STUDIES OF NOISE IN JOSEPHSON-EFFECT MIXERS AND THEIR POTENTIAL FOR SUBMILLIMETER HETERODYNE DETECTION

Thesis by

Robert J. Schoelkopf, III

in Partial Fulfillment of the Requirements

for the Degree of

Doctor of Philosophy

California Institute of Technology
Pasadena, California
1995
(Submitted November, 1994)

Acknowledgements

Of course, there are a multitude of people who deserve much of the credit (but none of the blame!) for the fact that this work could be completed. The only thing I can do is say thank you, and try to remember a few of them specifically.

First, I would like to thank my advisor, Tom Phillips, for his support and considerable patience. The freedom and resources from which I have benefitted during my years in the submillimeter group would be hard to find elsewhere, and in such quantities. Tom has always let me make my own decisions, and I am sure that the experience I have gained under him will stand me in good stead.

I owe equal thanks to Jonas Zmuidzinas, who has also performed advisorly duties above and beyond the call of duty. He was always willing to postpone other, more pressing, responsibilities to answer my questions, from the naive to the mundane and beyond. A huge proportion of the physics I have learned in the last few years has been through him, directly or indirectly. His dedication to research and tenacity in pursuit of a problem have also been a great influence.

The rest of the members of the submillimeter group, past and present, also deserve many thanks for their cooperation and collaboration in all matters. In particular, I would like to thank Thomas Büttgenbach, Chris Walker, and Jacob Kooi, who taught me much about receiver building. Pat Schaffer also gets many thanks for help with dewars, and always having a needed spare part tucked away somewhere. George Ugras has provided much entertainment (and friendship), both in and out of the lab. I thank Dave Woody for hospitality in Owens Valley, some very helpful discussions, and encouragement. In fact, there are countless other folks who contributed to making

Caltech such a stimulating and varied environment.

I would like to give special thanks to Todd Groesbeck, with whom I shared an office for nearly six years (!), without a single fistfight. Todd's easygoing manner and willingness to discuss all matters made many days at work brighter and easier to bear. He also helped in many computer-related matters, as unpaid code debugger, and protector from the vagaries of VMS. Finally, thanks to him for the beautiful TeX macros which are responsible for the form of this thesis.

A group of people without whom this work would have been impossible are the junction fabrication specialists at JPL. Rick LeDuc and Jeff Stern helped immeasurably by fabricating the junctions, and tolerated my presence in an already overcrowded lab. Jeff also took the time to produce the SEM picture used in Chapter 6. Thanks also go to the other members of this group for answering many a question, including Bruce Bumble, Andreas Judas, and Brian Hunt.

There are numerous people who have helped by way of encouraging me to pursue science, including all of the many teachers and mentors I have had along the way. Especially I would like to thank the guys at NASA/Goddard: Andy Szymkowiak, Rich Kelley, and Harvey Moseley, for letting me share a very enjoyable two years, and prompting my move to grad school.

Some assisted by way of keeping me sane and functioning throughout the years. In this category are all my squash partners, and in particular my climbing partner (and fellow running-dog), Fred Pool, who has been a great friend. Thanks also to John Ward, for getting me back into a small boat after far too many years. I would like to thank Jon Pedersen, with whom I learned many lessons which I use every day. I also owe a lot to the members of Bachelor's Anonymous (a.k.a the Molson-Milano Fund), namely Tim Breen, Tom Platt, Cole Wilson, Tory Meyer, Tom Winchell, and Dave Nafissian, for keeping up our friendship despite all the miles between us.

My family has also been very supportive from year one and onward. My mother, Jane, and my brother, Andy, have always been there when I needed them, and to share all the times, both good and bad. Most importantly, though, I would like to thank my wife and companion, Inger. Her patience with me has been limitless, her love unbounded, and her faith unwavering. Besides putting in tedious hours of proofreading, she made this thesis possible in countless other ways. Above all,

though, she has made it worth doing and brought joy to every step of the journey.

This work was funded by NASA grant NAGW-107, BMDO, and SDIO/IST. I would also like to acknowledge the support from a NASA Graduate Student Researcher Fellowship. Support in the form of time on the JPL/Caltech CRAY was also provided.

This thesis was typeset using plain TeX, with macros written by Todd Groesbeck. Nearly all of the plots appearing herein were prepared with MicroCal Origin, Version 3.0.

Dedication

This thesis is dedicated to the memory of my father, Robert J. Schoelkopf, Jr. He was truly one of the most intelligent and widely-read men I have ever encountered. When pressed hard enough, it turned out he almost always knew something about every subject, no matter how obscure, from literature, or history, or art. I think the curiosity and love of knowledge I inherited from him is largely responsible for where I have ended up. Though not a scientist, and certainly not mechanically inclined, he never discouraged my interest in gadgets and science. I know that this must have been difficult for him, but it did not go unrecognized or unappreciated. I hope, also, that I can come to emulate his understated manner and humility. My greatest regret about this thesis is that he was not able to see its completion. A half of a lifetime was not nearly enough to learn everything from him and his experiences. I will never forget him, or his love and support.

Abstract

This thesis describes both theoretical and experimental investigations into the dynamics and noise processes of Josephson junctions, with the intent of evaluating their potential as mixers in heterodyne instruments for submillimeter-wave (*i.e.*, the frequency range from 300 GHz to 3 THz) detection. Superconducting tunnel junctions utilizing the nonlinearity due to photon-assisted tunneling of quasiparticles (SIS mixers) have become the state-of-the-art technology for sensitive heterodyne detection up to frequencies of about 700 GHz. Recent progress in the fabrication of high-T_c superconductors has led to Josephson-effect devices with $I_C R_N$ products of up to ten millivolts, which might be suitable for mixing at frequencies of many terahertz. The key question for weighing the prospects for high-frequency Josephson mixers is that of the sensitivity which can be attained.

Previous experimental work on Josephson mixing suggests the existence of an "excess" noise, which degrades the sensitivity. Theoretical modeling of mixer performance, based on the resistively-shunted junction (RSJ) model for the dynamics of the device, also indicates the presence of larger noise than expected. The origin of this noise was not clearly understood, however, nor was its exact magnitude or expected scaling with frequency or junction characteristics known. In addition, previous experiments utilized crude devices of the point-contact type, which were unstable and thus undesirable for real applications.

In the first part of this thesis research, extensive numerical simulations were performed with the RSJ model, including calculations of mixer noise and conversion efficiency. These calculations have revealed that the source of excess noise is the AC Josephson oscillations of the device, which

can be completely incoherent, with a linewidth comparable to their frequency. Thus they appear as a broadband noise source. While this noise is intrinsic and unavoidable, an optimized mixer is still shown to be capable of interesting sensitivity levels, and the excess noise is expected to become relatively *less* important as the operating frequency is increased.

Secondly, a process has been developed for the fabrication of stable, well-characterized, and reproducible Josephson devices based on resistively-shunted Nb and NbN tunnel junctions. The devices utilize submicron-area, high current-density tunnel junctions and a AuGe shunt resistor to yield completely non-hysteretic I-V curves, normal-state resistances of about 40 Ω, and $I_C R_N$ products of about half a millivolt. These devices should be nearly optimal for mixing at 100 GHz.

Heterodyne measurements using these junctions have been performed in a waveguide mixer mount. Receiver temperatures as low as 190 K (DSB), with -6 dB conversion efficiency, have been obtained at 100 GHz, but these results are still a factor of about four higher than those predicted by the RSJ simulations. Accurate measurements of the available noise power of the junctions at the intermediate frequency of 1.5 GHz were made, and confirmed that the receivers were limited by elevated junction output noise. The deviations of the noise from theoretical predictions are shown to be caused by the nonlinear interaction of the junction with the embedding circuit. While this work points out some of the complexity introduced by the strong nonlinearity of Josephson devices, it is still expected that Josephson-effect mixers may be useful for heterodyne detection at very high frequencies.

Table of Contents

List of Figures

List of Tables

Chapter 1

Introduction and Background Material

Research is the process of going up alleys to see if they are blind.

– Marston Bates

This thesis describes investigations of heterodyne detection using the Josephson effect in superconducting tunnel junctions. Detectors based on the tunneling of unpaired electrons (quasiparticles) in superconducting tunnel junctions have been extremely successful in the millimeter and submillimeter wavebands, in some cases leading to systems with sensitivities approaching the fundamental limit imposed by quantum mechanics. In this first chapter, a basic introduction is given to needs of submillimeter astronomy and the methods of heterodyne detection. The basic physics of tunneling in superconductors and the application of tunnel junctions for detection is then described. Finally, we detail the motivations for the study of Josephson-effect mixers as detectors in the submillimeter-wave band.

1.1. Submillimeter Astronomy

The submillimeter-wave (1 mm to 100 μm or 300 GHz to 3 THz) region of the electromagnetic spectrum remains one of the newest and least explored areas of astronomy today. This frequency range is important for the understanding of several types of objects, from molecular clouds and star-formation regions to distant luminous galaxies (see, *e.g.*, Phillips and Keene, 1992). For example, the thermal emission

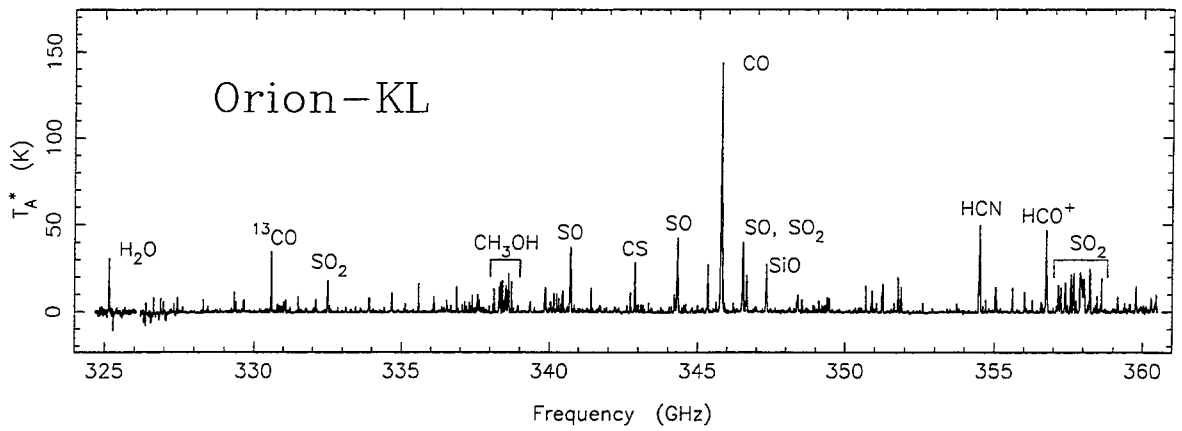

Figure 1.1 Submillimeter spectrum of the giant molecular cloud in Orion (M-42) in the range from 325 GHz to 360 GHz. The data consist of many observations performed at the Caltech Submillimeter Observatory with an SIS heterodyne receiver, each made with a roughly 500 MHz bandwidth at a resolution of 0.5 MHz (for an overall resolution of roughly 1 part in 10^6). Each of over 900 individual molecular transitions have been resolved and identified. (Courtesy T. Groesbeck; Groesbeck, 1994).

(at temperatures of 10 to 100 Kelvin) from the interstellar medium (ISM) peaks in the submillimeter range. In addition, many simple molecules have rotational transitions in this frequency range, allowing investigations of the chemistry of the ISM. For extragalactic sources at cosmological distances, the emission at optical and infrared wavelengths can be redshifted into the submillimeter band. However, there are many technological challenges which need to be solved to allow the full exploitation of the available astronomical information. There are difficulties due to poor atmospheric transmission, and there is a need for large area, high-accuracy telescopes, both to increase collecting area and to allow sufficient angular resolution. One of the main needs, however, is for high sensitivity and high spectral resolution detectors.

Since the submillimeter range lies between millimeter or radio wavelengths and the infrared, there are two approaches to detector development. First, one can extend infrared technologies such as bolometers or photodetectors downward into the submillimeter. The submillimeter-wave region remains inaccessible to most photodetectors, because the photon energies are too small compared to the bandgap of the available semiconductor materials. Bolometers can have high sensitivity, but have essentially no frequency resolution. This broad-band response is advantageous in observations of continuum emission processes, such as thermal radiation from dust. Frequency selection can in principle be accomplished with the use of appropriate optics

in front of the bolometers, but this can be somewhat awkward at longer wavelengths. A second approach is to push millimeter techniques, such as heterodyne receivers, upwards in frequency. In this thesis, we will concentrate on heterodyne techniques.

One of the most important uses of any astronomical detector is in spectroscopy, which often allows the determination of the physical parameters of the source such as temperature, pressure, and chemical composition. In addition, dynamical information can be extracted through the observation of Doppler-shifts in the emitting region. Heterodyne receivers can easily be used to produce extremely high spectral resolution (greater than a part in 10^6). This implies that velocities as small as a tenth of a kilometer per second can be discerned. Given the rich variety of molecular transitions (*cf.* Figure 1.1), high resolution is required simply to separate and identify the various molecules present in the ISM. In fact, these spectra can be used to study the unique chemistry which takes place in molecular clouds.

1.2. Heterodyne Detection

We need to describe the construction and figures of merit of a heterodyne system before we can discuss the technical requirements and optimization of such systems. All heterodyne systems operate by converting the signal to a lower frequency, where it can then be amplified and analyzed. The frequency conversion is performed by multiplying the signal with a strong coherent source, known as the local oscillator (or LO), in a nonlinear device called a mixer. The output can then be amplified and analyzed more conveniently, since the circuitry and amplifiers are easier to build at lower frequencies. In principle, there need not be any loss of frequency resolution, provided that the local oscillator is a spectrally pure (narrow linewidth) signal. In practice, the resolution will usually be limited by the spectrometer into which the mixer output is fed. This back-end spectrometry is not trivial, but it is typically easier to perform at the lower (downconverted) frequency.

The general layout of a heterodyne receiver is shown in Figure 1.2. For detection of weak signals, it may be desirable to have an amplifier which precedes the frequency conversion. For frequencies above 100 GHz, however, low-noise amplifiers are not available. For this reason, it is imperative to have high-efficiency frequency conversion in the mixer with a minimum of added noise. A common measure of

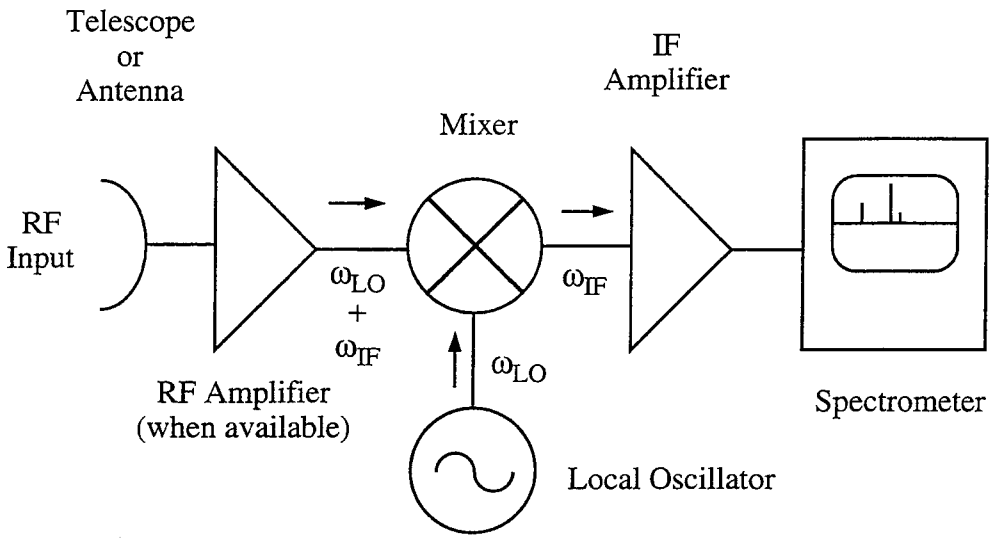

Figure 1.2 General layout of a heterodyne receiver system. The high-frequency signal is fed into the mixer (when high-frequency amplifiers are not available), where it combines with the local oscillator. The difference frequency is filtered and fed into an amplifier, and then the signal can be spectrally decomposed and analyzed.

an amplifier's noise used in microwave engineering is the noise temperature, T_N. This is defined as the temperature of a matched load, which, when placed at the amplifier's input, exactly doubles the output noise power. The signal-to-noise ratio of a heterodyne system is given by the Dicke radiometer equation,

$$(S/N) = \frac{T_{INPUT}}{T_N} \frac{1}{\sqrt{B\Delta t}}, \tag{1.1}$$

where T_{INPUT} is the equivalent temperature of the input signal, B is the detection bandwidth, and Δt is the integration time. Therefore, the noise temperature may be thought of as the power per unit bandwidth (*i.e.*, $P = k_B T B$) which can be detected with a signal-to-noise ratio of one, after a one second integration, and in a 1 Hz bandwidth. Since the integration time required to detect a weaker signal at a particular signal-to-noise ratio will decrease as the square of this noise temperature, the need for low noise temperatures is clear for astronomical or space-borne applications, where telescope time is limited.

We can discuss the performance of such a heterodyne system by making use of the well-known expressions for the gain and noise of a system of cascaded amplifiers (Kraus, 1966, p. 262). If the gain and noise of each stage of the system are given by G_i and T_i, respectively, then the system noise and gain

are

$$T_{SYS} = T_1 + \frac{T_2}{G_1} + \frac{T_3}{G_1 G_2} + \ldots$$
$$G_{SYS} = G_1 \times G_2 \times G_3 \times \ldots . \tag{1.2}$$

In a heterodyne system, we may treat the mixer as an amplifier whose input is at a high frequency (the radio frequency, or RF), and whose output is at some lower frequency (the intermediate frequency, or IF). The gain of the mixer is more often termed the "conversion efficiency." Typically this conversion efficiency is less than one, so that the following IF amplifier's noise can be important for the overall system performance. This IF amplifier usually has a large enough gain that the subsequent system components do not greatly affect the system noise temperature. We can see that the two most important figures-of-merit for a mixer are thus its noise temperature and conversion efficiency. In the submillimeter range, high power sources for use as the LO can be difficult to obtain, so it is advantageous if the mixer requires a smaller amount of LO power to pump it. Finally, any signal mismatch at the RF input of the mixer will also degrade the noise performance, so a mixer impedance which can be efficiently coupled to the source (through the antenna or telescope) is also desirable. An interesting limit, imposed by quantum mechanics, exists for the noise temperature of any linear, phase-preserving amplifier (Caves, 1982). Since this apparatus measures both the amplitude and phase of a mode of the electric field, and since these are conjugate variables, the uncertainty principle places a bound on the measurement accuracy. Expressed as a noise temperature, this "quantum-limit" is given by $T_Q = h\nu/k_B$. A mixer similarly preserves the phase information of the incoming wave, and this quantum-limited noise temperature is the best that any mixer can attain.

A few comments on the details of the frequency conversion process in mixers are warranted here. Consider some general nonlinear device, whose total current depends on the applied voltage, to which a time-varying voltage, $V(t)$ is applied. The voltage is composed of a constant term and two oscillatory components, *i.e.*,

$$V(t) = V_{DC} + A\sin(\omega_{LO}t) + B\sin(\omega_{Signal}t),$$

where V_{DC} is the constant bias voltage, and A and B are the amplitudes of the local oscillator and signal

waveforms, respectively. The current response of the device, $I(t)$, will be given by

$$
\begin{aligned}
I(t) \;=\; & I(V_{DC}) \;+\; C_1\,[A\sin(\omega_{LO}t) + B\sin(\omega_{SIG}t)] && \text{(original signal)} \\
& + \; C_2\left(\frac{A^2}{2} + \frac{B^2}{2}\right) && \text{(rectified signal)} \\
& - C_2\left(\frac{A^2}{2}\cos(2\omega_{LO}t) + \frac{B^2}{2}\cos(2\omega_{SIG}t)\right) && \text{(first harmonics)} \\
& + C_2\,A\,B\,\cos[(\omega_{LO} - \omega_{SIG})t] && \text{(difference frequency)} \\
& - C_2\,A\,B\,\cos[(\omega_{LO} + \omega_{SIG})t] + \ldots, && \text{(sum frequency)}
\end{aligned}
\tag{1.3}
$$

where C_1 and C_2 are the coefficients of a Taylor expansion of the device's current response about the operating point. Obviously, a linear device would not perform any frequency conversion. If the signal is at slightly less than the LO frequency, then the difference frequency (the IF) is the only slow (but not DC) term. This can then be filtered and led to the IF amplifier. However, if the signal frequency is slightly larger than the LO, the difference frequency is small and negative, which cannot be distinguished from the positive frequency. Unless special precautions are taken to reject this frequency in front of the mixer, we can see that the system will in general be sensitive to frequencies a certain offset on either side of the LO. Such a detector is known as a double sideband receiver, and so any IF bandwidth corresponds to two different RF bands. This affects, among other things, the way in which noise temperatures are quoted, since they are an effective noise power referred to the input of the receiver. One can either refer to a single-sideband temperature, which assumes coupling through only one sideband, or a double-sideband (DSB) noise temperature, where power is coupled through twice the bandwidth. The double-sideband noise temperature for a system is thus half the value as quoted in single-sideband units. All experimental sensitivities described in this thesis are double-sideband temperatures, while for the mixer simulations it is more convenient to calculate single-sideband numbers. These are then converted (divided by two) in making comparisons to experiment.

1.3. Superconducting Tunnel Junctions as High-frequency Mixers

As mentioned earlier, superconductors are well suited for mixing in the submillimeter-wave regime.

The key reason for their excellent performance is the sharpness and strength of the nonlinearities in superconducting tunnel diodes, which allows efficient and low-noise frequency conversion. Since superconductors can have very low loss in this frequency range (provided the photon energy is less than the energy required to break a Cooper pair; for Nb, this corresponds to 750 GHz), it is possible to construct efficient tuning circuits and antennas which are integrated with the devices. Finally, these superconducting junctions require local-oscillator power levels which are orders of magnitude lower than competing semiconductor devices (*e.g.*, Schottky diodes).

A superconducting tunnel junction consists of two superconducting banks separated by a very thin (several Å) insulator. Since the wavefunctions of the charge carriers on either side of the barrier extend into this barrier and overlap, carriers can tunnel across. At the onset of superconductivity in a metal, the electrons begin to feel an attractive potential and bind to form "Cooper pairs" (Cooper, 1956). Simultaneously, a gap in the density of states of the electrons appears (see, *e.g.*, Tinkham, 1975), with a singularity (large number of available states) on either side of it. At some finite temperature below the transition temperature, some of the electrons are paired; those remaining unpaired, due to thermal fluctuations, are known as "quasiparticles." There are thus two types of charge carriers in a superconductor: the Cooper pairs, which give rise to the resistance-less supercurrent, and the quasiparticles, which can give rise to dissipative currents. Tunneling of both of these charge carriers occurs in a junction, and both kinds of tunneling give rise to a nonlinearity which can be used for mixing.

A simplified current-voltage characteristic of a tunnel junction is shown in Figure 1.3. There is a supercurrent at zero voltage, of magnitude I_C, which arises from the tunneling of Cooper pairs. When this current is exceeded, the devices switches out to a voltage, known as the gap voltage, $V_{Gap} = 2\Delta/e$, where Δ is the energy gap in the density of states of the superconductor. There is a sharp increase in the tunneling current at this voltage, where the bias voltage equals this gap, and quasiparticles can tunnel. At large voltages, the current increases linearly with voltage, as it would in a junction with normal metals. This linear branch defines the "normal-state resistance," R_N.

Under illumination with a coherent source of radiation, the junction develops distinct "steps"

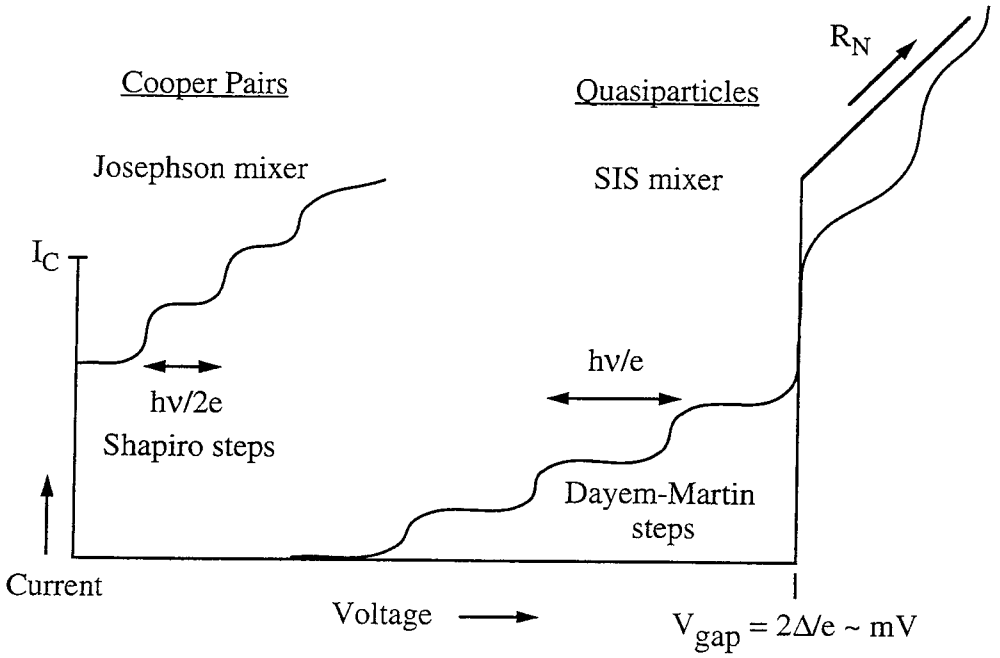

Figure 1.3 Current-voltage characteristic of a superconducting tunnel junction. Also shown are curves depicting a simplified version of the response to a source of coherent radiation. The Shapiro steps, due to photon-assisted tunneling of Cooper pairs, move out from zero voltage and have a width of $\Delta V = h\nu/2e$. The Dayem-Martin steps are caused by photon-assisted tunneling of quasiparticles, are displaced from the gap voltage, and have a width of $\Delta V = h\nu/e$.

in this current-voltage characteristic, which are caused by photon-assisted tunneling. The steps which are due to the assisted tunneling of Cooper pairs are known as "Shapiro steps," (Shapiro, 1963) and move out from zero voltage with a spacing of $\Delta V = h\nu/2e$, where ν is the frequency of the radiation, and $2e$ is the charge of the Cooper pair. The second set of steps are known as "Dayem-Martin," or quasiparticle steps (Dayem and Martin, 1962), and are displaced on either side of the gap voltage with a spacing of $\Delta V = h\nu/e$. Mixers based on the Dayem-Martin nonlinearity are known as "SIS mixers," while those utilizing the Cooper pair tunneling are known as "Josephson-effect mixers." The quasiparticle nonlinearity is strong only in tunnel junctions, while the Josephson effect is observable in a wide range of superconducting devices, such as microbridges, point contacts, and superconductor-normal-superconductor junctions.

A theoretical framework for the analysis of the response of a tunnel junction to radiation was developed by Werthamer (1966) and applied to the particular problem of SIS mixers by Tucker

(1979). Werthamer used a tunneling Hamiltonian approach (Cohen, Fallicov, and Phillips, 1962), in which the tunneling operator simply serves to destroy a particle on one side of the junction and create a particle on the other side. He then calculated the junction's response function (*i.e.*, the expectation value of the operator) based upon the BCS (Bardeen, Cooper and Schrieffer, 1957) wavefunctions for the superconductors. A full treatment of the microscopic theory is beyond the scope of this discussion, but a few relevant results will be mentioned. There are two complex response functions, one due to pair tunneling, the other due to quasiparticle tunneling. The pair-current terms display a dependence on the difference in the superconducting phase on either side of the junction, and represent the Josephson effect. The other terms are the result of quasiparticle tunneling, and are phase independent. Werthamer derived analytic expressions for these response functions at zero temperature.

The microscopic treatment of tunneling has been used (*cf.* Tucker, 1979, and the excellent review by Tucker and Feldman, 1985) to analyze the performance of mixers using the quasiparticle nonlinearity. Since the nonlinearity is sharp compared to the photon energy, several behaviors are exhibited which are not possible with classical mixers. The first is the possibility of conversion gain, *i.e.*, frequency down-conversion with amplification. Classical mixers are limited to efficiencies of −3 dB (Torrey and Whitmer, 1948). The second interesting prediction is that mixer noise temperatures approaching the quantum limit, $T_Q = h\nu/k_B$, can be attained. A convenient feature of the microscopic theory for quasiparticle tunneling is that for a constant voltage bias, the zero frequency I-V curve is purely due to the imaginary part of the quasiparticle response function. The analyticity of the response function can then be used to infer the complete quasiparticle response via a Kramers-Kronig transform. This allows a direct comparison of Tucker's theory with experiment, without the need to know the complete details of any nonideal behavior in the junction. It is interesting to note, however, that Tucker's theory of SIS mixing is somewhat arbitrary in that the effects of pair currents have been ignored. In practice, these pair currents (the Josephson effect) can lead to noise and undesirable effects in SIS mixers, and it is common practice to suppress the Josephson effect with a magnetic field, in which case reasonable agreement with theory is seen (*e.g.*,

de Lange, 1994). A treatment of Josephson mixing based on the microscopic theory has not been performed; here the dynamics of the phase dominate, while the pair current response function is essentially frequency-independent up to the gap frequency of the superconductor.

The predictions of Tucker's quantum theory for SIS mixers have in fact been borne out. SIS mixers are currently the state-of-the-art technology for sensitive heterodyne detection at millimeter and submillimeter wavelengths. Experiments have shown that the mixer noise can indeed closely approach the quantum limit (Mears *et al.*, 1991), and that large gain is possible (McGrath *et al.*, 1981). In fact, when integrated with ultra-low noise IF amplifiers using a HEMT (high-electron mobility transistor), receiver system temperatures within a factor of five of the quantum limit have been obtained up to nearly 700 GHz. Although SIS junctions have a large parasitic capacitance, which arises from the plane-parallel geometry of the two conductors, the detrimental effects of this reactance can be minimized through the use of proper tuning circuits. Early work with these mixers used mechanical tuners and waveguide coupling structures (*e.g.*, Dolan *et al.*, 1981; Woody *et al.*, 1985). More recently, integrated tuning circuits which are fabricated on the mixer chip have been used to good advantage. Mixers with tuning can use either waveguide (*e.g.*, Kerr and Pan, 1990; Kooi *et al.*, 1994) or quasi-optical coupling schemes, in which an integrated planar antenna and a dielectric lens feed the junction (Büttgenbach *et al.*, 1992; Zmuidzinas *et al.*, 1994). Noise from the Josephson effect (which is probably chaotic in these high-capacitance junctions) has been minimized via the application of magnetic fields. Finally, the advent of high quality, high current-density (and durable) Nb tunnel junctions suitable for these SIS mixers has led to their widespread application in submillimeter astronomy.

Nonetheless, the upper frequency limit for the operation of SIS mixers remains uncertain. The fundamental limit is set by the energy scale of nonlinearity, *i.e.*, the energy gap of the superconductor. Higher transition temperature superconductors have larger energy gaps, and should therefore operate to higher frequencies. The junctions themselves are expected to function well up to frequencies where the photon energy is twice the energy gap ($h\nu = 4\Delta$, which corresponds to ~ 1.4 THz for Nb) of the superconductor (Wengler, 1987). However, tuning structures will have to be fabricated with normal

metals, because the loss of the superconductors increases dramatically at $h\nu = 2\Delta$. High current-density junctions have been made using NbN ($T_C \sim 17K$ and $2\Delta/e \sim 5$mV), but the few receiver tests with these junctions have shown poorer sensitivity than expected (Stern, 1991; McGrath *et al.*, 1991). Because of the success of SIS mixers, however, current interest in other mixer technologies, such as hot-electron bolometers and Josephson mixers, focuses on the higher (> 700 GHz) frequencies.

1.4. Motivation for Study of Josephson Mixers

Just as the upper frequency limit of SIS mixers is determined by the voltage scale of the nonlinearity (the gap voltage), Josephson-effect mixers are limited by the size of their characteristic voltage, which is the $I_C R_N$ product. Tunnel junctions suitable for SIS mixers require very good materials growth and control in order to produce the sharp nonlinearity required, and for this reason it is difficult to find new materials systems which are acceptable. In contrast, a wide variety of superconducting devices can display strong Josephson effects, including grain boundary junctions, point contacts, SNS weak links, and microbridges. For example, devices based on high-T_C materials (YBCO) have already produced Josephson characteristics with characteristic voltages of up to 10 mV (Rosenthal *et al.*, 1993). However, due to the extremely short coherence lengths (a few Å) in these superconductors, tunnel junctions suitable for SIS mixing may never be possible, since they would require perfect epitaxial growth to within one unit cell on either side of the barrier. SIS mixing with tunnel junctions also requires a well-defined gap in the density of states of the superconductor, while it is still not clear whether high-T_C materials are BCS superconductors. These materials may have a more complicated density of states or states within the gap, which would affect the I-V curve and SIS mixing. We will see later in this thesis that optimal Josephson mixing can be carried out up to frequencies of order the characteristic frequency, $\omega_C = \frac{2e}{\hbar} I_C R_N$, which corresponds to 484 GHz per mV of $I_C R_N$ product. For a high-T_C Josephson device, one might obtain good Josephson mixing to frequencies of 5-10 THz, far in excess of any currently envisaged SIS mixer. This possible application to the new ceramic superconductors is the main motivation for the continued study of Josephson mixing.

Unfortunately, there are several issues which remain to be solved before mixing in these devices can be undertaken. Current fabrication technology for high-T_c devices uses extremely high dielectric constant substrates, which may also have large far-IR losses. Device impedances (*i.e.*, normal-state resistances) are commonly very small ($\lesssim 1\Omega$). Most measurements on these devices have therefore suffered from extremely large RF mismatches. Progress is being made on improving the device properties, both in raising the impedances, and in adapting the fabrication to other substrates with better electrical properties (Hunt *et al.*, 1994).

At the same time, however, previous work on Josephson mixing has left unanswered questions about the limits of their performance. Most experiments utilized point contact devices, which were unstable and not reproducible, and whose circuit parameters were unknown. The procedures for mixer optimization with respect to device parameters and design of the RF embedding circuit were not clearly established. Most importantly, both experimental and theoretical investigations suggested the presence of an "excess" noise, whose origin and exact magnitude were unclear. So while the application of Josephson-effect mixers based on high-T_c devices remains an attractive option for submillimeter and far-IR heterodyne detection, many issues related to the basic behavior of these devices remain to be addressed.

Another intriguing aspect of Josephson-effect mixing is the possibility of using the internal oscillations of the junction to serve as a "built-in" local oscillator. Oscillators based on arrays of Josephson junctions have been studied as high-frequency sources, because the AC Josephson effect (*cf.* Section 2.4C) makes them natural voltage-controlled oscillators. Mixing in a junction without an external LO has been proposed (*e.g.*, Likharev, 1986, p. 422) and a simple theoretical analysis has been performed (Devyatov *et al.*, 1986), but this mixing mode has never been experimentally realized. One problem is the large natural linewidth of these oscillations, but if these could be reduced in some way (such as low-frequency shunting or bias on low-impedance resonances) then the requirement for high-frequency sources could be eliminated, leading to a significant reduction of the cost and complexity of a heterodyne system.

1.5. Overview of Thesis

In light of the preceding discussion, the approach for the research described in this thesis was as follows. Since there remain significant fabrication-related issues associated with high-T_C devices and questions about their high-frequency materials characteristics, as well as those of the substrate materials, we decided to undertake careful measurements of optimized Josephson mixers based on low-T_C superconductors. In addition, it was important to understand and quantify the excess noise of Josephson mixers in general, in order to have any basis for evaluating the potential for sensitive high-frequency detectors. To this end, extensive simulations of mixer performance, based upon the well-known resistively-shunted junction (RSJ) model, were undertaken. These simulations did indeed lead to a much clearer picture of the excess noise mechanism, and the realization that although it was intrinsic to all Josephson mixers, its presence might not prohibit the achievement of interesting sensitivity levels. After the noise was clarified and the conditions for receiver optimization in its presence were known, then a well-characterized low-T_C device could be tested to see if the theoretical understanding of this noise could be verified. It was seen that suitable devices utilizing high current-density, low-T_C tunnel junctions could be realized, although they required the use of advanced lithographic techniques. A process for the fabrication of these devices was developed, and they were then tested in a well-known receiver configuration using a waveguide mixer-mount, which allowed wide variation of the RF conditions presented to the device. Accurate measurements of the receiver sensitivity and the output noise of the devices, both with and without LO illumination, were undertaken. We had hoped to eventually obtain high-T_C based devices which could be tested in the same configuration, in order to facilitate a comparison between different materials technologies, but these devices did not become available.

The organization of the thesis, then, generally follows this line of inquiry. In Chapter 2, the RSJ model is presented, and some of its basic behaviors are reviewed. In Chapter 3, we move on to the inclusion of fluctuations into the RSJ model formalism, discuss the presence of excess noise and its origin in this case without a oscillatory drive, and make comparisons between the results of

simulations and the simple model of Likharev and Semenov for this noise. Chapter 4 discusses the RSJ model with the presence of a local oscillator and the mixing process in Josephson junctions. The method used for calculation of mixer performance is described, and results of these mixer simulations are shown for an optimized case, and as a function of several key parameters. In Chapter 5, the mechanism behind the excess noise is described and the optimization of a mixer, given the existence of this noise, is discussed. The requirements for creating devices suitable for Josephson-effect mixing based on resistively-shunted tunnel junctions, the resistor design and implementation, and the methods used for device fabrication are presented in Chapter 6. Experimental data obtained using these shunted junctions is collected in Chapters 7 and 8. First, we describe the calibrated microwave system and the measurements of the output noise of these devices at the typical intermediate frequency of 1.5 GHz. Finally, the results of several series of 100 GHz receiver measurements, the characterization of these receivers, and the comparison of the receiver results with the earlier theoretical predictions are discussed. Chapter 9 presents a brief review of the material presented, and discusses the conclusions which can be drawn from the work.

Chapter 2

The RSJ Model

Get your facts first, and then you can distort them as much as you please.

– Mark Twain

In this chapter, we will lay the foundations for the discussion of noise and mixing in Josephson junctions, which will rely on an understanding of the dynamics of the nonlinear device acquired through the resistively-shunted junction (RSJ) model. First, the RSJ model and the AC and DC Josephson equations on which it is based will be derived. The basic phenomena associated with this model, and with all Josephson-effect devices will be outlined, and the various junction parameters and their effect on the junction dynamics will be discussed. Finally, the approach to the solution of the general RSJ model will be presented. The response of Josephson devices to a periodic driving force (*i.e.*, the local oscillator required for mixing), and the procedure for obtaining mixer parameters from the RSJ model will be described in the following chapter.

2.1. The Josephson Equations

The Josephson effect, which occurs between any two weakly-coupled superconductors, was predicted theoretically in the doctoral dissertation of B.D. Josephson (Josephson, 1962 and 1963), and experimentally confirmed shortly thereafter (Anderson and Rowell, 1963). There are two basic

results: the first is that the current flow between the two coupled superconductors is proportional to the sine of the phase difference between the superconducting wavefunctions, which is known as the DC Josephson effect, and the second is that the phase difference is proportional to the integral of the voltage between the superconductors, which gives rise to the AC Josephson effect. These two results were initially derived by Josephson using a tunneling Hamiltonian approach similar to the method of Werthamer (*cf.* Section 1.3). A simpler derivation of these results is presented below which follows the treatment of the famous Feynman lectures (Feynman, Leighton, and Sands, 1964) on physics.

Consider two identical superconductors which are weakly coupled to each other. This coupling can take the form of an insulating barrier which is thin enough to permit quantum mechanical tunneling of the electrons and Cooper pairs, a narrow constriction smaller than a superconducting coherence length (*i.e.*, a microbridge), or numerous other realizations. The equations of motion for the two wavefunctions in the two superconductors are then

$$\begin{aligned} \jmath\hbar\frac{\partial\psi_L}{\partial t} &= U_L\psi_L + K\psi_R \\ \jmath\hbar\frac{\partial\psi_R}{\partial t} &= U_R\psi_R + K\psi_L, \end{aligned} \tag{2.1}$$

where K is the coupling energy between the right (R) and left (L) superconductors. If we connect the superconductors to a battery and apply a voltage, V, we introduce a chemical potential and an energy shift of qV where q is the charge of the carriers ($q = 2e$ for Cooper pairs). We substitute the Ginzburg-Landau (Tinkham, 1975) form for the macroscopic wavefunction of the superconductors, $\psi = \sqrt{\rho}e^{\jmath\theta}$, where ρ is the number density of the pairs and θ is the superconducting phase. We then obtain the following equations, after separating the real and imaginary parts,

$$\begin{aligned} \frac{\partial\rho_L}{\partial t} &= \frac{2K}{\hbar}\sqrt{\rho_L\rho_R}\sin\phi \\ \frac{\partial\rho_R}{\partial t} &= -\frac{2K}{\hbar}\sqrt{\rho_L\rho_R}\sin\phi \end{aligned} \tag{2.2}$$

and

$$\frac{\partial \theta_L}{\partial t} = \frac{K}{\hbar}\sqrt{\frac{\rho_L}{\rho_R}}\cos\phi + \frac{eV}{\hbar}$$
$$\frac{\partial \theta_R}{\partial t} = \frac{K}{\hbar}\sqrt{\frac{\rho_L}{\rho_R}}\cos\phi - \frac{eV}{\hbar}. \tag{2.3}$$

Here we have defined $\phi = \theta_L - \theta_R$. The first two equations (2.2) represent charge conservation, so that the current leaving one electrode equals the current entering the other electrode. The current density of the pairs is thus $J = J_C \sin\phi$, where J_C is some critical current density which is proportional to the coupling strength, K, between the electrodes. Integrating over the electrode area gives

$$I = I_C \sin\phi. \tag{2.4}$$

This sinusoidal dependence of the current on the phase difference is sometimes known as the DC Josephson effect. Taking the difference between the equations (2.3), we obtain the differential equation for the phase difference, ϕ,

$$\frac{\partial \phi}{\partial t} = \frac{2e}{\hbar}V, \tag{2.5}$$

which is known as the AC Josephson equation. Notice that the specific mechanism leading to the coupling does not affect the resulting equations or the sinusoidal current-phase relationship. If the coupling is sufficiently strong, however, then the wavefunctions will be altered, the coupling could become nonlinear, and more complicated dependences can result. The basic Josephson relations have been observed in a wide variety of materials systems and device types, including tunnel junctions, SNS junctions, weak links, and microbridges (see *e.g.*, Likharev, 1986). In the next section we will see how these two equations are used to derive the RSJ equation for a generalized, idealized Josephson junction with parasitic resistive and capacitive elements.

2.2. The RSJ Equation

The RSJ model was introduced independently by McCumber (1968), Johnson (1968), and Stewart (1968), and has been studied extensively since then. Because of the difficulty of solving the RSJ equation in the general case, many studies have focused on analog (*e.g.*, Claassen and Richards, 1978) and digital (*e.g.*, Kautz, 1981) simulations of the model. The RSJ model has been applied

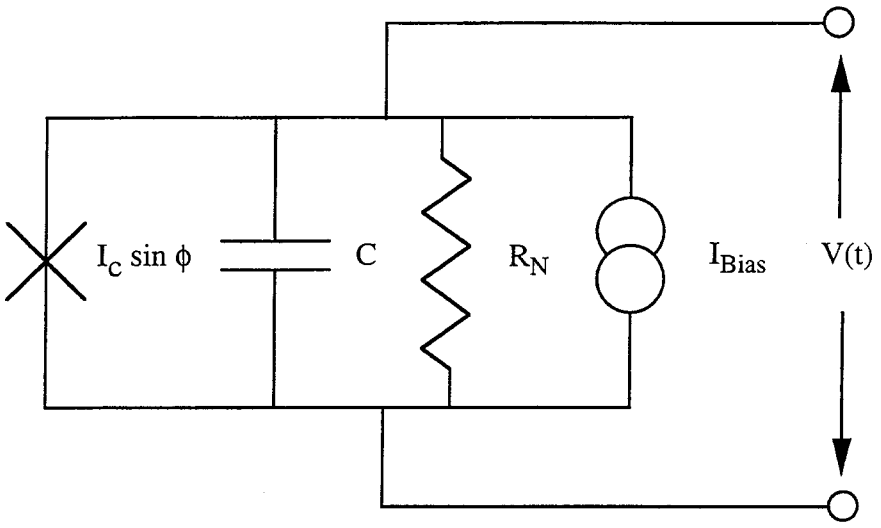

Figure 2.1 Equivalent circuit basis for the RSJ model. Circuit consists of a parallel combination of a linear resistance, a capacitance, and an ideal Josephson element with a sinusoidal current phase relation. An external current source drives the circuit.

widely to account for the behavior of many different types of devices, including tunnel junctions, point contacts, weak links, microbridges and SNS junctions. Many of these practical realizations of Josephson junctions can have aspects, such as additional nonlinearities due to quasiparticle tunneling or heating, which are not captured by the model. However, all of the observed behavior which is due to the Josephson effect can be reproduced by the RSJ model, at least qualitatively. In addition, devices are often fabricated with external shunt resistances, and these devices can be described extremely well by the RSJ model. In most studies of sensors and other devices which utilize the Josephson effect, the RSJ model is productively used to predict and interpret device performance.

The simple equivalent circuit of the junction which leads to the RSJ equation is shown in Figure 2.1. The circuit consists of the parallel combination of an ideal Josephson element, which is a current source which varies with the sine of the phase, a resistor, and an optional capacitor. All of these elements represent conduction processes which occur simultaneously within the Josephson junction. Most commonly, the capacitance is ignored, and the resistor is assumed

to be a simple linear conductance, and the only dissipational element in the circuit. Physically, the Josephson element represents conduction due to Cooper pair tunneling, and the capacitance arises from inevitable parasitic coupling between the two electrodes of the device, although it can be small in some geometries. The resistive element can arise from quasiparticle (*i.e.*, unpaired electrons in the superconductor) tunneling, or from some other explicit conduction path such as a shunt resistor. In some sense, all loss in the absence of such an external element must be related to the normal electrons, since the Cooper pairs are dissipationless. The term "RCSJ model" can sometimes be found in reference to the case of non-zero capacitance. Variations of the basic model in which the resistor can be a nonlinear, voltage-dependent conductance are referred to as the "RSJN model" (Likharev, 1986). In this work, we did not investigate the effects of nonlinear resistors. Throughout this thesis, we will use the term "RSJ model" to refer to the model both with and without capacitance.

The circuit diagram allows us to write the equation of motion for the single dynamical variable of the model, which is the phase difference across the junction, simply by summing the current through the device and making use of the Josephson equations. The total current is

$$I_{Total} = C\frac{\mathrm{d}V}{\mathrm{d}t} + \frac{V}{R} + I_C \sin\phi,$$

where the first term is simply the displacement current through the capacitor. We can eliminate the voltage by making use of the AC Josephson equation

$$\frac{\mathrm{d}\phi}{\mathrm{d}t} = \frac{2e}{\hbar}V,$$

which gives us the RSJ equation,

$$C\frac{\mathrm{d}^2\phi}{\mathrm{d}t^2} + \frac{1}{R}\frac{\mathrm{d}\phi}{\mathrm{d}t} + I_C \sin\phi = I_T. \tag{2.6}$$

Here the right-hand side, I_T, is the total current supplied to the circuit from an external current source, which can include a DC bias, a periodic forcing term (*i.e.*, a local oscillator), and other contributions. Because of the extreme nonlinearity introduced by the sinusoidal term, this very

simple equation exhibits a variety of complex behavior under different driving currents and circuit parameters. Later in this chapter we will discuss the inclusion and influence of fluctuations on this model.

2.3. The RSJ Model in Normalized Units

In order to simplify the solution and understanding of the RSJ model, it is customary to recast the equation in a set of normalized, dimensionless units. While this forces the inconvenience of converting back and forth while interpreting experimental data, it also gives a small number of dimensionless parameters, each of which determines the strength of a different physical processes in the device. In this thesis, we will exclusively utilize the so-called "McCumber parameterization" (McCumber, 1968), but a slightly different "Johnson parameterization" (Johnson, 1968) can occasionally be found in the literature.

First, the critical current, I_C, the normal-state resistance, R_N, and their product, $I_C R_N$, provide natural scales for normalization of current, impedance, and voltage, respectively. Second, we can remove the multiplicative constants in the AC Josephson equation, (2.5), by introducing the normalized time,

$$\tau = \frac{2e}{\hbar} I_C R_N t = \omega_c t,$$

where ω_c is the critical frequency of the device, and is the Josephson frequency which corresponds to the $I_C R_N$ voltage. The complete normalization is therefore

$$\begin{aligned} i &= \frac{I}{I_C} & v &= \frac{V}{I_C R_N} \\ \tau &= \omega_c t & \Omega &= \frac{\omega}{\omega_c}. \end{aligned} \tag{2.7}$$

The AC Josephson equation then becomes simply

$$\dot{\phi} = v, \tag{2.8}$$

where the dot represents differentiation with respect to normalized time, and the RSJ equation is

TABLE 2.1

RSJ MODEL NORMALIZED UNITS AND PARAMETERS

UNIT NORMALIZATIONS

Quantity	Dimensioned Symbol	Normalized Symbol	Scaling [a]
Current	I	i [b]	I_C
Voltage	V	v	$I_C R_N$
Frequency	ω	Ω	ω_C
Time	t	τ	ω_C^{-1}
Impedance	Z	z	R_N

PARAMETERS

Quantity	Dimensioned Symbol	Parameter	Definition
Critical Frequency	ω_C	–	$\frac{2e}{\hbar} I_C R_N$
Capacitance	C	β_C	$\frac{2e}{\hbar} I_C R_N^2 C$
Temperature	T	Γ	$\frac{2e}{\hbar} k_B T / I_C$

[a] One multiplies normalized units by this scaling factor to obtain the equivalent dimensioned units.

[b] Throughout this thesis, we use i for the normalized current and j for $\sqrt{-1}$.

then

$$\beta_C \ddot{\phi} + \dot{\phi} + \sin\phi = i_T. \tag{2.9}$$

Here we have introduced the McCumber beta parameter, defined as

$$\beta_C = \frac{2e}{\hbar} I_C R_N^2 C. \tag{2.10}$$

This dimensionless parameter controls the importance of the capacitance on the junction dynamics, and is simply the product ω_C times R_NC, or the ωRC product at the critical frequency. For β_C values greater than about one, the current-voltage characteristic of the device becomes double-valued, or hysteretic (see Section 2.4.A). Notice that the characteristic frequency of the junction, $\omega_C = \frac{2e}{\hbar} I_C R_N$, increases linearly with the $I_C R_N$ product of the device. Increasing the $I_C R_N$ product will therefore increase the maximum operating frequency for the device. For all further discussions of RSJ modeling in this thesis, we will use the normalization scheme and the notational conventions detailed in the following table, 2.1.

The RSJ differential equation unfortunately cannot be solved in closed form for the general case of nonzero capacitance. The behavior of the system has been analyzed by numerical solution

of the equation of motion, both in regard to Josephson junctions, and to several other systems which are analogous. The equation of motion is identical to that of the damped, driven pendulum, where ϕ is the angular deviation from vertical. The resistor then corresponds to a viscous damping force, and the capacitance corresponds to the moment of inertia of the pendulum bob. The RSJ model is known to have very complex behavior under a periodic drive, including period-doubling bifurcations and deterministic chaos. This chaotic behavior is only possible for nonzero capacitance (*e.g.*, Kautz and Monaco, 1984; Octavio, 1984). In the next section, we will explore some of the basic phenomena associated with the RSJ model in the absence of oscillatory drive (sometimes known as the autonomous RSJ model), in order to develop a familiarity with the basic dynamics which take place.

2.4. Basic Results of the RSJ Model

As mentioned previously, general solutions of the RSJ equation are not available. However, for the simplest case with no capacitance and no fluctuations, a closed form solution can be obtained. An excellent reference for the following discussions and any other questions pertaining to Josephson-effect devices is the monograph by Likharev (1986).

An analog to the RSJ model which can be very useful in lending intuition to the expected behavior is the washboard model. In this picture, a massive particle moves in a potential, shown in Figure 2.2. The position of the particle is the phase of the junction, and the velocity is the voltage. The beta parameter corresponds to the mass of the particle. The form of the potential is given by $U(\phi) = 1 - i\phi - \cos\phi$, so that an increase in the bias current causes an increase in the overall linear slope of the potential. We will use this analogy in describing some of the phenomena below.

A. Current-Voltage Characteristics

The I-V curve of the junction reveals the effects of the various parameters (I_C,R_N,β_C,Γ) of the RSJ model. The I-V curve for an RSJ junction with zero capacitance is shown in Figure 2.3. For a constant current bias with a current less than the critical current, $i < 1$ (or $I < I_C$ in dimensioned units), examination of (2.9) shows that there is a solution with constant phase $\phi = \arcsin i$, and

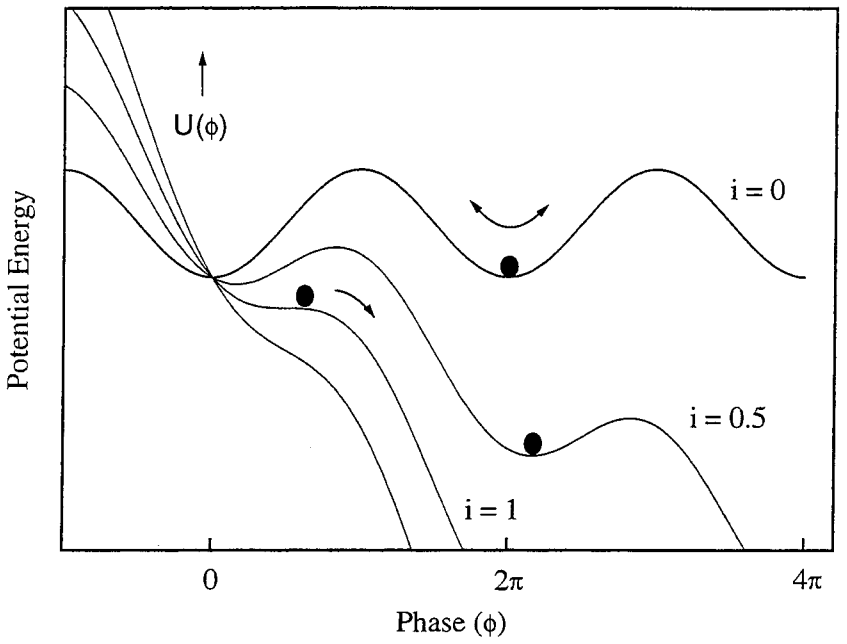

Figure 2.2 Depiction of the washboard analog to the RSJ model. A massive particle rolls through a viscous medium on a potential whose form is $U(\phi) = 1 - \cos(\phi) - i\phi$. The velocity of the particle corresponds to the voltage across the device.

therefore zero voltage. This is the DC supercurrent, where the current rises at zero voltage to a maximum value equal to the critical current. For bias currents greater than the critical current, $i > 1$, the method of Stewart (1968) yields $v = \sqrt{i^2 - 1}$. At large biases, $i \gg 1$, the I-V curve becomes linear again, with a slope of one (or R_N in dimensioned units). The I-V curves for the RSJ model are always symmetric about the origin. In terms of the washboard analogy, for $i < 1$, the particle is trapped in a minimum of the potential, and therefore the average phase is constant, and the voltage is zero. At $i = 1$, the minima in the potential become unstable, resulting in the sudden onset of voltage with increasing current. Finally, for $i >> 1$, the sinusoidal variations in the potential are small compared to the overall slope, and the phase increases nearly linearly with time, at a rate set by the damping. This causes the linear I-V curve at large voltages.

The addition of a nonzero capacitance can affect the shape and character of the I-V curve. According to the washboard picture, increasing the capacitance of the device is analogous to increasing the mass of the particle in the potential. At large bias, the device is in the running state,

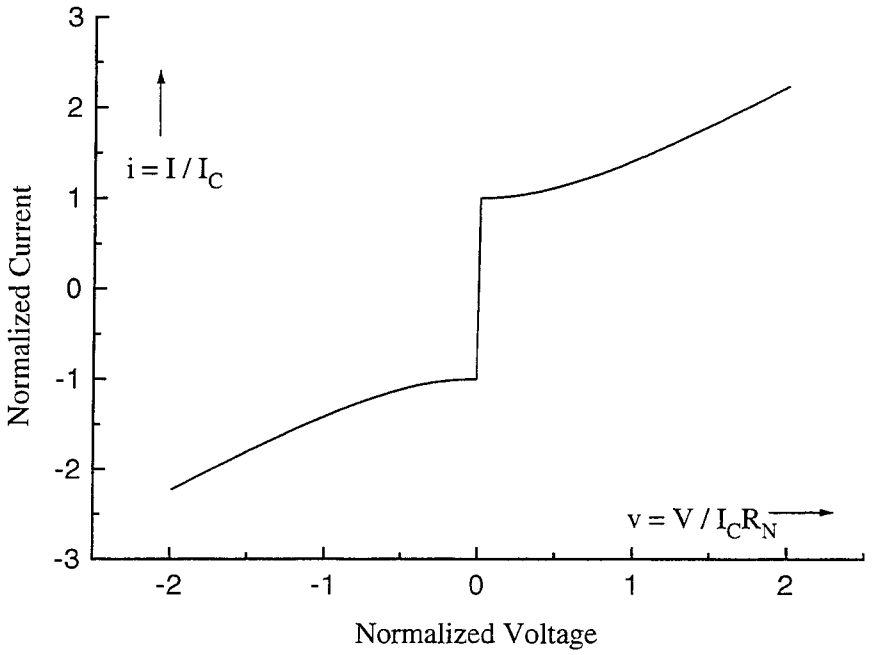

Figure 2.3 Current (vertical axis) as a function of voltage (horizontal axis) in normalized units for RSJ model with no capacitance and zero fluctuations.

the voltage is nonzero, and the particle is not trapped. For a device with capacitance, the inertia of the particle allows it to continue to travel down the potential as the bias current is reduced, even after the wells in the potential become marginally stable. This means that the junction will remain in the nonzero-voltage state at currents below the critical current, and the I-V curve has become hysteretic. As the bias current is increased past the critical current, the junction abruptly switches out into the nonzero-voltage state. Current-voltage curves, obtained through numerical integration of the RSJ equation for different values of the dimensionless capacitance parameter, β_C, are shown in Figure 2.4. I-V curves become hysteretic in the absence of fluctuations for β_C values of greater than 0.8 (Likharev, 1986, p. 98), and the amount of hysteresis increases as β_C is increased past this value. In addition, the I-V characteristic has sharper curvature in the region $V \lesssim I_C R_N$ with the addition of capacitance, even for nonhysteretic devices.

B. Josephson Oscillations

Perhaps the most important feature of a Josephson device when biased at nonzero voltage

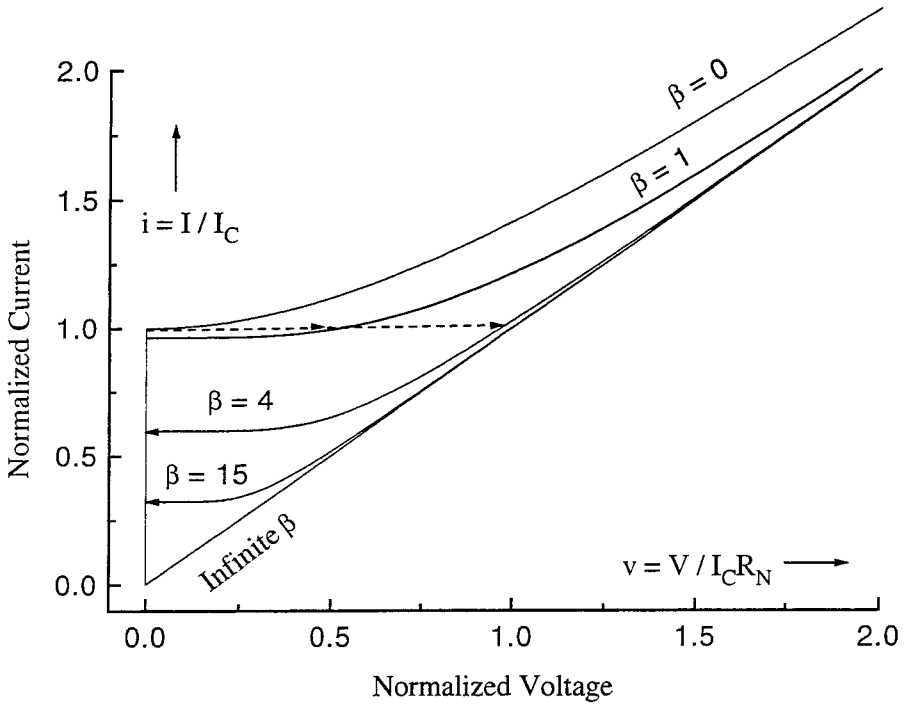

Figure 2.4 The effect of capacitance on RSJ I-V curves. Curves for several different values of the McCumber beta parameter are shown (β = 0,1,4,and 15). For hysteretic curves, the right-most curves are only accessible when the bias is swept in downward direction, as indicated by the arrows, and switching occurs as indicated by the dashed lines. Note that because of the symmetry of the curves about the origin, only the positive branch is displayed here.

is the spontaneous generation of coherent radiation due to the AC Josephson effect. This effect has been used to produce high-frequency sources of radiation (*e.g.*, Lukens, 1990), although the low power levels available from a single junction and the large intrinsic linewidth usually requires the use of coherent arrays of devices. As we will see in following chapters, the oscillatory response of the device when biased is exceedingly important in determining the output noise and heterodyne sensitivity of Josephson junctions.

Consider a device which follows the Josephson equations (2.4) and (2.5) under a constant voltage bias, V_0. Integration of (2.5) gives a linear ramp in the phase plus some constant of integration, $\phi(t) = \phi_0 + \frac{2e}{\hbar}V_0 t$. The current as a function of time will then be $I(t) = I_C \sin(\frac{2e}{\hbar}V_0 t) = \sin(\omega_J t)$, where ω_J is known as the Josephson frequency. Thus the junction behaves as a voltage-controlled oscillator (VCO) with an oscillation frequency directly proportional to the bias voltage.

The constant of proportionality, $2e/h$, corresponds to 483.5 GHz per millivolt of bias voltage.

Notice that the oscillating current implied above will lead to a varying voltage, breaking our assumption of perfect voltage bias. The effect of the oscillatory voltage will be to introduce harmonics of the basic Josephson frequency, or equivalently, to cause the oscillation to become nonsinusoidal. The self-consistent solution for the phase in the case of vanishing capacitance ($\beta_C = 0$), as obtained by Aslamazov, Larkin, and Ovchinnikov (1968), is

$$\phi(t) = 2\arctan\left(\frac{v}{i+1}\tan\frac{\Theta(t)}{2}\right) - \frac{\pi}{2}, \tag{2.11}$$

where $\Theta(t)$ is the integral of the DC voltage, $\Theta(t) = \frac{2e}{\hbar}\widehat{V}t$. The corresponding voltage waveform is given by

$$V(t) = \widehat{V} + \Im m\left\{\sum_{k>0} V_k e^{j\,k\omega_J t}\right\}$$

where $\widehat{V}$ is the average voltage (in dimensioned units), and the harmonic amplitudes, v_k, are given by

$$v_k = \frac{V_k}{I_C R_N} = \frac{2v}{(i+v)^{|k|}}. \tag{2.12}$$

The harmonic content of the oscillation increases as the average voltage decreases. In the washboard analogy, once the device is biased above the critical current, the particle will roll down the potential with some average velocity or voltage. As the particle experiences the undulations in the potential, however, its velocity will vary periodically. At low bias, the particle rolls slowly along the nearly horizontal regions of the potential, and then produces a sharp voltage spike as advances to the next well. At large average voltage, the undulations in the potential are less important, and the oscillations become nearly sinusoidal. Two example oscillation waveforms at different bias voltages are displayed in Figure 2.5. Harmonic generation and oscillation linewidth will be discussed in detail in the following chapter concerning noise in unpumped junctions.

C. Photon-Assisted Tunneling: Shapiro Steps

When a Josephson junction is illuminated with a coherent source of radiation at frequency ω, the well-known constant voltage steps, predicted by Josephson in his original paper (1962) and first

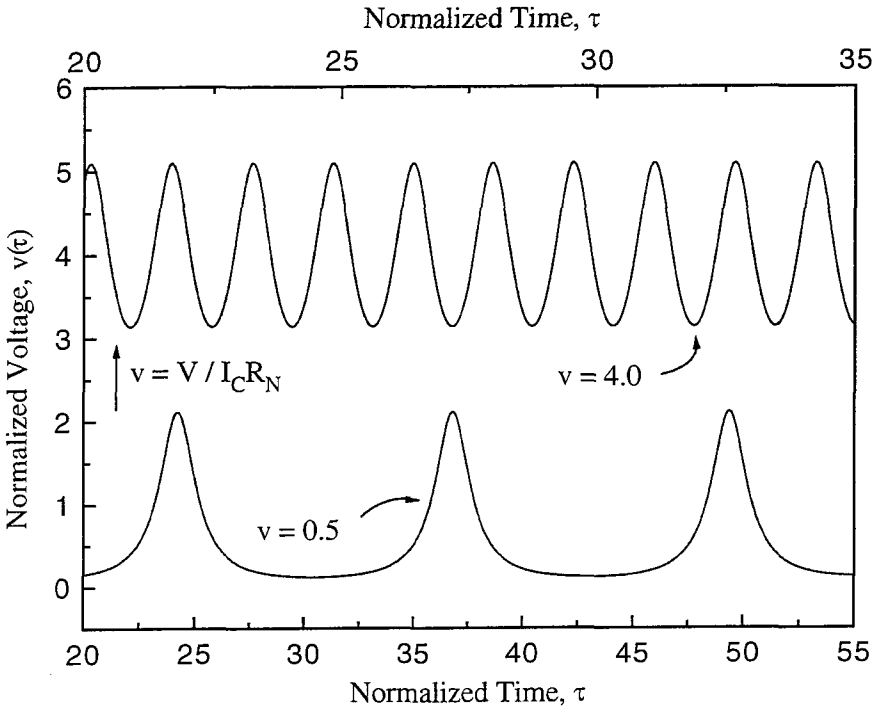

Figure 2.5 Waveforms of normalized voltage versus normalized time obtained by numerical integration of RSJ equation with β_C=0. The lower curve has an average voltage of 0.5, and displays a strongly nonsinusoidal form, with many harmonics. The upper curve has an average voltage of 4.0, and is more nearly sinusoidal.

observed by Shapiro (1963), appear in the current-voltage characteristic at the quantized voltages $V_n = \frac{n\hbar\omega}{2e}$. These steps are due to photon-assisted tunneling of Cooper pairs across the barrier of the junction, or, equivalently, to phase-locking of the internal Josephson oscillations to the applied field. Besides providing a mechanism for several types of high-frequency detectors, this effect has found application in the current definition of the international voltage standard (*e.g.*, Hamilton *et al.*, 1991), since the frequency-to-voltage conversion is proportional to well-known fundamental physical constants, and allows the use of highly accurate clocks and frequency counters.

If a device obeying the Josephson equations (2.5) and (2.4) is acted upon by a constant bias voltage plus an oscillatory component, *i.e.*,

$$V(t) = V_0 + V_\omega \cos(\omega t),$$

and the phase can be calculated by integration,

$$\phi(t) = \phi_0 + \omega_J t + \frac{2eV_\omega}{\hbar\omega}\sin(\omega t).$$

Using (2.4), the current becomes

$$I(t) = I_C \sin[\phi(t)] = I_C \sin[\omega_J t + \alpha \sin(\omega t) + \phi_0],$$

where α is the normalized RF voltage,

$$\alpha = \frac{2eV_\omega}{\hbar\omega}. \tag{2.13}$$

Using the identity for Bessel function series (Abramowitz and Stegun, 1964),

$$I(t) = I_C \sum_{n=-\infty}^{n=+\infty} J_n(\alpha) \sin\left(\frac{2eV_0 t}{\hbar} + n\omega t + \phi_0\right),$$

where the J_n are the integer-order Bessel functions. Here we see that there is a constant current at the quantized voltages where the Josephson frequency, ω_J, is an integer multiple of the frequency of the externally applied voltage; the amplitude of this current is of order $I_C J_n(\alpha)$. We can also see that an imposed signal is "strong," and causes modification of the I-V curve, when $\alpha \gtrsim 1$. To translate this to practical terms, for a 100 GHz signal, this corresponds to a power level of about one nanowatt, assuming a 50 Ohm device impedance. The very low local-oscillator power requirement is a desirable feature of both SIS and Josephson-effect mixers.

2.5. Inclusion of Fluctuations in the RSJ Model

Until now, we have ignored the possibility and the effects of fluctuations and noise, although these must exist even at extremely low temperatures. In this section we will comment on the sources of fluctuations in Josephson junctions. In the following section we indicate the methods by which fluctuation effects can be included into the RSJ formalism, and discuss the calculation of the junction response (*e.g.*, I-V curves) to their presence. The following chapter will be devoted to a more detailed description of the total junction noise and the interaction of the fluctuations with the nonlinearity.

There are several sources of fluctuations which can all be present in a particular realization of a Josephson junction. Since there are dissipative processes occurring in the device (*i.e.*, there is an

effective resistance), the fluctuation-dissipation theorem (Callen and Welton, 1951) tells us that there must be fluctuations associated with this dissipation. In the simplest case, these fluctuations will be the Johnson noise (Johnson, 1928) associated with the resistance in the RSJ model. This Johnson noise is uncorrelated and Gaussian distributed, with a broadband and frequency-independent (or "white") spectrum given by the Nyquist theorem (Nyquist, 1928),

$$S_V(\nu) = 4k_B T R, \tag{2.14}$$

where S_V is the spectral density of the voltage fluctuations, k_B is Boltzmann's constant, and T is the physical temperature of the resistor. These fluctuations can be imagined as a stochastic voltage source in series with the resistor, and their spectrum and magnitude should be unchanged when current flows through the resistor, provided that the temperature is unchanged. The noise can equivalently be thought of as a current source in parallel with the resistor whose current spectral density is

$$S_I(\nu) = \frac{4k_B T}{R}. \tag{2.15}$$

The origin of these fluctuations is the coupling of the charge carriers to the background electromagnetic field. Nyquist discusses the quantum mechanical extension of the noise when the energy per mode is no longer $k_B T$ (*i.e.*, for high frequencies or low temperatures). The quantum-mechanically correct result is given (Callen and Welton, 1951) by

$$S_V(\nu) = 2h\nu R \coth\left[\frac{h\nu}{2k_B T}\right] = 4h\nu R\left[\frac{1}{\exp(h\nu/k_B T) - 1} + \frac{1}{2}\right]. \tag{2.16}$$

The quantity in brackets is the familiar blackbody expression for the occupation number of a boson field, which is the background electromagnetic field to which the device is coupled. The last term is due to the zero-point fluctuations, and is the half-photon per mode present even at zero temperature. It is simple to show that in the low-frequency or Rayleigh-Jeans limit, $h\nu \ll k_B T$, the preceding reduces to the familiar Johnson noise form, (2.14). In the opposite, low-temperature limit, we have

$$S_V(\nu) = 2h\nu R, \tag{2.17}$$

or "quantum" noise, which has a linearly increasing spectrum. An interesting question is whether, in this extreme quantum limit, the fluctuations can be described by Gaussian noise with this simple spectral density, or whether there are higher order non-Gaussian correlations in the noise which must be included. It is useful to note that at liquid helium temperatures, the crossover to the quantum noise regime occurs at high ($\sim$ 90 GHz) frequencies.

Additional complications can arise when some or all of the dissipation is due to a tunneling current. The complete fluctuation spectrum of normal and superconducting tunnel junctions has been calculated, using the tunneling Hamiltonian formalism, by Rogovin and Scalpino (1974). The current spectral density for an SIS junction is

$$S_I(\nu) = eI_{QP}(V_0 + h\nu/e)\coth\left[\frac{eV_0 + h\nu}{2k_BT}\right] + eI_{QP}(V_0 - h\nu/e)\coth\left[\frac{eV_0 - h\nu}{2k_BT}\right], \qquad (2.18)$$

where I_{QP} is the quasiparticle response function (*i.e.*, Werthamer's current response, see Section 1.3) and V_0 is the bias voltage. For low frequencies (*i.e.*, $h\nu \ll eV_0$), this reduces to

$$S_I(\nu) = 2eI_{QP}(V_0)\coth(eV_0/2k_BT). \qquad (2.19)$$

In the low voltage limit of $eV_0 \ll k_BT$, this formula reduces to simple Johnson noise. For an SIS junction $I_{QP}(V_0)$ is simply the bias current of the junction, and so in the opposite limit, ($eV_0 \gg k_BT$),

$$S_I(\nu) = 2eI_{DC}, \qquad (2.20)$$

which is the familiar expression for shot noise. Notice that for a pure tunneling resistance, the crossover from Johnson to shot noise at 4.2 K occurs at $eV \sim k_BT$, or about 0.3 millivolts. Rogovin and Scalapino also calculated the fluctuations in the pair current components, which have very similar form. Even though these currents are dissipationless, they are coupled to the background electromagnetic fields, and therefore exhibit fluctuations.

In this work, however, we will mostly ignore these quantum-mechanical modifications of the simple Johnson noise. First, for the resistively-shunted junctions used in the measurements, the external resistors should be firmly in the Johnson limit except at high frequencies, and the

additional shot noise due to the small subgap tunneling current is negligible in the region of interest below a couple of millivolts of bias voltage. Secondly, we will see that the low-frequency noise is most important in determining the dynamics of the RSJ model, so that the shot-noise and zero-point modifications to the high-frequency spectrum will be less important. Finally, we will see that the Johnson noise interacts with the strong nonlinearities of the RSJ model and produces a large "excess" noise which dominates the performance of the device.

2.6. Solution of the RSJ Model in Presence of Noise

The effects of fluctuations can be included by adding another circuit element to the RSJ model. A stochastic current source, whose fluctuating current will account for the noise of the resistive element, may be added to the bias current in Figure 2.1. The problem of finding solutions to the nonlinear RSJ equations will, however, be complicated by the addition of this term. Analytical solutions for differential equations with stochastic driving terms, known as Langevin equations, can be found via solutions of the Fokker-Planck Equation (FPE) for the probability distribution of the phase. The average rate of change of the phase (*i.e.*, the voltage) can be found through this method in certain limiting cases such as negligible capacitance (Ambegoakar and Halperin, 1969). However, these methods are limited to calculations of autonomous (unpumped) I-V curves, and the response to radiation and mixer performance cannot be calculated in this manner. A good review of FPE methods appears in Barone and Paterno (1982).

Another approach to solution of the general RSJ equation is direct numerical integration of the differential equation. In this method, an integration technique (*e.g.*, Runge-Kutta) is applied to obtain a discretely sampled voltage waveform given a particular (possibly time-dependent) forcing current. This waveform can then be analyzed in several ways. Simple averaging allows calculation of current-voltage characteristics. A Fourier analysis of the time domain solution can give oscillation or noise spectra. Finally, an analysis of the appropriate frequency components in the presence of a biharmonic signal (*i.e.*, a local oscillator and coherent signal) can allow calculation of mixer conversion matrices (this is discussed fully in Section 4.4 on mixer calculations).

The effects of fluctuations can be accounted for in this direct integration method by including the appropriate stochastic driving current in the RSJ equation. For simple Johnson noise, this will be an uncorrelated, Gaussian distributed noise current, whose autocorrelation is given by $< I(t)I(t-\tau) >= \frac{2k_BT}{R}\delta(\tau)$. This method of solving the RSJ model in the presence of noise is sometimes also called a Monte-Carlo method, because the waveform depends on the particular realization of the random forcing term. However, one can obtain valid general results by averaging over an ensemble of realizations of the stochastic process. In the RSJ normalized units, the current noise amounts to selecting a Gaussian current at each integration time step with a variance $\sigma_i^2 = 2\Gamma/\Delta\tau$, where $\Delta\tau$ is the normalized time step. Here Γ is the RSJ noise parameter or dimensionless temperature, introduced in Table 2.1, and defined by

$$\Gamma = \frac{2ek_BT}{\hbar I_C}. \tag{2.21}$$

This parameter can be thought of as the ratio of the thermal energy, k_BT, to the Josephson coupling energy, $\hbar I_C/2e$. The current-voltage curves for several representative values of the Γ parameter, calculated by numerical integration, are displayed in Figure 2.6. The main feature of the inclusion of fluctuations is the rounding of the sharp voltage onset as the current approaches the critical current. Recalling the washboard model analogy, the noise currents will cause random fluctuations in the tilt (DC bias) of the potential. If biased near the critical current, these random noise currents can occasionally allow the particle to slip into the next well of the potential. This creates an average phase change which depends on the frequency of phase slips. Increasing the amplitude of the noise increases the rate of transitions and thus the voltage. At large biases, the effects of these fluctuations is less severe. Finally, for very large noise ($\Gamma \sim 1$), the effects of the wells in the potential are negligible and the nonlinearity is nearly destroyed. The addition of noise tends to reduce hysteresis, increasing the value of β_C at which the curves become double-valued.

2.7. Summary

In this chapter, we have introduced the RSJ model for a Josephson junction and discussed

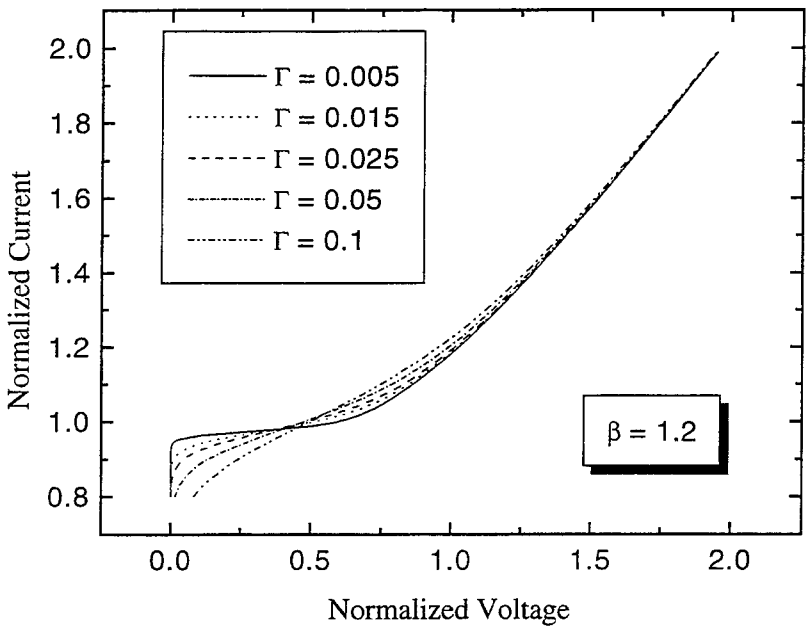

Figure 2.6 Variation of current-voltage characteristics with the addition of thermal fluctuations. Curves for $\beta_C = 1.2$ and for several different values of the dimensionless noise parameter, Γ, are shown.

some of the most basic phenomena exhibited by the model. We have discussed the normalized units used in the RSJ model, and the basic effects of the capacitance (β_C) and noise (Γ) parameters. We have also examined the solutions of the RSJ model for simple DC and RF bias, and given a rough description for the numerical solution of the model in the general case. The washboard model was shown to help provide an intuitive understanding of some of the basic RSJ phenomena. We will refer back to these simple dynamics of the RSJ model in our discussions of excess noise and mixing in the chapters to come.

We should remember that there are some effects which are not included in the model. These include the "dissipative" part of the supercurrent or the pair-quasiparticle interference term (the so-called "$\cos\phi$" term, which is the second term due to pair tunneling found in Werthamer's microscopic theory, *cf.* Section 1.3), the possibility of a non-sinusoidal current-phase relation, and the frequency-dependent form of the Johnson thermal fluctuations. Another important assumption of the RSJ model is that of current bias. Since we only provide a current drive to the model, we ignore the possibility of the nonlinear interaction with the external circuit. Nonetheless, the RSJ model does

exhibit all of the behaviors observed, and provides the basis for the construction and optimization of mixers and other Josephson-effect devices.

Chapter 3

Noise in the Unpumped RSJ Model

All science is either physics or stamp-collecting.

– Lord Kelvin

In this chapter, we will describe the dynamics of the RSJ model in the presence of fluctuations, and the characteristics of the noise when the junction is biased. Although we assume that the only noise input in the model is classical Johnson noise (*cf.* Section 2.5, Equation (2.14)), we will see that the low frequency output noise of the biased junction is always higher than this value. This does not present a thermodynamic contradiction, and is understandable since the device is not in equilibrium when a bias voltage is applied. The phenomenon of noise which is stronger than the expected thermal value has been known as "excess" noise. Results of an RSJ simulation showing the presence of this excess are shown in Figure 3.1. In other fields "excess noise" is often used in reference to 1/f or flicker noise, and while those processes could also occur in real Josephson junctions, it is a separate phenomenon from the excess discussed in this work. Obviously, the value of the junction noise is crucial in determining device performance in a variety of applications. We will therefore begin by describing the theory and later (*cf.* Chapter 6), measurements of the L-band (1.5 GHz) noise of shunted junctions. Since the noise is strongly modified by the nonlinearity of the junction, we will begin our discussion by examining the behavior of the biased junction in the presence of noise.

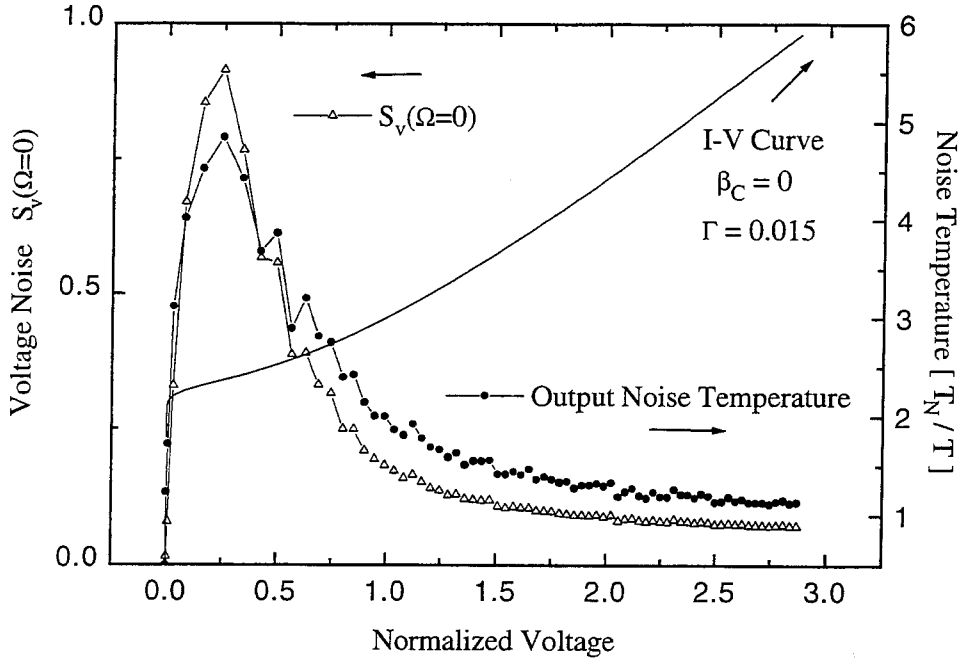

Figure 3.1 Low frequency noise from a Monte Carlo simulation of the RSJ model with $\beta_C = 0.4$ and $\Gamma = 0.015$. Voltage spectral density (in normalized units) as a function of bias voltage is displayed on the left axis. The output noise temperature, determined by the equivalent temperature of a thermal source which produces the same available power as the junction (see text), is displayed on the right axis. The current-voltage characteristic is also shown. The noise shows typical behavior, increasing substantially at bias voltages below the $I_C R_N$ voltage (*i.e.*, $v \lesssim 1$).

3.1. Dynamics of DC Biased RSJ Model in the Presence of Noise

As described earlier (*cf.* Section 2.4.B), a Josephson junction responds to a constant bias by generating oscillations with a frequency proportional to the average bias voltage. Intuitively, we can see that the addition of thermal fluctuations will induce small fluctuations in the bias voltage, and thereby lead to a modulation of the Josephson oscillation frequency. Thus, we expect that the presence of fluctuations will lead to a finite linewidth for the oscillations. If the oscillations are a narrow-band process, then the voltage fluctuations lead to small changes in the phase of the oscillation. This requires that the fluctuations have a broad-band or frequency-independent spectrum, and that the Josephson oscillations have a linewidth small compared to their frequency. Using general fluctuation theory (Stratonovich, 1963), one can show that a sinusoidal oscillation in

the time domain has a Lorentzian spectral profile, and we obtain (Likharev, 1986, p. 106)

$$S_{V_{OSC}}(\nu) = V_k^2 \frac{\Delta_k}{(\nu - k\nu_J)^2 + \Delta_k^2} \tag{3.1}$$

for the oscillation spectrum of the k harmonics, where the V_k are the harmonic amplitudes given in (2.12), and $2\Delta_k$ is the FWHM linewidth of the harmonic. The linewidths are given by

$$\Delta_k = k^2\Delta \qquad \text{and} \qquad \Delta = \frac{1}{8\pi}\left(\frac{2e}{\hbar}\right)^2 S_V(\nu = 0), \tag{3.2}$$

and the halfwidth in normalized angular frequency units, δ, is

$$\delta = \frac{1}{4} S_v(\nu = 0). \tag{3.3}$$

Thus the linewidths are directly proportional to the low-frequency voltage spectral-density of the fluctuations. Assuming that these fluctuations are just due to thermal Johnson noise,

$$\Delta = \frac{1}{2\pi}\left(\frac{2e}{\hbar}\right)^2 k_B T R_N. \tag{3.4}$$

This can be conveniently expressed as a full-width at half-maximum (FWHM) of 40 MHz per Ohm of resistance per Kelvin of temperature. This relatively large linewidth, even at cryogenic temperatures, is one of the major drawbacks of oscillators using the Josephson effect. Also, the low frequency noise will often be significantly larger than the Johnson noise floor. Note, however, that the problem of finding the oscillation linewidth is essentially the same as that of finding the low frequency noise.

We can re-express the oscillation spectrum in normalized units for convenience and for ease in comparison with modelling results. Notice that in normalized units, the oscillation frequency, ω_J, becomes

$$\Omega_J = \omega_J/\omega_C = \frac{2e}{\hbar}\frac{V_{DC}}{\omega_C} = \frac{V_{DC}}{I_C R_N} = v. \tag{3.5}$$

The spectrum then becomes

$$S_{v_{OSC.}}(\Omega) = v_k^2 \frac{\delta_k}{(\Omega - kv)^2 + \delta_k^2}, \tag{3.6}$$

with the linewidth in normalized units of $\delta = \Gamma$, and S_v is the normalized voltage spectral density. In this thesis, we always discuss so-called "one-sided" spectral densities, which are defined only for

positive frequencies. One can also find "two-sided" spectral densities in the literature, but for any physical and therefore real variable, these two-sided spectra contain no new information.

The normalized voltage spectral density for a simple RSJ model with $\beta_C = 0$ and a moderate value for the fluctuation amplitude is shown in Figure 3.2. Several features of this figure which are exemplary should be noted. First, the voltage spectral density is in fact the density per normalized frequency, not per normalized angular frequency (this amounts merely to a scaling by 2π). Second, the Johnson noise floor is indicated, which has a value of 4Γ in these units. The broadened peaks corresponding to the Josephson oscillation and its harmonics are clearly visible, but notice that the combined effect is to increase the low frequency noise (near $\Omega = 0$) to well above the intrinsic Johnson noise floor. Also shown is a fit of a series of harmonically related Lorentzian functions to the spectrum. The harmonic amplitudes extracted from the fit are in excellent agreement with the analytic form (*cf.* Equation (2.12)) predicted above. The scaling of the harmonic linewidths (Equation (3.2)) is also quite good. The results of the fit are summarized below in Table 3.1. The FWHM of the oscillation is found to be exactly half the low-frequency voltage noise, as expected from Equation (3.3). We will now need to examine the question of how to predict the expected linewidth or low frequency noise.

3.2. Low Frequency Noise in the Simple RSJ Model

For the case of small fluctuations and zero capacitance, an analytical expression for the noise spectrum was obtained by Likharev and Semenov (LS, 1972). Their method involves linearizing the RSJ equation with respect to the small fluctuations, Fourier transforming the equation into the frequency domain, and utilizing the analytic forms for the phase and harmonic oscillation amplitudes. The voltage and current Fourier amplitudes, $\tilde{v}$ and $\tilde{i}$, are related by

$$\tilde{v}(\Omega) = \sum_{k=-\infty}^{+\infty} z_k \, \tilde{i}\,(\Omega - kv) \tag{3.7}$$

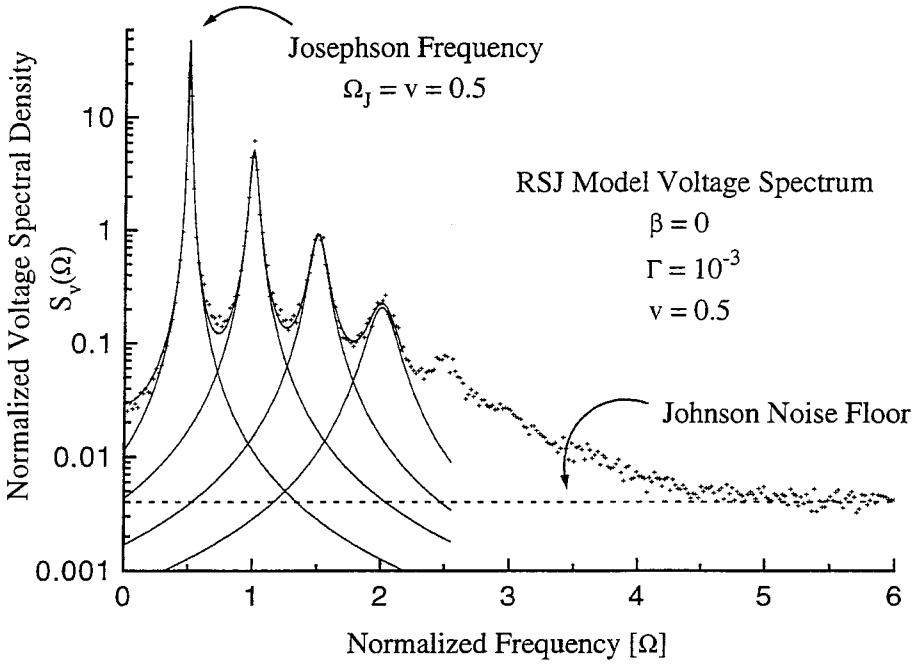

Figure 3.2 Voltage spectral density versus frequency for RSJ simulation with $\beta_C = 0$, $\Gamma = 1 \times 10^{-3}$, and $v = 0.5$. The Josephson oscillation and several harmonics show up clearly. Also shown is a multiple Lorentzian fit to the spectrum. The four harmonic components of the fit are shown separately.

where the z_k's are frequency transformation coefficients (*i.e.*, mixing coefficients) given by

$$z_k(\omega) = \frac{Z_k(\omega)}{R_N} = \delta_{k,0} + \frac{ik\omega_C}{\omega(i+v)^{|k|}} - \frac{1}{2}\left\{\frac{(k-1)\omega_C}{(i+v)^{|k-1|}(\omega+\omega_J)} + \frac{(k+1)\omega_C}{(i+v)^{|k+1|}(\omega-\omega_J)}\right\}. \tag{3.8}$$

The voltage spectral density is then of the form

$$S_v(\Omega) = \sum_{k=-\infty}^{\infty} |\, z_k \,|^2 \, S_i\,(\Omega - kv). \tag{3.9}$$

The z_k's describe the ways in which the Josephson nonlinearity interacts with and changes the intrinsic fluctuation spectrum, and can be thought of as mixing coefficients which take current fluctuations at the frequencies $\Omega - kv$ and convert them to voltage fluctuations at frequency Ω. An equally valid picture is that the fluctuations cause a finite linewidth for the Josephson oscillations and their harmonics, and the Lorentzian tails of these oscillations contribute to the voltage fluctuations at various frequencies. For example, the spectral density at very low frequency in Figure 3.2 can be

TABLE 3.1
FIT TO RSJ OSCILLATION SPECTRUM

	Fundamental	Harmonic 1st	2nd	3rd
Center Frequency [a]	0.50005	–	–	–
Predicted Frequency	0.5	1.0	1.5	2.0
Harmonic Amplitude	0.3865	0.1496	0.0587	0.02422
Predicted Amplitude (v_k^2) [b]	0.382	0.1459	0.0557	0.02128
Linewidth [c]	–	3.91	8.75	16.02
Predicted Linewidth	1	4	9	16

[a] In the fit, the components were forced to be harmonically related, *i.e.*, the harmonics are defined to be multiples of the fitted fundamental frequency.
[b] For this bias voltage, the amplitudes v_k^2 scale as $4v^2/(i+v)^{2k}$, which becomes 0.38197 to the kth power.
[c] These linewidths are scaled to that of the fundamental; the fundamental had a width of 0.01471.

seen to have contributions from the fitted Lorentzian components. The sum of all these harmonics causes the large excess noise.

Likharev and Semenov also show that for frequencies much less than the Josephson frequency, Ω_J, the form of the z_k's leads to a remarkable simplification for the voltage spectral density,

$$S_v(\Omega) = r_d^2 \left[S_i(0) + \frac{1}{2i^2} S_i(\Omega_J) \right], \tag{3.10}$$

where r_d is the normalized differential or dynamic resistance at the bias point, *i.e.*, the slope of the I-V curve. This quantity is given by the simple form

$$r_d = \frac{\partial v}{\partial i} = \frac{\sqrt{v^2+1}}{v} = \frac{i}{v} \tag{3.11}$$

when the I-V curve is given by the analytic form with no fluctuations (*cf.* Section 2.4.A). If the only noise in the junction is simple Johnson noise due to the normal-state resistance, the LS expression is

$$S_v(\Omega) = 4\Gamma r_d^2 \left[1 + \frac{1}{2i^2} \right], \tag{3.12}$$

with the analogous form in dimensioned units,

$$S_V(\nu) = R_d^2 \left[\frac{4k_B T}{R_N} + \frac{I_C^2}{2I^2} S_I(\omega_J) \right] = R_d^2 \left[1 + \frac{I_C^2}{2I^2} \right] \frac{4k_B T}{R_N}. \tag{3.13}$$

Physically, this equation is interpreted as indicating that the low frequency voltage noise is equal to the dynamic resistance squared times the thermal current noise, plus a contribution from the current noise at the Josephson frequency multiplied by some mixing conversion coefficient. Koch *et al.* (Koch, Van Harlingen and Clarke, 1980; Koch, 1982) described the modification of this equation for the case in which the quantum expression for the Johnson noise (*cf.*, Section 2.5) at the Josephson frequency is taken into account. Equation (3.13) then becomes

$$S_V(\nu) = R_d^2 \left[\frac{4k_B T}{R_N} + \frac{2eV}{R_N} \frac{I_C^2}{I^2} \coth \left(\frac{eV}{k_B T} \right) \right]. \tag{3.14}$$

If we introduce the parameter $\kappa = eI_C R_N / k_B T$, then Koch's expression in normalized units is given as

$$S_v(\Omega/2\pi) = 4\Gamma r_d^2 \left[1 + \kappa v \frac{1}{2i^2} \coth(kv) \right]. \tag{3.15}$$

Thus quantum effects should be considered at 4.2 K when $I_C R_N$ is greater than about 350 microvolts.

The low frequency noise of shunted junctions, including these quantum contributions, has been measured by Koch *et al.* (Koch, Van Harlingen, and Clarke, 1981; Koch, Van Harlingen, and Clarke, 1982) in Pb/PbIn junctions. They directly measured the voltage noise at around 100 kHz, well above the range which included any 1/f contributions. They compared their measurements as a function of bias voltage with the expression (3.14), and applied corrections for the observed variations in the dynamic resistance of their devices which were not predicted from the RSJ model. They concluded that the Likharev-Semenov expression yielded a good description of the noise, provided that the correct quantum-mechanical form for the high-frequency Johnson noise (*i.e.*, the hyperbolic cotangent, including the zero-point contribution) was used. In a sense, these experiments used the Josephson junction as a "self-pumped" mixer to examine the spectral density of the Johnson noise at high frequencies. Furthermore, if the presence of the zero-point contribution was verified,

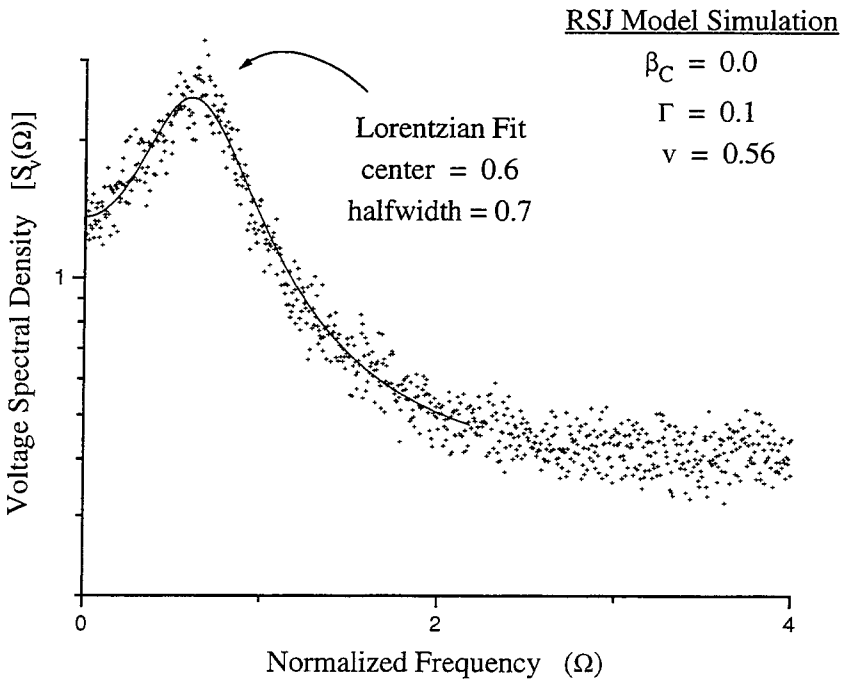

Figure 3.3 Voltage spectral density versus frequency for RSJ simulation with $\beta_C = 0$, $\Gamma = 0.1$, and $v = 0.56$. For this much larger value of the fluctuation parameter, Γ, the Josephson linewidth is comparable to the oscillation frequency. The spectrum cannot be described well as a sum of multiple Lorentzians.

this mixer was near the quantum limit in sensitivity. The self-pumped mixing mode of Josephson junctions has been studied theoretically (Devyatov *et al.*, 1986).

In spite of Koch's sucess in applying the LS model for the noise of the unpumped junction, we should point out some of the assumptions which are strictly required for its validity. Essentially, this LS model will only apply when the frequency conversion coefficients z_k are unchanged from their $\beta_C = 0$, $\Gamma = 0$, simple RSJ form. One condition is that the process is "narrow-band," *i.e.*, the linewidth of the oscillations is small compared to their center frequency. This means that the LS model should break down at low voltages, or equivalently, for sufficiently large fluctuation values. An example of a voltage noise spectrum with relatively large fluctuations is shown in Figure 3.3, which is no longer well described as a sum of discrete Lorentzians. Secondly, the dynamic resistance should remain near its unperturbed value. We saw in Section 2.5 that the I-V curve is significantly rounded by the noise at small voltages (*i.e.*, $v \ll 1$), but there are also modifications at somewhat

larger voltages. Lastly, we need to assume that the junction is current biased at all frequencies, or else the external circuit will affect the z_k's. For example, if there is a low-impedance, resonant circuit in parallel with the junction at some relatively high frequency, this will draw current and reduce the voltage oscillations near this frequency. We will see later (Chapter 7) that this circumstance can also lead to strong modification of the DC I-V curve and the dynamic resistance. Nevertheless, in the next section we will discuss the comparison of RSJ simulations of the I-V curve and low-frequency noise, and we shall see that if the LS model is modified to utilize the dynamic resistance obtained from the simulation, it can give remarkably accurate prediction of the voltage noise, even in regimes where it might not be expected to remain valid.

3.3. RSJ Simulations of Noise and the Likharev-Semenov Model

The Monte-Carlo simulation method can be used to solve the RSJ equations for an arbitrary capacitance and fluctuation level, the low frequency noise can be determined directly from the voltage time series obtained. Current-voltage characteristics and low-frequency noise were calculated using this method by Voss (1981). Both the amount of excess noise (*i.e.*, the maximum value obtained as a function of bias voltage) and its dependence with bias voltage were seen to vary with the capacitance (β_C) and fluctuation strength (Γ). Several RSJ simulations for various values of β_C and Γ, including the I-V curves and low frequency voltage noise as a function of bias voltage, are shown in Figure 3.4. Also shown is the noise predicted by the Likharev-Semenov model (Equation (3.10)), where the dynamic resistance and current have been replaced with the values from the RSJ simulated I-V curves. We have also ignored any frequency-dependent corrections to the resistor's current noise, and assumed that the current noise is simply 4Γ at all frequencies (*i.e.*, we use Equation (3.12) for the voltage spectral density in normalized units), as we have in the RSJ simulations. Clearly, the LS model predicts both the voltage dependence and the magnitude of the noise quite well for a wide range of RSJ capacitance (β_C) and noise (Γ) parameters. The dominant factor in determining the noise is clearly the exact form of the dynamic resistance. However, the noise also includes a mixed-down component which is apparently close to that predicted by the LS model. Although Voss

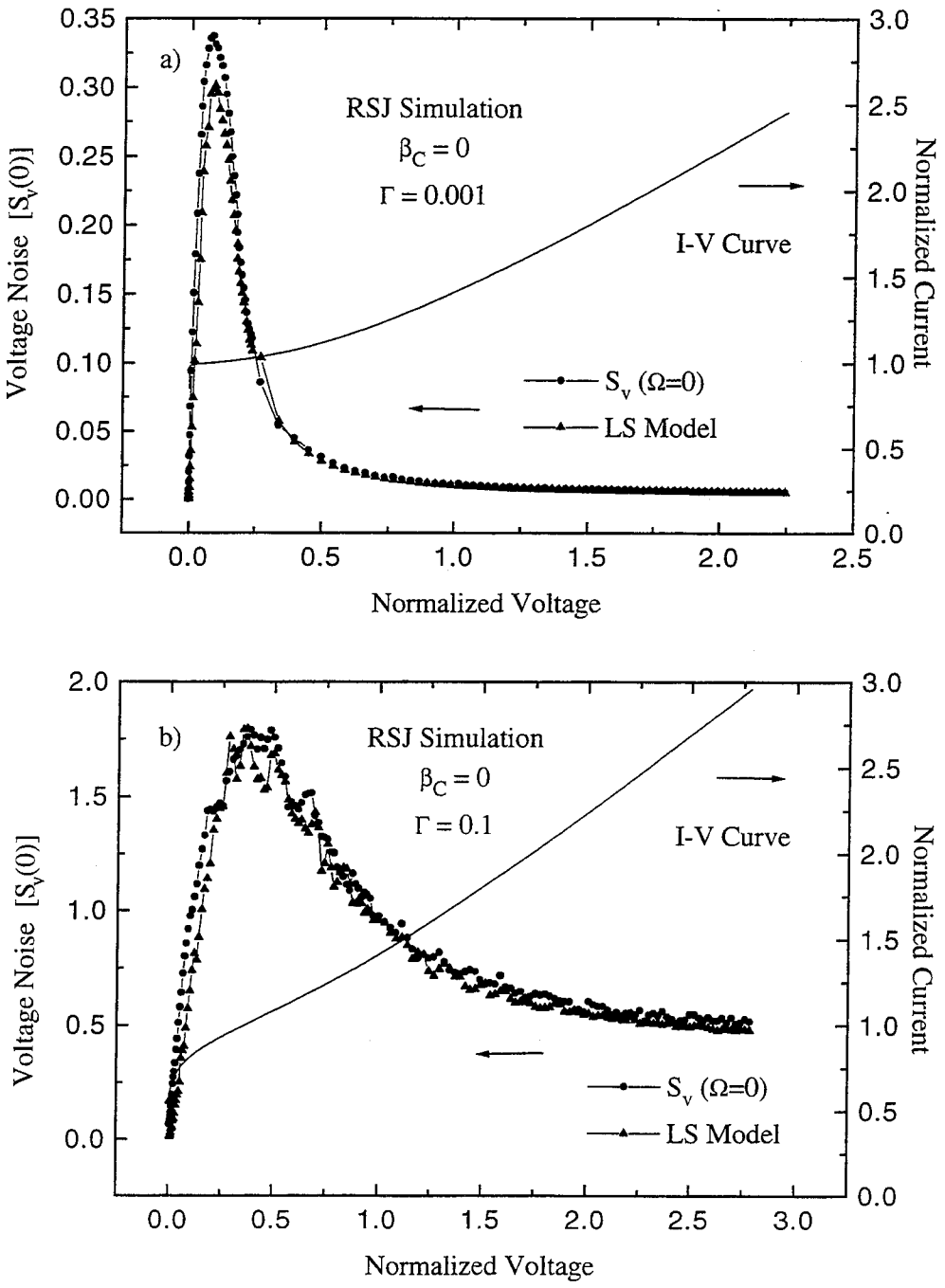

Figure 3.4 Comparison of Likharev-Semenov model for voltage noise with RSJ simulations for various parameters. Current-voltage characteristics (full line) and low-frequency voltage noise (circles) were obtained from RSJ Monte-Carlo simulations. Also displayed is the noise predicted (triangles) by the Likharev-Semenov model (Equation (3.10)), where the dynamic resistance and current are obtained from the simulated I-V curves. a) RSJ with $\beta_C = 0$ and small noise, $\Gamma = 10^{-3}$. b) RSJ with $\beta_C = 0$ and large noise, $\Gamma = 0.1$.

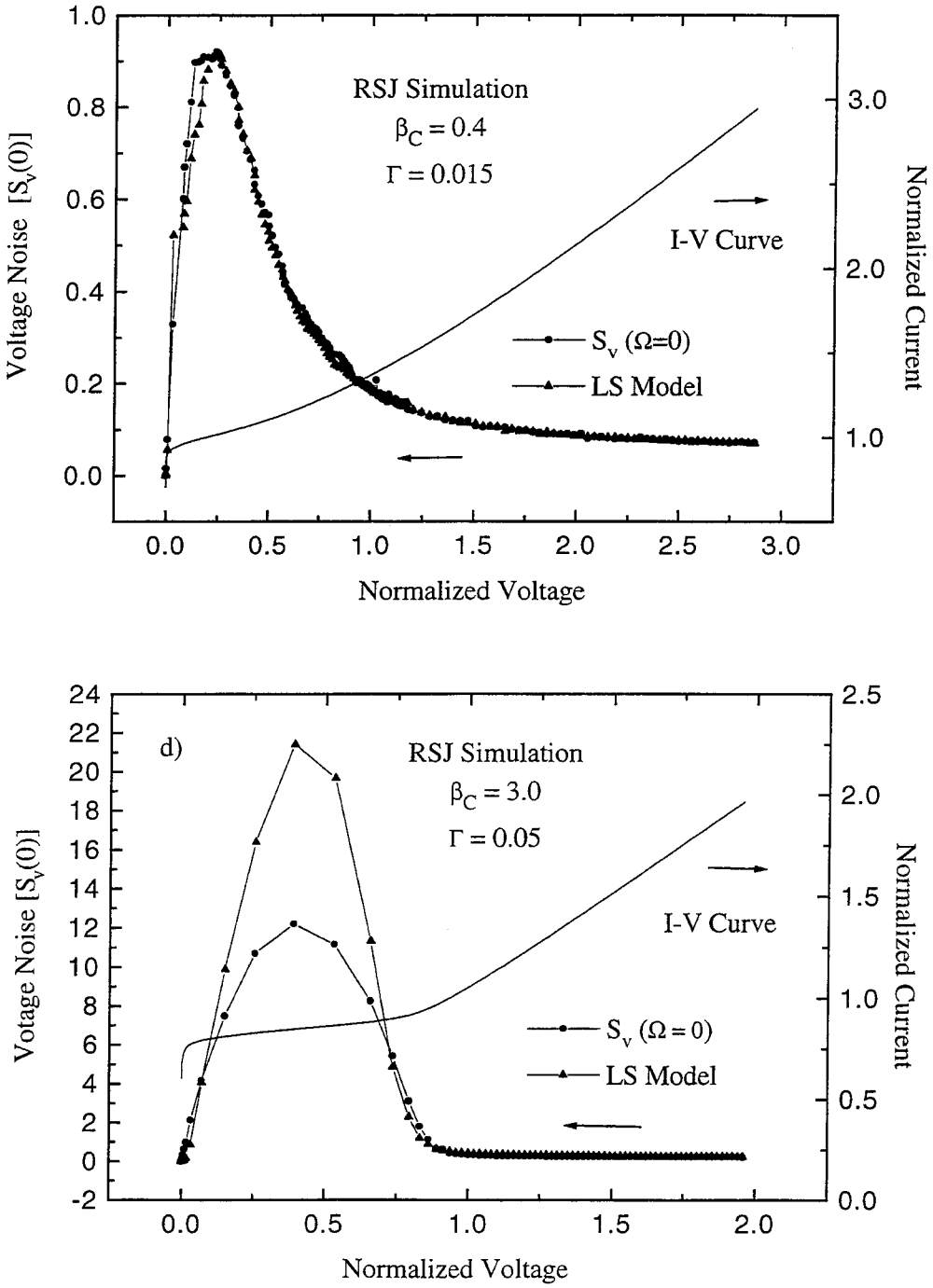

Figure 3.4 — *Continued* Comparison of Likharev-Semenov model with RSJ simulations for c) RSJ with moderate capacitance, $\beta_C = 0.4$ and moderate noise, $\Gamma = 0.015$. d) RSJ with large capacitance, $\beta_C = 3.0$ and moderate noise, $\Gamma = 0.05$.

discussed the modification (to include noise rounded dynamic resistances) of the LS model, he did not show a detailed comparison of the LS model and RSJ simulations.

We do observe, however, that the model becomes inadequate (Figure 3.4d) for sufficiently large ($\beta_C = 3$) values of the capacitance. Although the LS model and the simulation both converge to the thermal limit for very large voltages, the LS model underestimates the noise by about a factor of two for $v \lesssim 0.7$, and then overestimates it by a factor of two (although this is difficult to see in Figure 3.4(d)) due to the linear scale) at higher voltages. In the case of significant capacitance, we expect the Josephson oscillation amplitudes and the entire voltage spectrum will be strongly modified, so the deviation is not unexpected. It is also obvious that the choice of RSJ parameters changes the appearance of the noise-voltage curves. As the Γ parameter is reduced, the noise rounding effects on the I-V curve are lessened, the maximum value of the dynamic resistance increases, and the maximum occurs at smaller bias voltages. This behavior is also displayed in the voltage noise (compare Figure 3.4a and 3.4b). The addition of capacitance generally increases the dynamic resistance and also leads to an increase of the voltage noise.

We would also expect that a variation in the high-frequency impedance seen by the circuit external to the junction itself might alter the noise. We can explicitly add a modification due to a lumped element external circuit to the RSJ equation, and solve the resulting system in an identical manner. The results of such a simulation, in the case in which a series R-L-C combination has been added in parallel to the RSJ circuit, are shown in Figure 3.5. The external circuit was arranged to have a low-impedance (relative to R_N) resonance at a frequency of 1.4 (in normalized units), and the Johnson noise of the real part of the resonant circuit has been included, assuming it is at the same temperature as the junction. We can see from the comparison of the I-V curve with the unperturbed case (*i.e.*, no resonator) in Figure 3.5 that when the junction is biased so that its internal oscillations are at the resonant frequency (*i.e.*, at $v \sim 1.4$), the junction draws additional current. This arises because the junction can better dissipate power at the RF frequency. When we examine the low-frequency noise near the resonance, we see a strong modification due to the changing dynamic resistance near the resonant feature in the I-V curve. One can see from the

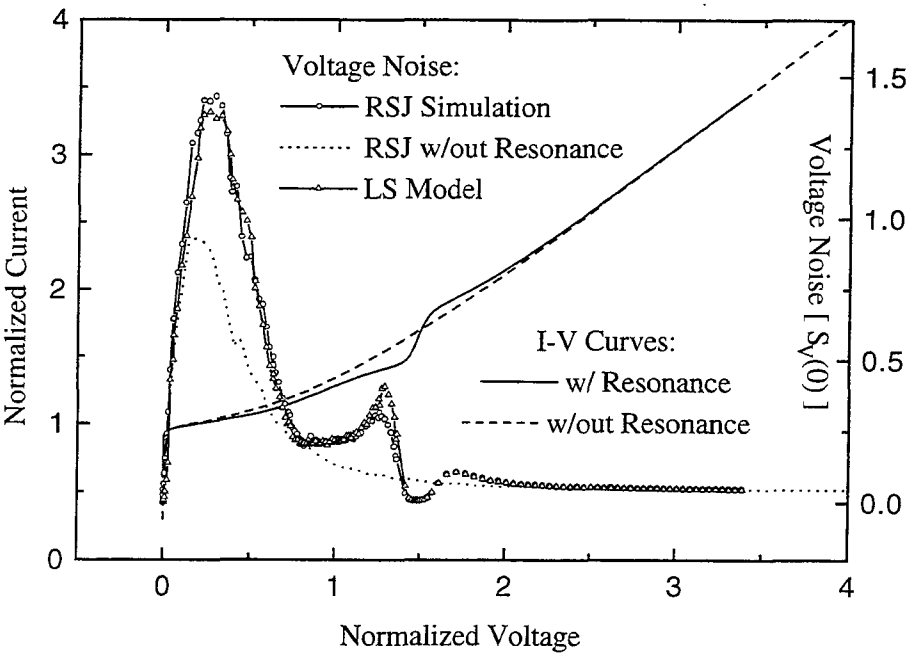

Figure 3.5 Low-frequency noise and I-V curves for RSJ model with an external resonator. A series R-L-C circuit, with a low-impedance resonance at a normalized frequency of 1.4, has been connected in parallel with the junction. The I-V curves of the junction with resonator (full line) and without (dashed line). Circles show voltage noise from RSJ simulation, triangles are the LS model, using the simulated I-V curve. Also shown is the voltage noise from the RSJ simulation without resonator (dotted line). Both RSJ simulations are for a junction with $\beta_C = 0.5$, and $\Gamma = 0.01$.

figure, however, that the LS model cannot completely reproduce the noise, probably because of the modification of the impedance and therefore the mixing coefficients assumed. This is significant, since, as we will see later, it is difficult to arrange coupling structures for Josephson mixers which do not have some resonant structure.

Another, and perhaps more useful, measure of the severity of the excess noise is the available noise power or noise temperature of the device. The available noise power is the maximum amount of power which can be delivered to an external load. If we consider the junction as a noise voltage source with an internal impedance equal to the dynamic resistance, and then equate the available noise power per unit bandwidth with that of a thermal noise source, we obtain the noise temperature, T_N,

$$T_N = \frac{S_V}{4k_B R_d}, \tag{3.16}$$

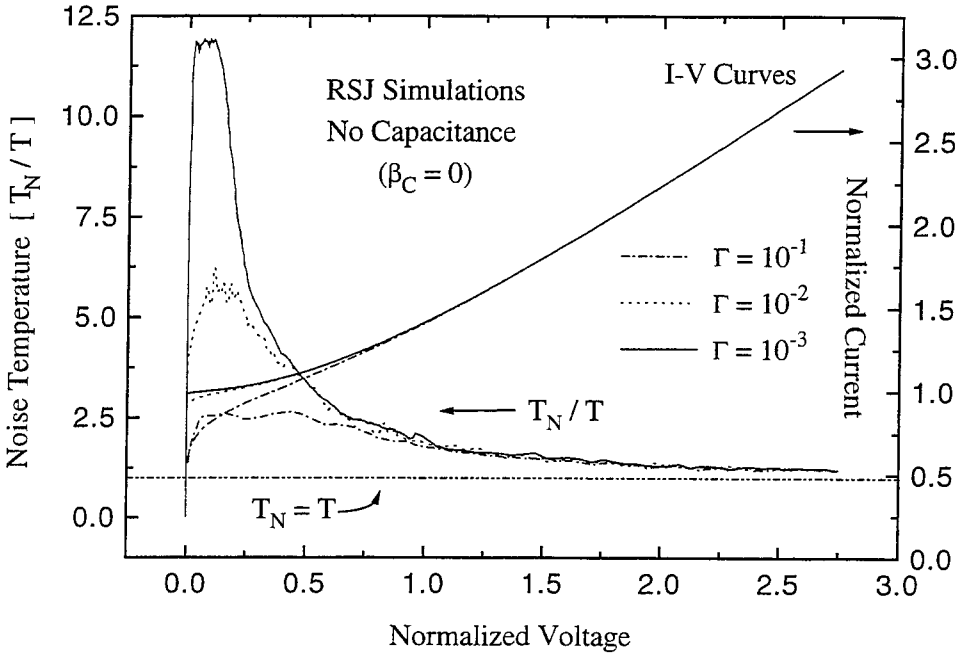

Figure 3.6 Output noise temperature (T_N/T) as a function of bias voltage in the RSJ model for several values of the noise parameter, Γ. Full line is for $\Gamma = 10^{-3}$, dotted line is for $\Gamma = 10^{-2}$, and dash-dotted line is for $\Gamma = 0.1$. The I-V curves for these simulation are also shown. Notice that the excess noise becomes stronger (*i.e.*, T_N/T has a larger maximum value) as Γ decreases. In all cases, the noise temperature approaches the thermal limit with no excess (*i.e.*, $T_N/T = 1$) at sufficiently large bias voltages.

where S_v is the noise spectral density at low frequencies. In normalized units, the corresponding equation is

$$T_N/T = \frac{S_v}{4\Gamma r_d}. \tag{3.17}$$

This dimensionless noise temperature is displayed for several different RSJ simulations, with different values of the Γ parameter, in Figure 3.6. At large bias voltages, the dynamic resistance approaches the normal state resistance ($r_d \rightarrow 1$), the voltage noise approaches the pure Johnson noise limit ($S_v \rightarrow 4\Gamma$ in normalized units), and the noise temperature nears the physical temperature (*i.e.*, $T_N/T \rightarrow 1$). We can see that the noise temperature can be substantially greater than one for small values of the fluctuation parameter, Γ. Because the dynamic resistance and the nonlinearity become stronger for smaller fluctuations, the enhancement of the noise is more prominent. Vystavkin *et al.* (1974) discuss the scaling of the maximum dynamic resistance with the fluctuation strength. They

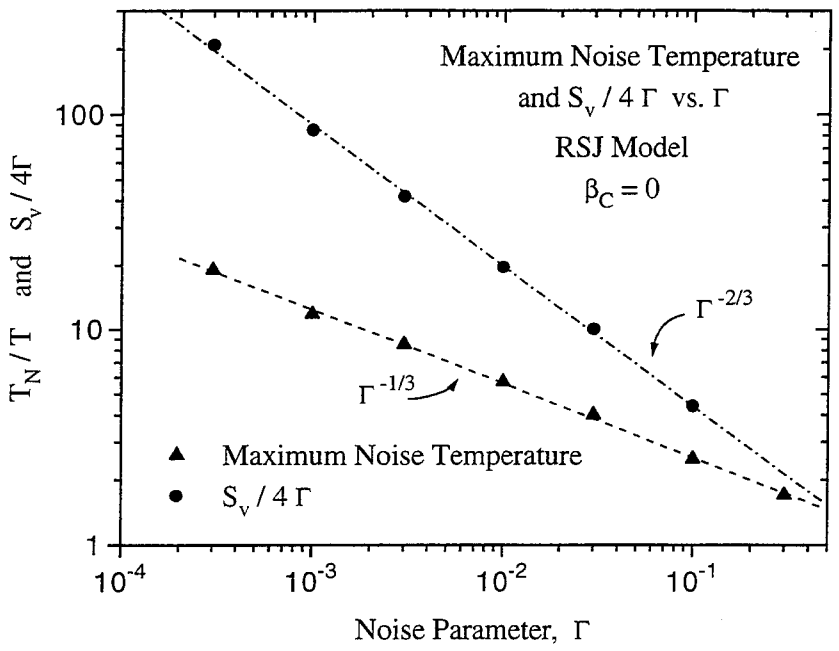

Figure 3.7 Scaling of maximum output noise temperature (triangles) and maximum voltage noise ($S_v(0)/4\Gamma$, circles) with the noise parameter, Γ. We expect, based on the LS model, that $S_v/4\Gamma$ should scale roughly as the dynamic resistance (r_d) squared, while T_N/T should scale as r_d. The lines show the best-fit power law dependences, $\Gamma^{-1/3}$ and $\Gamma^{-2/3}$. The observed scaling agrees well with the prediction that the maximum dynamic resistance should scale as $\Gamma^{-1/3}$ (see text).

derived the scaling from the analytical Fokker-Planck solutions of the RSJ model, with noise and no capacitance, of Ambegoakar and Halperin (1969). Vystavkin's finding is that the maximum dynamic resistance scales as $\Gamma^{-1/3}$ for small values of gamma. If this is true, the LS model would predict a scaling of S_v should be roughly as r_d^2, or $\Gamma^{-2/3}$. The scaling of T_N/T ($\sim S_v/r_d$) should be roughly as $\Gamma^{-1/3}$. The scaling of T_N/T and $S_v/4\Gamma$ with respect to Γ, as determined from RSJ simulations with β_C=0, is shown in Figure 3.7. The lines show fitted power law dependences, and are in excellent agreement with this prediction.

The overall scale of the noise, of course, becomes smaller as the input fluctuations are reduced. However, the importance of the excess noise relative to the thermal fluctuations becomes greater. This initially counterintuitive finding makes sense based on our understanding of the source of the excess noise. The excess noise is caused by the tails of the AC Josephson oscillations, and the

amplitude of the Josephson oscillations is fixed, while the amplitude of the thermal fluctuations is proportional to Γ. We will return to this issue of noise scaling in the pumped RSJ model in regard to noise temperatures and optimization of Josephson mixers in Chapter 5. The excess noise in the unpumped RSJ model is most important at low voltages, where the AC Josephson oscillation frequency is low, the dynamic resistance is high, and thus the linewidth is large. The Likharev and Semenov model for the noise is seen to reproduce the size and voltage dependence of the noise, provided that the current-biased assumption (*i.e.*, the impedance of the linear part of the circuit is R_N at all relevant frequencies) is not broken by the addition of large capacitance or a high-frequency resonance. We will compare direct measurements of the noise in resistively-shunted junctions with the LS model and the expected excess noise in Chapter 7.

Chapter 4

Dynamics of the Pumped RSJ Model

So long ago when we were taught, that for whatever kind of puzzle you got, just stick the right formula in - a solution for every fool.

– the Indigo Girls, *Least Complicated*

Having discussed the dynamics of the basic RSJ model and the nature of the "excess" noise seen in the unpumped case, we will now examine the behavior of the RSJ model under illumination from a coherent source. An understanding of this "pumped" case is obviously necessary to discuss Josephson mixing and the potential for submillimeter heterodyne detectors. We will first outline the basic results and discuss the dependence on the various RSJ parameters. Then a brief discussion of the mixing mechanism and a simple analytical treatment of mixing is given. Next we describe the more rigorous technique of three-port mixer modelling and outline the procedure used to obtain three-port noise and conversion matrices from the RSJ Monte Carlo simulations. The final section shows the results of these calculations, and the behavior of the matrix elements on the bias and RSJ parameters. Chapter 5 then proceeds to deal with the origin and nature of the excess noise in these mixers, and discusses the implications of this understanding for Josephson mixers.

4.1. Basic Behavior of Pumped RSJ Model

In response to illumination with a monochromatic source, a Josephson-effect device develops

constant-voltage peaks in the current-voltage characteristic, known as Shapiro steps, which were discussed briefly in Chapter 2. The steps occur at the quantized voltages,

$$V_n = n\frac{h\nu}{2e}, \tag{4.1}$$

which are proportional to the frequency of the incident radiation. These peaks are due to photon-assisted tunneling of the Cooper pairs in the superconductor, each with a charge of twice the electron charge (2e). An alternative description, in terms of phase-locking to the source, can be made using the RSJ model. We saw in Chapter 2 that the DC voltage-biased RSJ model produced oscillations with a frequency proportional to the voltage, *i.e.*, $\nu_J = 2eV_{DC}/h$. This means that the internal Josephson oscillations are at exact multiples of the incoming radiation frequency when biased on the Shapiro steps at the voltages given in Equation (4.1). Here, the internal oscillations are phase-locked to the external signal for some range of driving current, and are kept at a single frequency and therefore at a single voltage, which results in a vertical step in the I-V curve.

Between the vertical Shapiro steps, the I-V curve connects these steps in a smooth way (for non-hysteretic devices), whose exact shape can be difficult to calculate. We can solve the RSJ equation numerically in the time domain and replace the constant bias current in Equation (2.9) with a combination of a DC and an oscillatory term. Unfortunately, no analytical solutions such as those for the unpumped RSJ model of Ambegaokar and Halperin (1969, *cf.* Section 3.3) are known for the pumped RSJ model in the presence of noise. Example I-V curves for the driven RSJ model with no capacitance ($\beta_C = 0$) and several different pump frequencies are shown in Figure 4.1. Two additional parameters, the normalized RF driving current, i_{LO}, and the normalized local oscillator frequency, Ω_{LO}, are required to specify the driving used. Notice that in normalized units, the Shapiro steps appear at a normalized voltage equal to the normalized frequency. In Figure 4.1, the LO current in each case has been adjusted so that the zeroth-order Shapiro step (*i.e.*, the critical current) is about half its unpumped value. The I-V curves are symmetric about the origin as in the case of the unpumped RSJ model.

We can see that the shape of the region between the vertical steps, sometimes referred to as

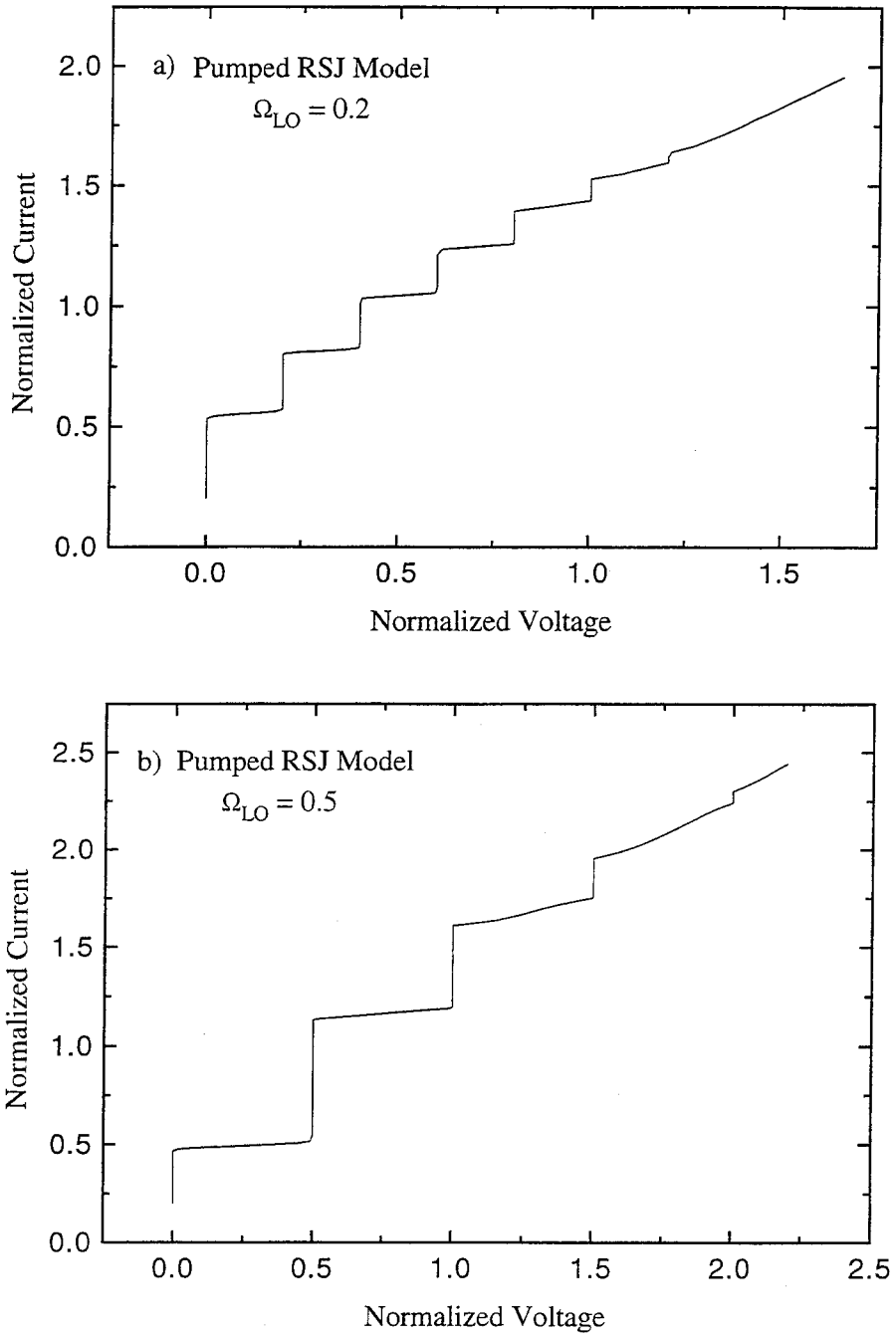

Figure 4.1 Pumped I-V curves for RSJ model with no capacitance ($\beta_C = 0$) and small noise ($\Gamma = 3 \times 10^{-4}$). The local oscillator current has been adjusted in each case to give a roughly 50% suppression of the critical current. a) For a local oscillator frequency of $\Omega_{LO} = 0.2$. b) For a local oscillator frequency of $\Omega_{LO} = 0.5$.

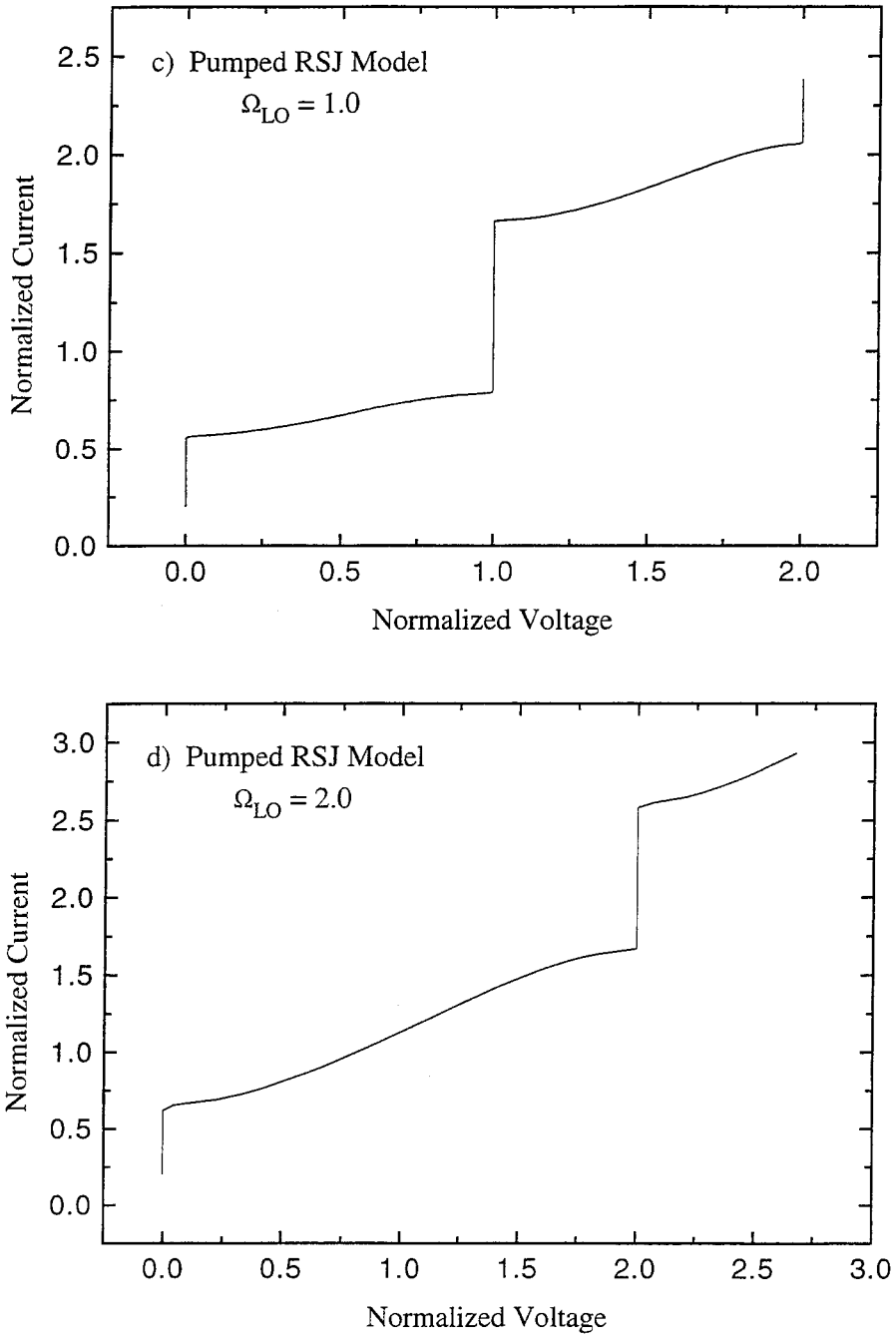

Figure 4.1 –*Continued.* Pumped I-V curves for RSJ model. c) For a local oscillator frequency of $\Omega_{LO} = 1.0$. d) For a local oscillator frequency of $\Omega_{LO} = 2.0$.

the "risers," varies depending on the RF frequency. The differential resistance between the steps is very large for small normalized pump frequencies, while there is a minimum at the midpoint of the riser for larger frequencies. In fact, for very large drive frequencies (*e.g.*, Figure 4.1d), each Shapiro step is reminiscent of the shape of the unpumped RSJ model I-V curve (*cf.* Figure 2.3). For high driving frequencies, $\omega_{LO} \gg \omega_C$ or $\Omega_{LO} \gg 1$, this can be made more quantitative by considering the phase of the junction as composed of a rapidly varying part which advances linearly at the rate given by the DC voltage, $\dot{\phi} = \frac{2e}{\hbar} V_{DC}$, and a slowly-varying part which is the deviation from this linear increase. This so-called "slowly-varying phase" (SVP) approximation is discussed in more detail by Likharev (Likharev, 1986; Likharev and Kuzmin, 1977). Essentially, by averaging over the "fast" (*i.e.*, $t \sim 1/\omega_{LO}$) behavior, one can obtain reduced equations for the evolution of the slow phase deviation. These equations become identical to the original RSJ equations, with the addition of a current and voltage offset equal to the center of the Shapiro step, and the modifications that the critical current is replaced by the Shapiro step height and the normal-state resistance is replaced by the differential resistance of the unpumped junction. Since the Shapiro step height is less than the full critical current, the hysteresis (β_C) parameter for this equation is reduced, while the noise parameter (Γ) is increased for the same reason. We thus expect that the effect of fluctuations on the Shapiro steps will be a rounding of the I-V curve near the steps. Likewise, we expect that hysteresis near the steps will be possible for sufficiently large values of the capacitance. A typical series of I-V curves for different values of the noise parameter, Γ, are shown in Figure 4.2.

An I-V curve showing hysteretic behavior between the Shapiro steps is shown in Figure 4.3. Another important feature of the pumped RSJ model with β_C greater than 1 is the possibility of bifurcations, sub-harmonic locking, and chaos. A small subharmonic step is visible in Figure 4.3 at a voltage of 0.75, between the first and second Shapiro steps. Several studies of the chaotic RSJ model have been made (Octavio, 1984; Kautz, 1981) and the equation has also been extensively studied under the guise of the damped, driven pendulum (whose equation of motion is identical to the RSJ equation, *cf.* Section 2.3). The dependence of the behavior on the various RSJ parameters in this regime is very complicated. Small changes in the LO pump current, for example, can shift the

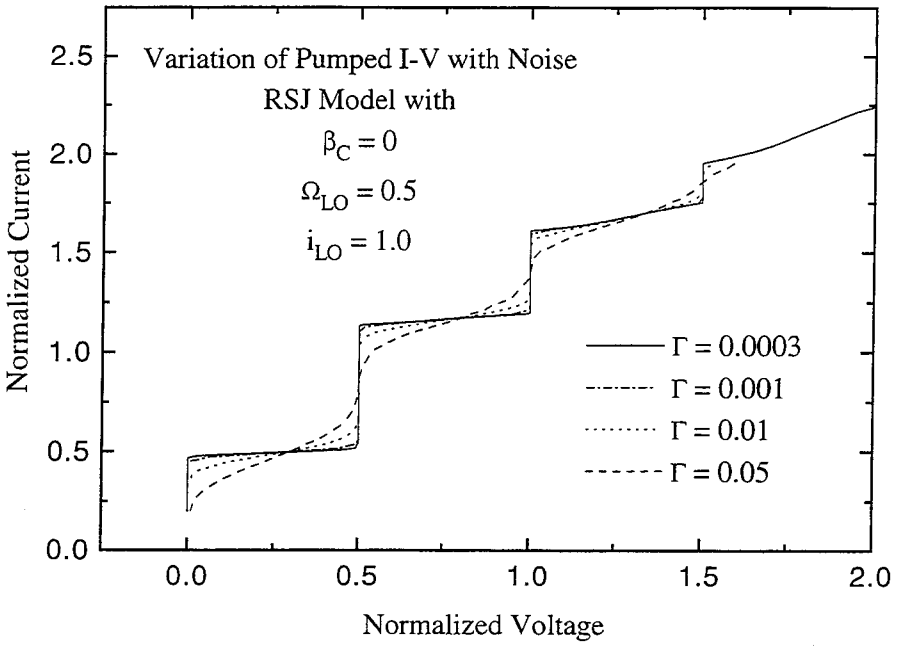

Figure 4.2 Variation of pumped I-V curves with noise parameter, Γ. Several curves with no capacitance and a pump frequency of 0.5 are shown. The effect of the fluctuations is similar to that in the unpumped RSJ model, where all the Shapiro steps are rounded in a manner similar to the critical current.

model from periodic solutions to a chaotic state and then back to a bifurcated regime. In addition, we expect that the noise performance of a mixer under these conditions would be severely degraded. For this reason, and because of the complications of dealing with calculations of mixer performance when the I-V curves are double-valued, we will confine the remaining discussions and calculations on mixers to the case of small to moderate capacitance (*i.e.*, β_C less than or equal to about one).

4.2. Qualitative Discussion of Josephson Mixing

Armed with a basic idea of the junction's response to the local oscillator illumination, we can give a rough description of how the mixing process occurs in Josephson devices. The following picture of Josephson mixing, in which the pumped I-V curve leads to a view of the junction as a fast video detector, was initially discussed by Grimes and Shapiro (1968), who also performed some of the first millimeter-wave Josephson mixing experiments. An I-V curve for three slightly different local oscillator strengths is shown in Figure 4.4. As the pump current is increased, the size of the

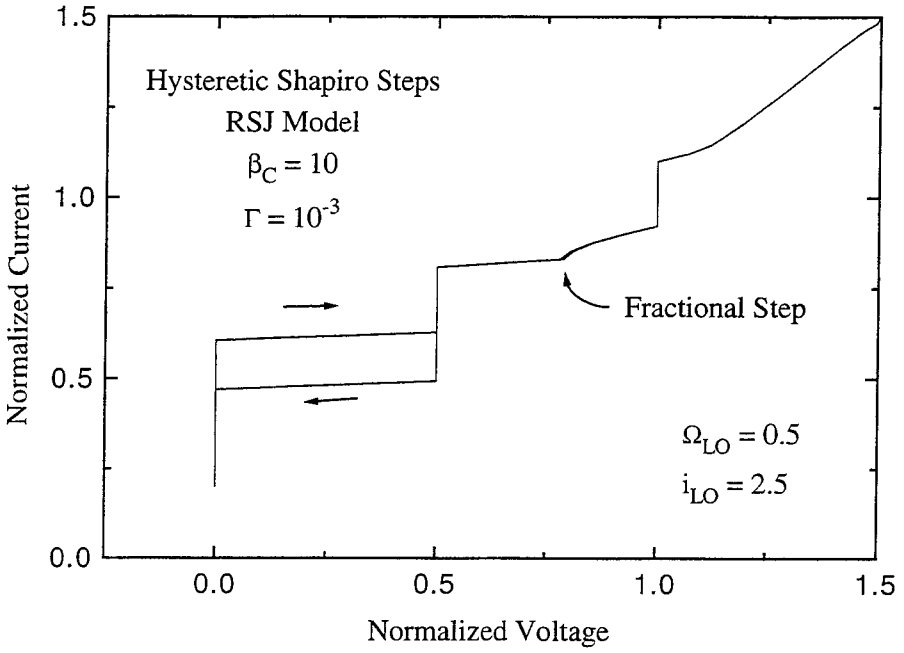

Figure 4.3 Pumped RSJ I-V curve for large capacitance, showing hysteresis of region between the Shapiro steps. For this simulation, $\beta_C = 10$, $\Gamma = 10^{-3}$, $\Omega_{LO} = 0.5$, and $i_{LO} = 2.5$. The region of the I-V curve between the zeroth and first Shapiro steps is double-valued. In addition, a small fractional Shapiro step can be seen at $v = 0.5$, between the first and second steps. Such subharmonic locking and chaotic behavior are possible for the pumped RSJ model with $\beta_C \gtrsim 1$.

critical current decreases, while the height of the first Shapiro step (at $v = 0.5$) increases. If we imagine adding a small signal at a slightly different frequency from the local oscillator, this will lead to "beating" with the local oscillator. The combination of the two oscillations (LO and signal) is equivalent to an amplitude modulation of the LO at the difference frequency. The modulation of the LO will in turn lead to a modulation of the I-V curve (if it could be traced quickly enough) between the three similar curves shown in Figure 4.4. If we imagine using a constant-current bias to hold the junction at the bias point indicated, then this modulation of the I-V characteristic will lead to a large accompanying voltage swing at the desired difference frequency. Thus the junction acts as a mixer, with a conversion efficiency which is large between the Shapiro steps.

This simple picture can be used to make a crude estimate of the expected conversion efficiency, which is defined as the ratio of the available RF signal power to the available power at the

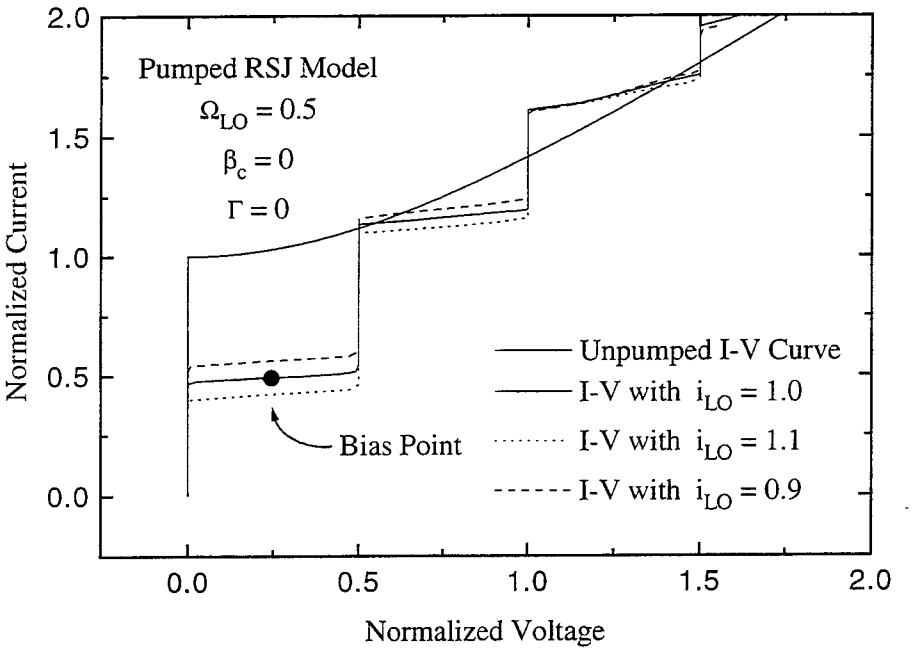

Figure 4.4 Variation of Shapiro steps and I-V curve with local oscillator strength (i_{LO}). As the pump strength is increased, the size of the critical current (*i.e.*, the height of the zeroth Shapiro step) decreases. Also shown is the nominal bias point for best mixing response (see text).

intermediate (difference) frequency (IF). The following treatment has been reproduced several times (see, for example, Van Duzer and Turner, 1981). If we assume that the junction is connected to matched loads at the RF input and the IF output, then the voltage swing in the IF load is given by

$$V_{IF} = \frac{R_d I_s}{2} \frac{\partial I_C}{\partial I_{LO}}, \tag{4.2}$$

where I_s is the signal current supplied, and both the junction and the load at the IF frequency have the impedance R_d, which, since the frequency is small, is the slope of the I-V curve at the operating point. The available RF power is simply

$$P_{RF} = \frac{1}{8} I_s^2 R_s, \tag{4.3}$$

while the power dissipated in the matched IF load is

$$P_{IF} = \frac{V_{IF}^2}{2R_d} = \frac{R_d I_s^2}{8} \left(\frac{\partial I_C}{\partial I_{LO}} \right)^2. \tag{4.4}$$

The conversion efficiency, η_C, is then given by

$$\eta_C = \frac{R_d}{R_s}\left(\frac{\partial I_C}{\partial I_{LO}}\right)^2. \tag{4.5}$$

Note that the quantity $\partial I_C/\partial I_{LO}$ actually refers to the change in the current at the chosen bias point. This simple treatment thus reduces the calculation of the conversion efficiency to a calculation of the I-V curve and the dependence of the Shapiro step heights (or, more accurately the dependence of the "riser" portion of the I-V curve) on local oscillator strength. We have seen that the detailed shape of I-V curve for the pumped RSJ model is difficult to calculate. In addition, we have only discussed the case of the RSJ model driven with a constant-current source so far. In general, the impedance with which the LO is provided to the junction affects the shape of the I-V curve, as well as the dependence of the step heights. The dependence on LO impedance is discussed later in this chapter.

Nonetheless, we can use the expression above (Equation (4.5)) to make an order of magnitude estimate for the conversion efficiency of a Josephson mixer. In Chapter 2, we saw that the Shapiro step height dependence for a voltage source at the RF became a Bessel function of the dimensionless parameter $\alpha = 2eV_{RF}/\hbar\omega_{LO}$. If we therefore say that the critical current changes by a total of I_C when α varies up to about one, then the corresponding change in the LO current is $\Delta I_{LO} \sim I_C \frac{\hbar}{2e}\frac{\omega_{LO}}{I_C R_N} \sim I_C\,\Omega_{LO}$. Then the conversion efficiency would be roughly

$$\eta_C \simeq \frac{R_d}{R_s}\frac{1}{\Omega_{LO}^2}. \tag{4.6}$$

The ratio R_d/R_s can be a few (since we expect R_s to be of order R_N, but since R_d can be greater than R_N), and thus the conversion efficiency can be large for normalized LO frequencies less than about one. Furthermore, we expect the conversion efficiency and the overall mixer performance to deteriorate as the square of the frequency for frequencies much greater than the critical frequency, ω_C. The conversion should be most efficient between the Shapiro steps, and should of course vanish on the steps themselves, where the dynamic resistance and the I-V variation with LO power both vanish. Since the higher-order steps are generally smaller, their variation with LO power is smaller.

Thus the conversion on these steps should be smaller, so that best performance is expected between the zeroth and first Shapiro steps. Likewise, based on the damped oscillatory behavior (*cf.* Chapter 8 for plots of the step height versus LO power) of the step heights, the conversion should be greatest for a local oscillator power less than that required for the first minimum of the critical current, when it has been suppressed by about 50%. We will see in Chapter 8 that the observed behavior of Josephson mixers using shunted junctions follows these general predictions quite closely.

4.3. Conversion Matrices and the Three-Port Model for Mixers

In this section, we will describe the general theory of mixers and the analysis of mixer noise and conversion efficiency using the conversion and noise correlation matrices, without specific reference to Josephson mixers. The following section will detail the procedure by which the noise and conversion matrices were obtained from the RSJ model, and their use to calculate mixer performance. The treatment herein is described in several places, including the famous work by Torrey and Whitmer (1948). The basic idea of the analysis is to obtain a linear, small-signal response matrix for the mixer by solving the nonlinear problem of the mixing element under LO illumination. The mixer is then described as a linear network, whose various ports correspond to the different frequencies of interest. The matrix relating the signals at one port to those at another port is known as the conversion matrix, and contains information about how frequencies are converted in the specific nonlinearity of the mixer. The noise correlation matrix describes the noise spectral densities at the various input ports (*i.e.*, frequencies) of the mixer and their respective correlations. Once the noise and conversion matrices are known for a particular mixer, simple linear network theory allows the calculation of conversion efficiency and mixer noise temperature as a function of the external circuit impedances. Even though any mixer is an inherently nonlinear device, this linear analysis (which is performed after a full nonlinear, large-signal analysis in order to determine the matrices) should be valid provided that the signal itself is small enough that it can be treated linearly.

Although one can consider a large number of frequencies due to possible harmonics of the local oscillator and the various combinations of the signal and intermediate frequencies, it is customary

to confine the matrices to deal with a limited number of frequency ports. In practice, this is reasonable since parasitics or other aspects of the physical system eventually terminate high-order harmonics. We will consider the so-called "three-port" approximation, and only concern ourselves with combinations of the intermediate frequency, ω_0, and the two signal frequencies, $\omega_{LO} + \omega_0$ and $\omega_{LO} - \omega_0$. It is obvious that signals at either of these two frequencies, or "sidebands," will lead to down-converted signals at the IF, ω_0. Because the intermediate frequency is small in comparison to the LO frequency, the impedances and coupling to both the upper ($\omega_{LO} + \omega_0$) and lower ($\omega_{LO} - \omega_0$) sidebands are usually the same. Such a mixer which is sensitive to either high frequency is known as "double-sideband."

The small-signal voltages and currents will therefore be considered at the intermediate frequency and the upper and lower sidebands. We can write the small-signal voltage, V_{ss}, as

$$V_{ss} = \Re e \left[V_{USB}\, e^{\jmath(\omega_{LO}+\omega_0)t} + V_0\, e^{\jmath\omega_0 t} + V_{LSB}\, e^{\jmath(\omega_{LO}-\omega_0)t} \right]. \tag{4.7}$$

Restricting ourselves to small enough signals such that linearity holds, we can relate the voltages to the currents,

$$\begin{pmatrix} V_{USB} \\ V_0 \\ V^*_{LSB} \end{pmatrix} = \begin{pmatrix} Z_{UU} & Z_{UO} & Z_{UL} \\ Z_{OU} & Z_{OO} & Z_{OL} \\ Z_{LU} & Z_{LO} & Z_{LL} \end{pmatrix} \begin{pmatrix} I_{USB} \\ I_0 \\ I^*_{LSB} \end{pmatrix}, \tag{4.8}$$

or more compactly,

$$\tilde{V} = \tilde{\tilde{Z}}\,\tilde{I}. \tag{4.9}$$

This equation is identical in normalized RSJ units when the Z's are normalized to R_N and the V's and I's are normalized in the usual way. A linear circuit would have a matrix which was purely diagonal, and of course would not be capable of mixing. If the conversion matrix is symmetric about its diagonal, time-reversal holds and the device is reciprocal. Josephson mixers are neither passive nor reciprocal, so, for instance, the up-conversion and down-conversion need not be equal (*i.e.*, $Z_{UO} \neq Z_{OU}$). However, in the limit that the intermediate frequency, ω_0, is small (*i.e.*, $\omega_0 \ll \omega_{LO}$),

the following general symmetry relations for the conversion matrix, $\tilde{\tilde{Z}}$, should hold,

$$\begin{aligned} Z_{OL} &= Z_{OU}^* \qquad & Z_{LU} &= Z_{LU}^* \\ Z_{LO} &= Z_{UO}^* \qquad & Z_{LL} &= Z_{UU}^*. \end{aligned} \tag{4.10}$$

In addition, we can choose the phase of the local oscillator (or the time origin) such that the second row of the matrix is purely real. Torrey and Whitmer describe the way in which the conversion matrix elements can be determined by calculation of the DC and LO voltages and their dependence on the LO power, which requires the solution of the nonlinear pumped case for the specific nonlinearity being considered.

We can now include the external part of the circuit in order to determine the conversion efficiency. We connect the impedances Z_U, Z_L, and Z_O to the mixer inputs, and we place a voltage generator with amplitude V_{SIG} in series with Z_U at the upper sideband port. By summing the voltages at the output ports of the mixer, we then obtain the following equation

$$\begin{pmatrix} V_{USB} \\ V_0 \\ V_{LSB}^* \end{pmatrix} + \begin{pmatrix} Z_U & 0 & 0 \\ 0 & Z_O & 0 \\ 0 & 0 & Z_L \end{pmatrix} \begin{pmatrix} I_{USB} \\ I_0 \\ I_{LSB}^* \end{pmatrix} = \begin{pmatrix} V_{SIG} \\ 0 \\ 0 \end{pmatrix}, \tag{4.11}$$

or

$$\tilde{V} + \tilde{\tilde{Z}}_{EXT} \cdot \tilde{I} = \tilde{V}_{SIG}. \tag{4.12}$$

We can then invert to find the current,

$$\tilde{I} = \left(\tilde{\tilde{Z}} + \tilde{\tilde{Z}}_{EXT} \right)^{-1} \cdot \tilde{V} = \tilde{\tilde{Y}} \cdot \tilde{V}, \tag{4.13}$$

where $\tilde{\tilde{Y}}$ is the total admittance matrix, whose elements follow the same naming convention as the conversion matrix $\tilde{\tilde{Z}}$. It is now possible to calculate the available power at the input and the total power delivered to the IF load. The available RF power is simply

$$P_{RF} = \frac{1}{8} \frac{|V_{SIG}|^2}{\Re e(Z_U)},$$

and the power dissipated in the IF load is

$$P_{IF} = \frac{1}{2} |I_0|^2 \Re e(Z_O) = \frac{1}{2} |Y_{OU} V_{SIG}|^2 \Re e(Z_O).$$

The conversion efficiency, η_C, is therefore

$$\eta_C = 4 \Re e(Z_O) \Re e(Z_U) |Y_{OU}|^2. \tag{4.14}$$

Noise can be included by adding a fluctuation voltage vector, $\widetilde{\delta V}$, to the right-hand side of Equation (4.8). We can then define the noise correlation matrix, $\widetilde{\widetilde{S}}$,

$$\widetilde{\widetilde{S}} = \begin{pmatrix} S_{UU} & S_{UO} & S_{UL} \\ S_{OU} & S_{OO} & S_{OL} \\ S_{LU} & S_{LO} & S_{LL} \end{pmatrix} = \widetilde{\delta V} \cdot \widetilde{\delta V}^{*T} / B, \tag{4.15}$$

where B is the bandwidth over which the voltage fluctuations are considered. The diagonal terms of this matrix are just the voltage noise spectral densities at the various frequencies, *i.e.*, S_{OO} is the voltage spectral density at the intermediate frequency, $S_V(\omega = \omega_0)$. The off-diagonal terms represent correlations in the noise at different frequencies, which are introduced by the nonlinearity of the mixer and its frequency conversion. It is straightforward to calculate the currents due to the voltage fluctuations added to Equation (4.8), $\widetilde{I} = \widetilde{\widetilde{Y}} \cdot \widetilde{\delta V}$. Since we are interested in the noise at the IF output of the mixer, we define the vector $\widetilde{\widetilde{Y}}_0 = (Y_{OU} \quad Y_{OO} \quad Y_{OL})$, and consider the mean square amplitude of the noise currents in the bandwidth B at the IF port,

$$|\widetilde{I}|^2 = \widetilde{\widetilde{Y}}_0 \cdot \widetilde{\widetilde{S}} \cdot \left(\widetilde{\widetilde{Y}}_0^*\right)^T. \tag{4.16}$$

The noise temperature of a mixer is defined as the temperature of a thermal load which, when placed at the RF input of the mixer, exactly doubles the output noise of the device. The total IF noise power is converted to an available RF noise power by dividing by the conversion efficiency, and one obtains for the noise temperature

$$T_N = \frac{\widetilde{\widetilde{Y}}_0 \cdot \widetilde{\widetilde{S}} \cdot \left(\widetilde{\widetilde{Y}}_0^*\right)^T}{4 k_B |Y_{OU}|^2 \Re e(Z_U)}. \tag{4.17}$$

Notice that the mixer noise depends, in principle, upon all the elements of the noise correlation matrix. Also, the mixer temperature is independent of the IF load impedance, Z_o. Any impedance mismatch at the IF port of the mixer affects both signal and noise identically, and thus the signal to noise ratio (*i.e.*, the mixer temperature) is independent of this mismatch. In a real system, however, increases in the IF mismatch lead to a decrease in the coupled conversion efficiency, and will increase the contribution of the following IF amplifier's noise to the overall receiver, thus degrading the performance. In any event, we can see that once the noise and conversion matrices are determined for a mixer, the mixer noise and conversion efficiency can be determined for any combination of IF and RF impedances by constructing the total impedance matrix, performing the matrix inversion to find $\widetilde{\widetilde{Y}}$, and calculating η_C and T_N using Equations (4.14) and (4.17). Since both these equations were calculated assuming a signal in only one of the two sidebands, these quantities are called the single-sideband (SSB) mixer temperature and conversion efficiency.

4.4. Mixer Calculations from the RSJ Model

The methods described in the previous section can be used for the calculation of Josephson mixer performance based on the RSJ model. The procedure for determining the conversion and noise matrices is described by Taur (1980), who calculated mixer performance for the case of vanishing junction capacitance (*i.e.*, $\beta_C = 0$). The RSJ equation with a constant local oscillator current is solved in the time domain and then Fourier analyzed to obtain the complex voltage amplitudes at the various different frequencies. Torrey and Whitmer (1948) present a method in which all of the conversion matrix elements can be determined from the I-V characteristic, the voltage amplitude at the LO frequency, and their derivatives with respect to the bias and LO currents. Taur utilized this method. Alternatively, a small driving current can be numerically injected in addition to the local oscillator, and the voltages at the three ports in response to this stimulus determines three matrix elements. The other elements can be determined by changing the frequency of the small current stimulus. The latter method, which was used in this work, is equivalent to the first method, and has the advantage that the signal strength could be varied to investigate saturation or confirm

the linearity of the mixer. In practice, the different stimuli could be simultaneously introduced at similar but noncommensurate frequencies, allowing a single time series to be used. The matrix symmetries were used, so that only two signals, one at the upper sideband to determine the high-frequency impedances and the downconversion, and one at the intermediate frequency to determine upconversion, were needed. Typical signal currents were about one percent of the critical current, and several time series were analyzed and the impedances averaged in order to give good signal to noise on the matrix determination despite the noise in the simulations. In order to use a low intermediate frequency, a long time series is required for Fourier analysis (typically 10^4 points). This means that the mixer calculations rapidly become computationally intensive. A very long time series is generated, but much of the information is not used because of the required frequency selection of the mixer calculations.

The noise correlation matrix could also be determined from the Fourier analysis of the RSJ time series. The elements of the matrix are just products of the Fourier amplitudes at the appropriate frequencies, in the absence of signal. For example, the diagonal elements are just the power spectral density at the intermediate frequency and upper and lower sideband frequencies. All RSJ simulations were performed using normalized units, and the noise correlation matrix is then in units of normalized voltage spectral density, as is S_v. Similarly, the conversion matrix elements, as determined by the ratios of normalized voltages to normalized currents, are automatically normalized with respect to the normal state resistance, R_N. The equation for the conversion efficiency is dimensionless and requires no adjustment, while the equation for the noise temperature is normalized to the physical temperature of the mixer, and becomes

$$T_N/T = \frac{\tilde{\tilde{Y}}_0 \cdot \tilde{\tilde{S}} \cdot \left(\tilde{\tilde{Y}}_0^*\right)^T}{4\Gamma |Y_{OU}|^2 \Re e(z_U)}, \tag{4.18}$$

where $\tilde{\tilde{Y}}_0$ and $\tilde{\tilde{S}}$ are now in normalized units, z_U is the normalized RF impedance, and Γ is the RSJ noise parameter.

4.5. RSJ Calculations of Conversion and Noise Matrices

In this section, we will discuss some of the behavior of the conversion and noise matrix elements as calculated from the Monte-Carlo simulations of the RSJ model. The work by Taur (1980) discussed similar results only for the case of zero capacitance, and a full explanation of the origin of the observed excess noise and optimization in its presence was not given. Full calculations of mixer noise and conversion gain will be presented in the following section.

The large-signal impedance determined from the RSJ model with the parameters $\beta_C = 0.8$, $\Gamma = 0.015$, $\Omega_{LO} = 0.5$, and $i_{LO} = 0.75$ are shown in Figure 4.5, plotted as a function of the average voltage. This impedance is simply defined as the ratio of the induced LO voltage to the applied LO driving current, and is normalized to the normal-state resistance, R_N. Both the real and imaginary parts are symmetric about the center of the riser. The real part of the impedance is roughly half of R_N, while the imaginary part is somewhat smaller and changes sign near the midpoint. These impedances tell us about the matching and dissipation of the local oscillator in the mixer. First, we can calculate the required LO power for a particular device from the product of the LO voltage and current. In this case the required power, in dimensioned units, is roughly 0.3 times $I_C^2 R_N$, which for a typical device (*i.e.*, $I_C = 10$ microamps and $R_N = 50$ Ohms) would be about one nanowatt.

The I-V curve is that calculated for a constant LO current in the junction. Due to the variation of the LO impedance with voltage, however, different LO currents would be induced in the junction when the LO is supplied from a source with a finite impedance. The change in LO current across the riser will alter the shape of the I-V curve. One can, in principle, assume a drive impedance for the LO, calculate the large signal impedance, and then adjust the LO current used in the simulation until the voltages at the LO frequency are matched. Taur (1980) showed I-V curves for two different drive impedances which were obtained using this method. He found that an inductive driving impedance could cause negative differential resistance across the riser, while a capacitive drive caused a reduction in the slope of the riser. This technique, however, is time-consuming and adds two more parameters (the real and imaginary parts of the driving impedance) to the nonlinear

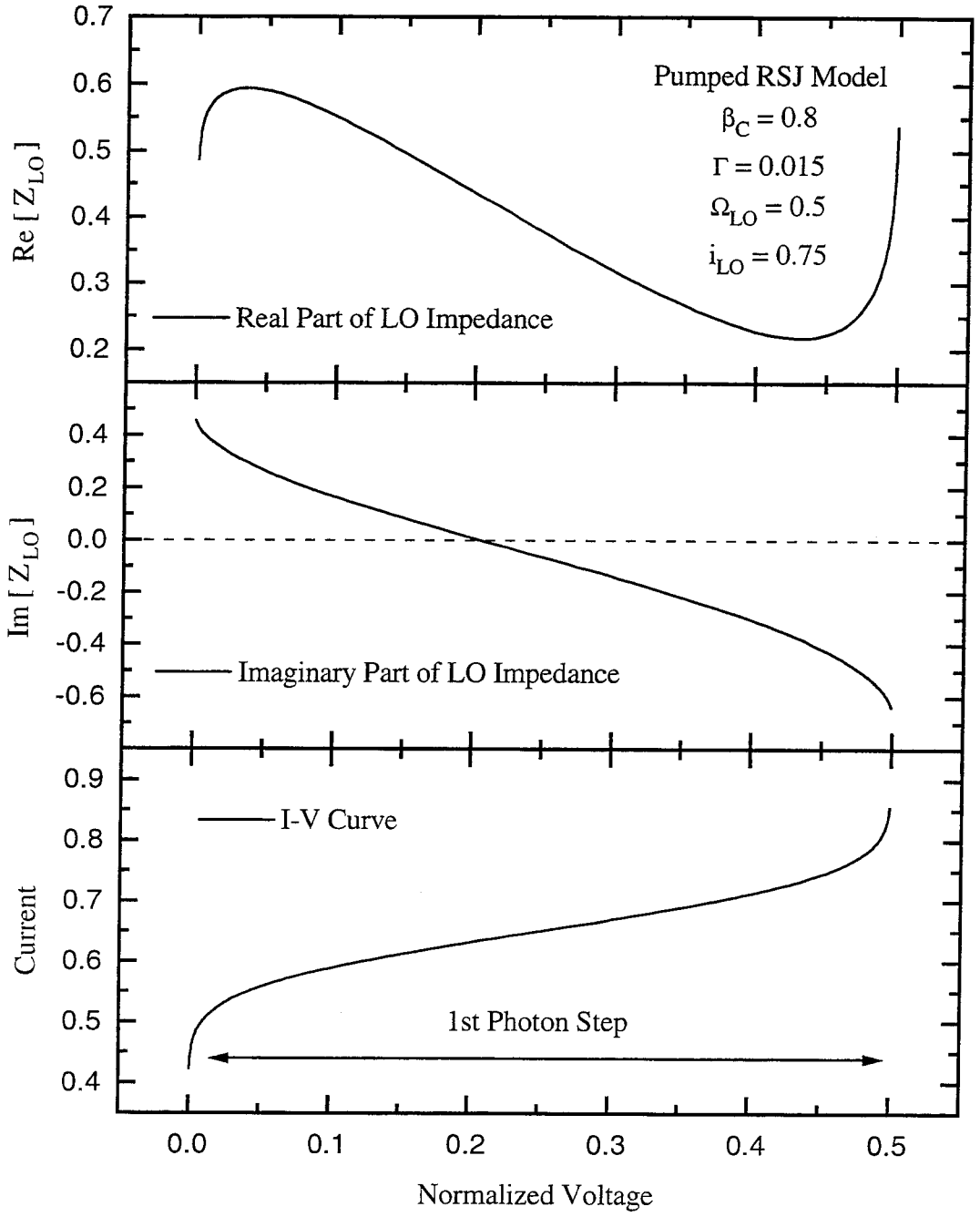

Figure 4.5 The large signal or LO impedance (*i.e.*, the ratio of the voltage at the LO frequency to the drive current) as a function of the bias voltage for the RSJ model. The parameters used were: $\beta_C = 0.8$, $\Gamma = 0.015$, $\Omega_{LO} = 0.5$, and $i_{LO} = 0.75$. Both the real and imaginary parts are shown. The bottom graph shows the I-V curve, and the voltage ranges across the first "riser," *i.e.*, between the zeroth and first Shapiro steps.

part of the calculation. We will only present I-V curves and other quantities here for constant LO current solutions to the RSJ equation. Although these do not necessarily correspond to curves which would be observed for the experimental case of a finite drive impedance and a fixed local oscillator power, all points on the curve do correspond to an attainable combination of LO powers and bias voltages, provided that the biasing circuit is stable for any negative resistances which may occur. Furthermore, the calculated I-V curves should correspond well with the cases of either a large or a mostly real driving impedance.

The more important impedances for mixing, of course, are the small signal impedances in the conversion matrix, $\tilde{\tilde{Z}}$. Several of these matrix elements are displayed in Figure 4.6. Since these are obtained by injecting small (relative to the LO) currents and observing the response of the junction, the noise on these elements is significantly larger than for the large-signal impedance. For the data displayed here, 200 independent determinations of the matrix elements were made, each from time series containing 16,384 points. To obtain the matrices for each of the 160 points on the I-V curve required about ten minutes of CPU time on a CRAY Y-MP. The parallel nature of this machine allows many points on an I-V characteristic to be calculated simultaneously. Alternatively, one may determine the matrix elements from the appropriate derivatives of the large-signal impedance with respect to the LO and DC bias current. To determine these derivatives accurately for small changes in the bias currents would require similarly large amounts of computational power. Unfortunately, a systematic exploration of parameter space or a full optimization of mixer performance is difficult, since there are several parameters for the modelling (*e.g.*, β_C, Γ, Ω_{LO}, i_{LO}, and the bias voltage) which can be changed, and each requires a new solution of the RSJ equation to determine the noise and conversion matrices.

Nonetheless, the mixer impedances as determined are sufficient for calculations of the mixer noise and conversion efficiency, and several general characteristics of the matrices can be seen in the data presented in Figure 4.6. The top graph shows the real part of the IF impedance of the device, Z_{OO}. In this case, a finite IF of about 2% of the LO frequency was used. For these low frequencies, the IF impedance is expected to approach the differential resistance seen in the DC I-V curve. We see

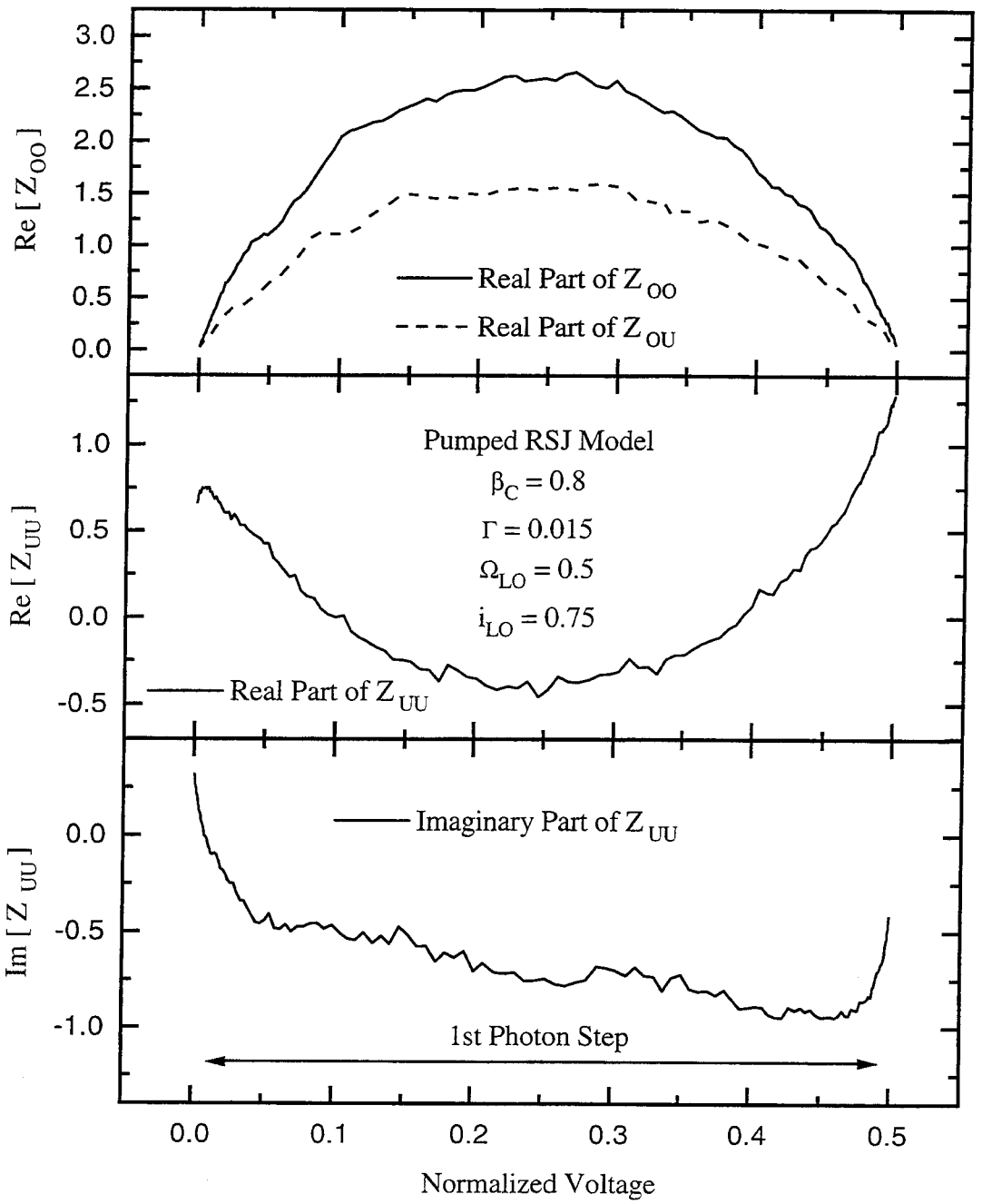

Figure 4.6 Several elements of the conversion, or small-signal impedance matrix, $\tilde{\tilde{Z}}$, are shown as a function of bias voltage. RSJ model parameters were those used in Figure 4.5. Top graph shows the IF impedance, Z_{oo} (full line) and Z_{ou} (dashed line). The bottom two graphs show the real and imaginary parts of the upper sideband impedance, Z_{uu}. All impedances are normalized to R_N.

that Z_{oo} does indeed have a smooth maximum in the center of the riser, attaining a value several times larger than the normal state resistance, R_N, and approaching zero at each of the Shapiro steps. The dashed curve in the same graph shows the real part of the down-conversion term, Z_{ou}. This element also attains a maximum in the midpoint of the riser. Although conversion efficiency depends on the impedances of the external circuit, it is obvious that good mixer performance will require significant off-diagonal elements in the conversion matrix. The behavior of Z_{ou} and Z_{oo} suggests operation of the mixer in the middle of the riser, in agreement with the simplistic analysis of Section 4.2. The last two curves shown in Figure 4.6 display the real and imaginary parts of the upper sideband impedance, Z_{uu}. Notice that the real part of this impedance is negative near the center of the step, which may imply that RF oscillations or reflection gain is possible. It is important, however, to remember that best mixer performance does not necessarily require optimum power matching to this impedance. We will see below that good conversion efficiency can be obtained for real impedances of the RF load comparable to R_N. All of these impedances and their bias dependence are quite similar to those calculated by Taur (1980) for a slightly different LO frequency ($\Omega_{LO} = 0.4$) and no junction capacitance ($\beta_C = 0$).

The bias dependence of some of the elements of the noise correlation matrix, $\tilde{\tilde{S}}$, is shown in Figure 4.7. Both the low-frequency (S_{oo}) and RF (S_{uu}) voltage noise also have maxima in the center of the riser. In addition, we can see that the values attained by the noise are significantly greater than that expected from pure Johnson noise in the absence of the Josephson nonlinearity. In this case, the voltage spectral density of the Johnson noise should have been close to 4Γ, or about 6×10^{-2}. As in the case of the unpumped junction, we see that the voltage noise from the RSJ model is large in regions of high dynamic resistance. The large values of the noise correlation matrix elements are the manifestation of the "excess" noise of Josephson mixers. The excess and its generation will be discussed fully in the following chapter. Also shown in Figure 4.7 is the complex matrix element S_{ou}. As one would expect, the off-diagonal elements of the noise matrix can be significant when there is efficient frequency conversion in the device. The correlations of the noise at the mixer's different ports can sometimes improve the noise performance of the mixer. This is

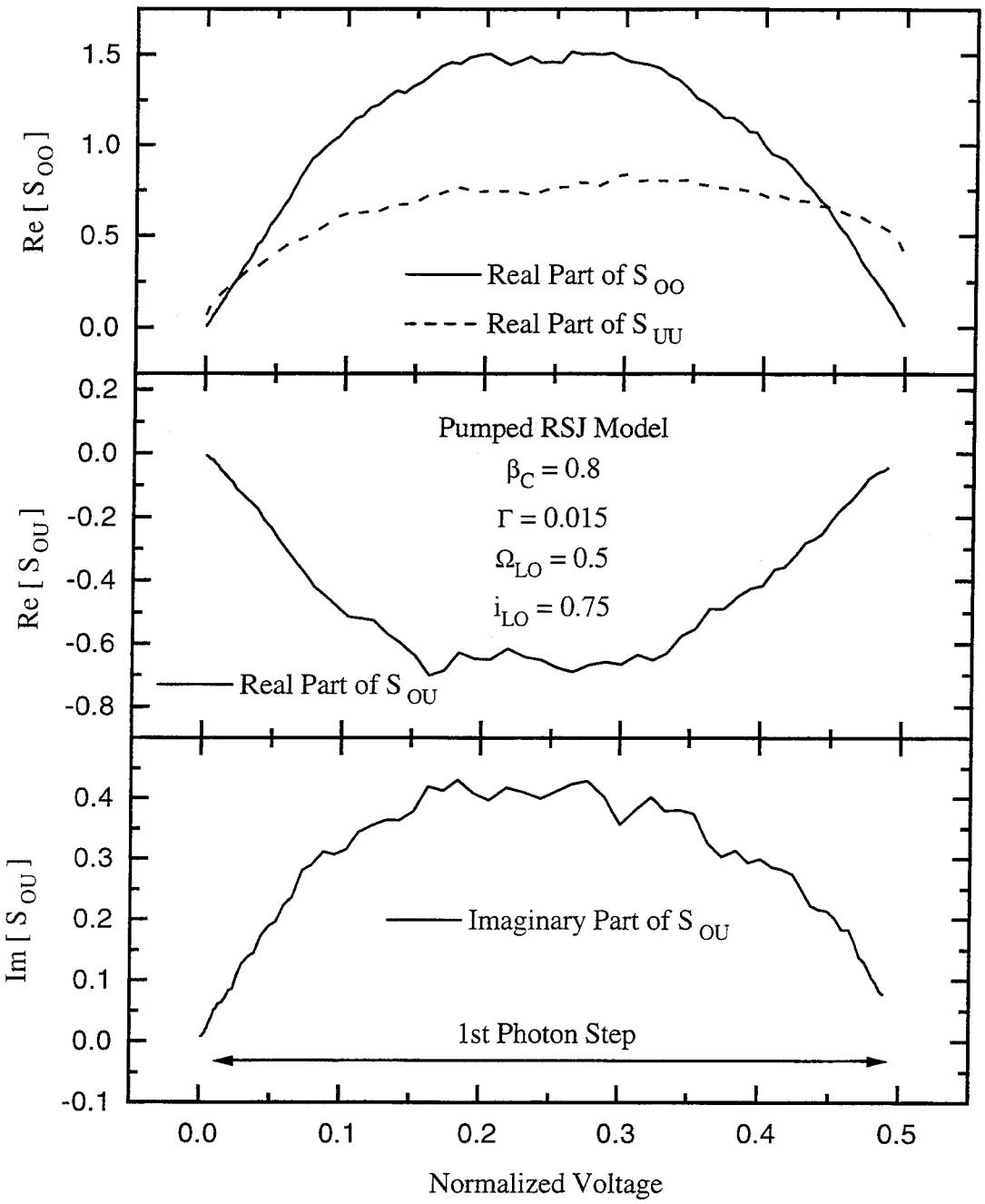

Figure 4.7 Several elements of the noise correlation matrix, $\tilde{\tilde{S}}$, as a function of bias voltage for the same parameters used in Figures 4.5 and 4.6. Top graph shows the voltage noise at the intermediate frequency, S_{oo} (full line), and at the upper sideband frequency, S_{UU} (dashed line). Also shown are the real and imaginary parts of the matrix element S_{oU}. All elements are normalized voltage spectral densities, *i.e.*, so that pure Johnson noise has a density of 4Γ.

the case for SIS mixers, which under the correct conditions have strong correlations which cancel out the effect of the junction's shot noise and lead to quantum-limited performance.

4.6. Mixer Noise and Conversion Calculations

Having calculated the complete noise and conversion matrices from the RSJ simulations, we can then use the methods described in Section 4.3 to obtain the mixer noise temperature and conversion efficiency for any choice of the embedding impedances. As mentioned earlier, the mixer noise is independent of the impedance of the IF load. The external impedances (real and imaginary parts) at the upper and lower sideband frequencies therefore constitute four separate parameters which can be varied in the linear three-port mixer calculations. However, there are two special cases of practical interest. Because of the very small (compared to the local oscillator frequency) intermediate frequency used in most mixers, the impedance of any mounting circuit which is not highly resonant will be nearly identical at the sidebands. This circumstance then leads to very similar conversion of signals from the two sidebands, and the mixer is called a "double-sideband" receiver. Sometimes, however, it is desirable to make the mixer sensitive only to one of the sidebands, in order to reduce the noise when observing a narrow spectral feature which appears in only one of the sidebands. In this case, the unwanted sideband is usually terminated in a reactive impedance, which is very different from the other sideband's impedance. We will refer to the case in which the RF impedances are identical to each other as the double-sideband (DSB) case. Note, however, that all noise and conversion numbers are "single sideband" (SSB), or those that would be observed for a signal appearing in only one sideband.

Contours of mixer noise temperature, normalized to the physical temperature and calculated using the parameters and matrices shown above in Figure 4.5, are shown in Figure 4.8 for the DSB case, as a function of the real and imaginary parts of the RF embedding impedance. Contours were calculated for a bias voltage of about 0.2, just below the midpoint of the photon step. We can see that the noise has a smooth minimum at an impedance which is slightly inductive and comparable or somewhat higher than the normal-state resistance. For sufficiently high resistance Josephson

devices, this impedance could be attained in a variety of coupling structures. The Josephson element is essentially a nonlinear inductance (*e.g.*, Likharev, 1986, p. 9), whose magnitude is $L_J = \hbar/2eI_C$. Thus at a frequency comparable to the critical frequency, ω_C, the magnitude of this impedance is simply $\omega_C L_J \sim R_N$. Thus it is perhaps not too surprising that the best performance is found close to the condition for optimum "match" to the nonlinearity. In SIS mixers, for example, there is a large capacitance which acts as a parasitic, but best performance is found for impedances which just compensate this reactance and give optimal power match into the nonlinear tunnelling resistance. Even for these simulations of the RSJ model with nonzero β_C, the capacitance of the device is relatively small (*i.e.*, the ωRC product is less than one at the LO frequency). Indeed, Taur found nearly identical optimum impedances for the case of zero junction capacitance.

A few comments about interpreting these mixer noise temperatures are necessary. The best noise temperature found for these parameters is about 17 times the physical temperature, which is roughly a factor of two lower than the best found by Taur without capacitance. Because of the RSJ normalized units, the noise temperature is determined relative to the physical temperature. This does not mean that mixer noise can be lowered arbitrarily by reducing the operating temperature of the device. The simulations are valid only for the particular set of RSJ parameters used in the modeling. For example, if one lowers the temperature of a real device, the critical current will be nearly constant with temperature, provided that the device was initially not near its transition temperature. This in turn means that the noise parameter (*i.e.*, $\Gamma = \frac{2e}{\hbar} k_B T/I_C$) in the RSJ model will decrease as the temperature decreases, and the noise temperature may be some different multiple of the new physical temperature. The use of the normalized units complicates interpretation, because we must keep in mind which parameters will be changed by altering one of the junction characteristics or experimental conditions. We will discuss the variation of the mixer noise with temperature and other parameters in the following chapter, after the mechanism for the excess noise has been clarified.

Figure 4.9 shows the corresponding dependence of the conversion efficiency on the RF impedance. For this calculation, an IF load impedance must be specified; here it is fixed to be real and three times the normal-state resistance. This is close to the observed IF impedance of the

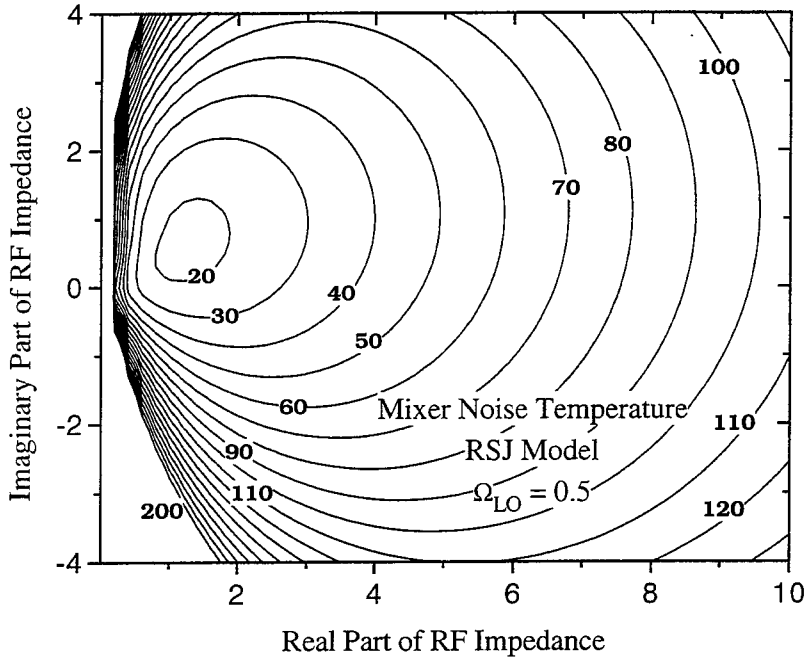

Figure 4.8 Contour plot showing dependence of mixer noise temperature on the RF embedding impedance for the DSB case (*i.e.*, both sidebands equal). RSJ simulation parameters are as for Figure 4.5. Contours are labelled with the single sideband noise temperature normalized to the physical temperature (T_N/T). The bias voltage was taken to be $v \sim 0.2$, just slightly below the midpoint of the photon step.

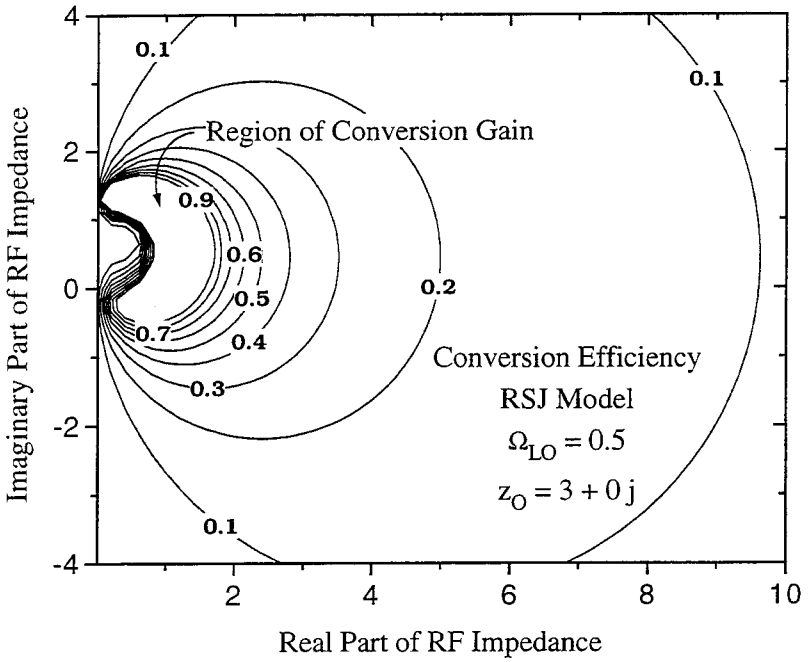

Figure 4.9 Contour plot showing the dependence of the conversion efficiency on the RF embedding impedance, in the DSB case, for the same RSJ simulation as in Figure 4.8. The impedance of the IF load was fixed to be real and three times the normal-state resistance. Note the sizable crescent-shaped region where conversion gain (*i.e.*, efficiency > 1) is possible.

junction, giving a good IF match. In addition, there is a significant region in which the conversion efficiency is greater than unity, and where there is amplification in addition to frequency conversion. For classical mixers, whose response is instantaneous, conversion gain is forbidden and the maximum efficiency can be shown to be -3 dB (50%) (*e.g.*, Torrey and Whitmer, 1948, or Tucker and Feldman, 1985). SIS mixers have a sufficiently strong nonlinearity to provide gain if the width of the current rise at the gap voltage (V_{Gap}) is narrow compared to the photon step width ($h\nu/e$), and unity conversion efficiency or gain has been observed frequently (McGrath *et al.*, 1981). Interestingly, it is often seen experimentally (Kooi *et al.*, 1994) that best receiver performance is obtained just outside of regions of conversion gain. Large gain is often associated with negative output impedance and reflection gain at the IF, which can cause undesirable oscillations. The IF output is also prone to saturation when there is large conversion gain, which will also degrade performance.

The conversion efficiency and single-sideband (SSB) mixer noise temperature as a function of bias voltage across the first photon step are plotted in Figure 4.10. The RF and IF impedance have been held fixed near their optimum values. Note that there is a broad range of voltage near the step midpoint in which there is good noise performance, and that the conversion efficiency is also good in this region. Although this curve does not strictly correspond to an I-V curve which would be observed (*cf.* the discussion above regarding the effects of LO source impedance) when the LO was supplied from a source with the same finite RF impedance, it indicates that the mixer performance should not be overly sensitive to bias. Although an estimate of the error in the model predictions is difficult to obtain due to the complicated functional form (*cf.* Equation (4.18)) of the dependence on the matrix elements, the scatter in nearby points on this curve gives a feeling for the noise level in the calculation.

The RSJ parameters used above correspond to conditions which can be achieved using the resistively-shunted Nb and NbN tunnel junctions at 100 GHz. For example, a junction with a resistance of 40 Ohms, a critical current of 12 microamps, and a nonhysteretic I-V curve would have the appropriate values at 115 GHz when operated at 4.2 Kelvin. In this case, the corresponding double-sideband (DSB) mixer noise temperature would be 35 K in dimensioned units. This would

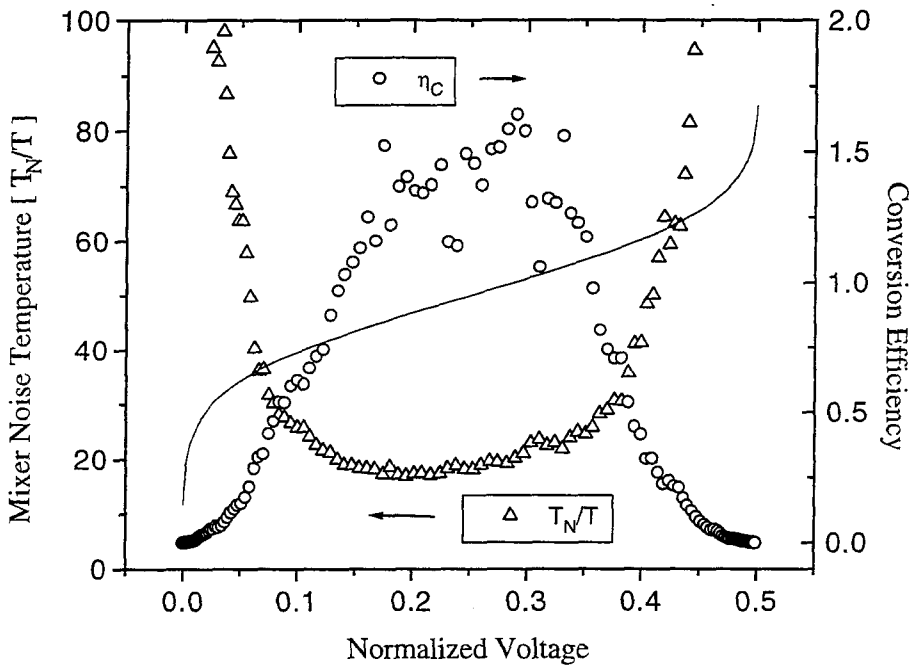

Figure 4.10 Bias voltage dependence of mixer noise temperature and conversion efficiency for the same RSJ simulations as those shown above. Here, the RF impedance is fixed near its optimum value at $1.4 + 0.6j$, normalized to R_N, for the DSB case. Conversion efficiency is calculated assuming an IF impedance of $3.0 + 0j$. The full line is the I-V curve, triangles are the SSB mixer noise temperature, normalized to the physical temperature, and the circles are the coupled conversion efficiency, which is dimensionless.

require a real RF impedance of 40 Ohms, which should be achievable using a waveguide mixer mount or a quasioptical antenna coupled structure. If forced to operate outside the region of conversion gain, the noise would only be about 5 Kelvin higher for an RF impedance of 80 Ohms, and the conversion efficiency would be about 50%. The contribution of the IF amplifier to overall receiver performance could be as low as 10 Kelvin if HEMT amplifiers were used. This noise temperature would not be competitive with an optimized SIS receiver, which could approach the quantum limit of only 2.5 Kelvin, not including front-end optical losses. If the $I_C R_N$ product could be increased while holding all other RSJ parameters fixed (*e.g.*, by increasing the resistance of the device, but holding the critical current fixed), the LO frequency can be increased proportionally and the RSJ predictions of mixer performance would be unchanged.

If one were to increase the local oscillator frequency without changing the $I_C R_N$ product, the

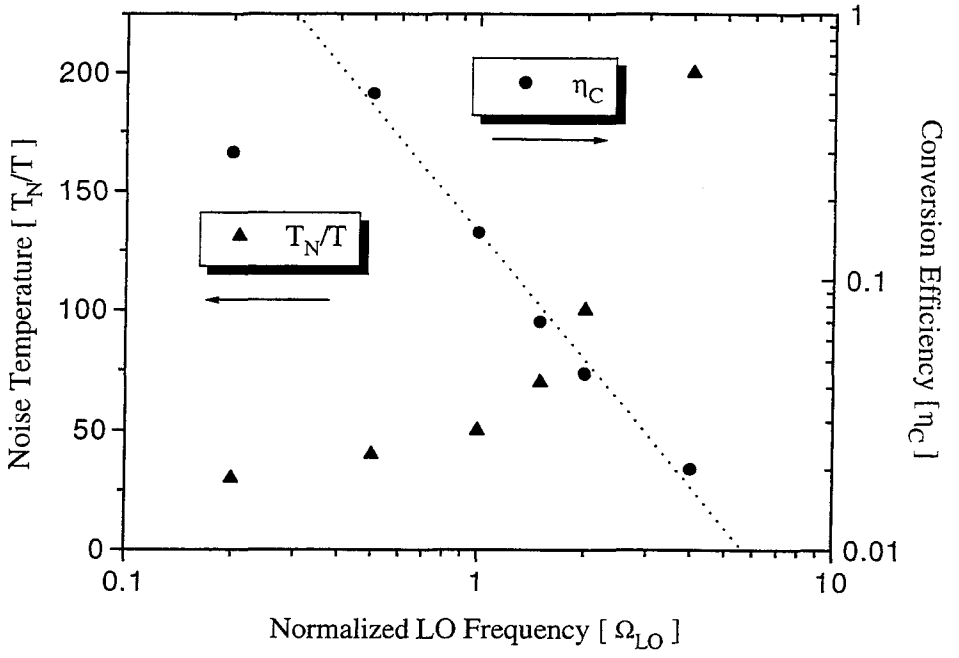

Figure 4.11 The variation of mixer noise temperature (normalized to the physical temperature) and conversion efficiency with the normalized LO frequency, Ω_{LO}. RSJ parameters are fixed with $\beta_C = 0$ and $\Gamma = 0.015$, but the bias voltage, LO power, and embedding impedance have been individually optimized for each case. The line shows a fitted power-law dependence of the conversion efficiency, with an power-law index of -1.5 (*i.e.*, $\eta_C \sim \Omega_{LO}^{-1.5}$.)

normalized frequency would obviously increase. In Section 4.2, we predicted that the mixer performance would rapidly decrease as the normalized frequency becomes greater than one. Figure 4.11 shows the dependence of the optimum mixer temperature and the coupled conversion efficiency on the normalized LO frequency for the RSJ model with $\beta_C = 0$ and $\Gamma = 0.015$. In each case, the bias voltage, local oscillator power, and RF embedding impedance have been optimized for best mixer noise temperature. The optimum RF impedance does not vary strongly, decreasing to about one half of R_N, while the inductive part increases to be about equal to R_N. At the very large frequencies, the dynamic resistance decreases in the middle of the riser (*cf.* Figure 4.1d). The best mixing then moves towards the low end of the riser, where the dynamic resistance and the I-V curve variation with LO power is greatest. The LO current required to provide the same relative suppression of the critical current increases with frequency. We can see from the figure that the noise temperature

degrades rapidly as the frequency increases. There is also a corresponding strong drop in the conversion efficiency. The very simplistic treatment in Section 4.2 predicted that the conversion would degrade roughly as the square of the frequency; the data presented here suggest a power law decrease with an exponent of about -1.5. For higher frequencies, unfortunately, it becomes very difficult to calculate the conversion accurately in the presence of the noise. In any event, it is clear that one needs to restrict the operation of the Josephson mixer to a frequency comparable to or slightly less than the critical frequency, ω_C (*i.e.*, to normalized frequencies less than one).

We have seen that the mixer noise temperature and conversion efficiency can be calculated directly from the RSJ equation which governs the dynamics of a Josephson junction when illuminated with a local oscillator. The "excess" noise of Josephson mixers can be seen under a wide range of parameters, both as a relatively large value for the voltage noise at low frequencies, and in the mixer noise. Mixer temperatures are always found to be some fairly large multiple of the physical temperature of the device, despite the fact that the only noise included in the simulations is Johnson noise with a noise temperature equal to the physical temperature. Optimal mixer performance is found over a broad range of bias voltage near the midpoint of the first photon step, and for RF impedances which are close to the normal-state resistance, and are real or slightly inductive. The addition of a small amount of capacitance seems to lower the noise by about a factor of two, provided that the device remains nonhysteretic. Mixer temperatures (DSB) of five to ten times the physical temperature are achievable for optimized devices at a frequency of about half the critical frequency (ω_C). If devices with large (*i.e.*, several millivolts) $I_C R_N$ products, such as high-T_C based junctions, could be used, these predictions indicate that Josephson mixers could be competitive with other mixer technologies in the submillimeter waveband. We see that under the correct circumstances, the "excess" noise need not prevent interesting sensitivity levels. The origin of the undesired excess noise and optimization in its presence will be discussed in the next chapter.

Chapter 5

Excess Noise in Josephson Mixers

Here be dragons...

– Enrico Fermi, *labelling the nucleus in a lecture, c. 1930*

The question of the origin and severity of the "excess" noise in Josephson-effect mixers is very important for evaluating their potential as high-sensitivity, high-frequency detectors. The result that the mixer noise temperature is many times higher than the physical temperature has been seen both in experiment and in theoretical simulations. The precise origin of this noise, however, has been somewhat less clear. As a result, it has been difficult to predict what the performance levels can be obtained, and to design and properly optimize actual Josephson receivers. In this chapter, we will expand on the dynamics of the pumped RSJ model which were presented in the previous chapter. We will show that the excess noise arises in a similar manner to the excess noise seen in the unpumped RSJ model in Chapter 3. Because the mixer must be biased at a non-zero voltage in order to access the part of the I-V curve where mixing occurs, AC Josephson oscillations result due to this bias voltage. These oscillations have a linewidth which can be large due to the action of any intrinsic noise in the device. The large linewidth of the Josephson oscillations means that the power in these oscillations can then appear at the important frequencies for a mixer, *i.e.*, at the IF output and at the RF sidebands where the signal originates. We will discuss the implications of this understanding for

the optimization of the mixer's noise performance, and also the possibility of operating the junction in a mode in which the excess can be reduced or eliminated.

5.1. History of Excess Noise in Josephson Mixers

Systematic studies of the expected performance of Josephson mixers, based on the RSJ model, have been previously carried out, all of which noted the presence of the excess noise. Claassen and Richards (1978a), performed simulations using an analog computer, and presented a limit of 40 times the physical temperature for the mixer noise of a weakly-coupled junction under a wide range of conditions. However, they noted difficulty in modeling the case of a strongly coupled junction (*i.e.*, for the case in which the RF impedance is comparable to the normal-state resistance). They ascribed the large noise to a combination of noise conversion from harmonics of the local oscillator and noise-induced switching between stable states of the junction (*i.e.*, between locations on a hysteretic I-V curve). In the digital simulations of Taur (1980), discussed in the previous chapter, optimum mixer noise temperatures as low as 20 times the physical temperature (SSB) were predicted for small normalized frequencies ($\Omega \sim 0.2 - 0.4$). Taur is not very precise regarding the origin of the excess noise, besides noting that the large noise is only observed between the vertical Shapiro steps, where the Josephson oscillations are not locked to the LO. He also alludes to an analytic model for the excess, referring to a paper in preparation which was never published. Finally, Zavaleyev and Likharev (1981) found a similar limit of 5 times the physical temperature (DSB; corresponding to 10 in SSB units) based on numerical simulations for the case of a real RF impedance of order R_N. In this work, the limits to noise performance were thought to arise from downconversion of noise from the harmonics of LO and the Josephson oscillation frequency (which is distinct). This last explanation has become the prevailing view in the literature (Likharev, 1986, p. 424). The excess is ascribed to downconversion of Johnson noise from the several ports, $\omega = \omega_0 + m\omega_J + n\omega_{LO}$, while signal is only converted from the two sidebands of the LO.

There is some confusion associated with ascribing the excess noise to chaotic or near-chaotic behavior. An increase in noise associated with chaos has been observed in Josephson parametric

amplifiers (*cf.* Pedersen, 1980) under some conditions. These devices are often made using unshunted tunnel junctions and the capacitance is very high (*i.e.*, $\beta_C \gg 1$). It has been shown that these types of devices are capable of exhibiting true chaotic behavior (Pedersen and Davidson, 1981). This chaotic noise-rise, however, is a completely distinct phenomenon from the excess noise observed in Josephson mixers. The excess noise, for example, is seen in simulations of the RSJ model without any capacitance, for which chaotic behavior is not possible in a range of DC and RF bias (see, *e.g.*, analytic proofs by Cicogna, 1987 and 1988, or simulations by Kautz and Monaco, 1985). However, chaos might explain some experimental observations of large noise temperatures with point contacts, as some of these devices showed hysteresis or I-V curves which were not ideally like the RSJ model.

5.2. The True Mechanism of Excess Noise

To aid in the understanding of the excess noise, let us first recall the expected Josephson dynamics under typical conditions for mixer operation. In Chapter 4, we saw that best operation was expected at a nonzero bias voltage, somewhere on the first photon step or "riser," between the zeroth and first Shapiro current steps. At the first Shapiro step, the Josephson oscillations are phase-locked (and at the same frequency) to the LO. On the riser, therefore, the junction should produce a Josephson oscillation with a frequency somewhere between DC and the applied LO frequency. Of course there is also a strong oscillation at the LO frequency and possibly several of its harmonics. Likharev (1986) ascribes the excess noise to downconversion from the large number of sidebands of these two (*i.e.*, the Josephson and the local oscillator) frequencies, their harmonics, and their other possible combinations.

Figure 5.1 shows the voltage spectral density as a function of normalized frequency, obtained from an RSJ simulation under typical mixing conditions. A local oscillator at a frequency of a half ($\Omega_{LO} = 0.5$) has been applied, and the device biased such that the average voltage is near the midpoint of the riser, or $v \sim 0.25$. A moderate value for the Johnson noise fluctuations ($\Gamma = 0.01$) and zero capacitance ($\beta_C = 0$) have been used. We can see that the induced LO voltage and its harmonics (several harmonics appear at higher frequencies, not shown here) are clearly visible in

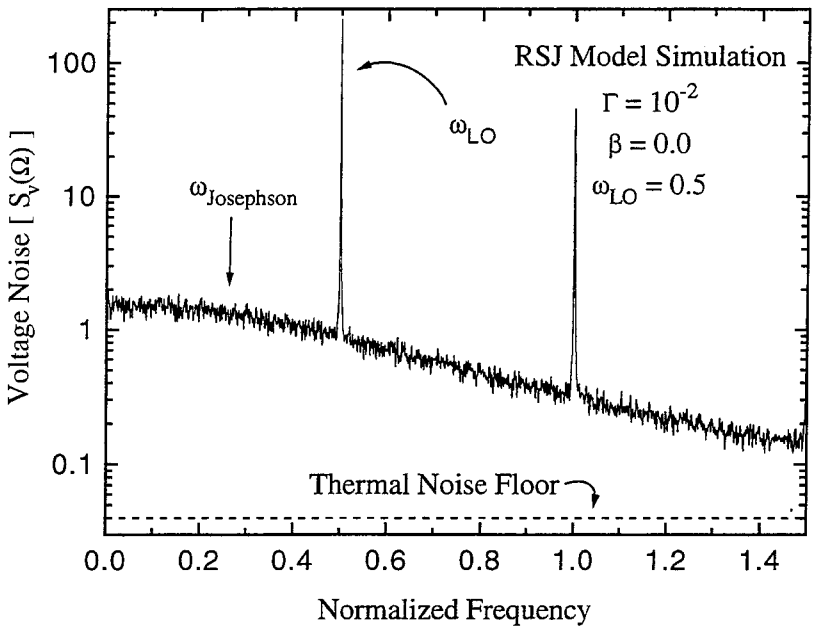

Figure 5.1 Semilog plot of voltage spectral density as a function of normalized frequency for RSJ model with $\beta_C = 0$, $\Gamma = 0.01$, and a local oscillator with frequency $\Omega_{LO} = 0.5$ applied. The mean voltage was 0.25, in the middle of the first photon step, near the position for best mixing response. The Josephson oscillations have become completely incoherent, with a linewidth greater than their center frequency. Thus there is no peak at the frequency expected, but the large excess noise floor resulting from these incoherent oscillations can be seen.

the spectrum. However, the expected Josephson oscillations, centered at a frequency of 0.25, are not evident. Instead, a large, broad-band noise is seen. Also shown (dashed line) is a simplistic assumption of where the thermal noise floor should be (*i.e.*, the thermal noise should be roughly $S_v \sim 4\Gamma \sim 0.04$). The excess noise is more than an order of magnitude larger than the expected thermal noise floor. The only possible explanation is that the Josephson oscillations have acquired a large enough linewidth so that they appear completely incoherent, that is to say, their linewidth is comparable to their center frequency. We saw earlier, in our discussion of the unpumped RSJ model (*cf.* Figure 3.3), that broad spectral features could result from the AC Josephson oscillations. It is these broad oscillations which have given rise to the excess. Clearly, Likharev's picture of mixing from sidebands of this Josephson oscillation or its harmonics is somewhat misleading.

In retrospect, we can see that a large Josephson linewidth is not unexpected in this situation.

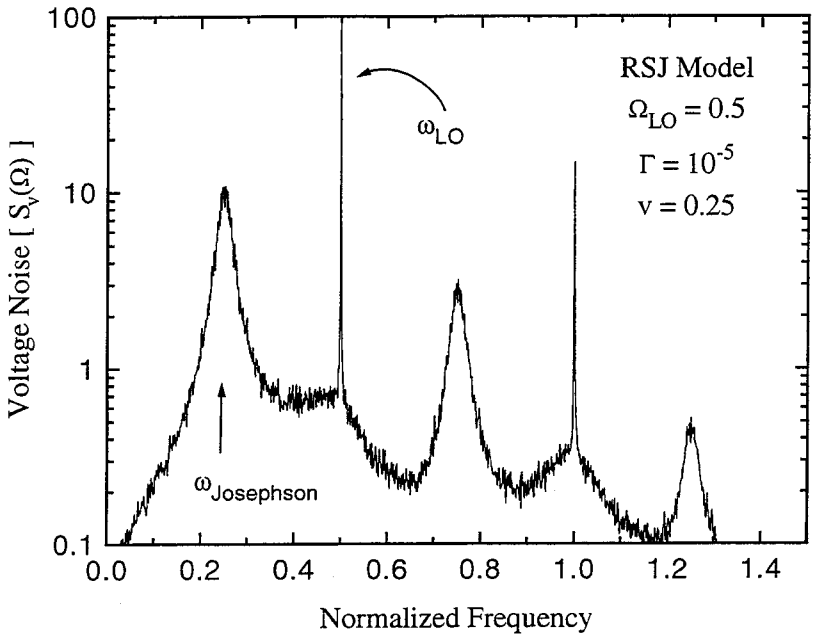

Figure 5.2 Semilog plot of voltage spectral density as a function of normalized frequency for the same RSJ parameters as in Figure 5.1, but with the noise parameter, Γ, reduced to 10^{-5}. In this case, the Josephson oscillation linewidth has decreased to the point where it is less than the center frequency, and the peak at a voltage corresponding to the average voltage of ~ 0.25 can be clearly seen.

In Chapter 3, we saw that the linewidth (in normalized units) should be just one-fourth of the low-frequency voltage noise spectral density. The LS model could be used to predict the low-frequency noise for the case of the unpumped junction, but the presence of the LO and mixing complicates predictions in this case. A lower limit for this noise, however, must be given by the dynamic resistance squared times the input current noise spectral density. For relatively low normalized LO frequencies, the dynamic resistance on the risers can be several times larger than the normal-state resistance. In the particular case shown in Figure 5.1, the dynamic resistance is roughly three times R_N, so we expect a Josephson linewidth greater than $4\Gamma r_d^2$, or about 0.4, which is greater than the oscillation frequency of 0.25. So we see that the large dynamic resistance at the mixing operating point can lead to very incoherent Josephson oscillations which appear as a broad noise floor, whose magnitude can be much greater than the thermal noise. If we reduce the value of the thermal fluctuations (*i.e.*, as Γ decreases), the linewidth will eventually be reduced, and a clear Josephson peak is visible in

the voltage spectrum, as seen in Figure 5.2. Nonetheless, one still finds excess noise in this case, as the wings of this Josephson oscillation contribute to the fluctuations both at low frequencies and at the sidebands near the LO frequency.

5.3. Dependence of the Excess Noise on the Temperature and the Noise Parameter

As we saw in Chapter 3, the dependence of the excess noise on the temperature can be counter-intuitive, and is confused somewhat by the fact that noise temperatures calculated from RSJ simulations are naturally in units normalized to the physical temperature. In this section we will present the variation of some of the mixer noise elements with the RSJ fluctuation parameter, Γ, and discuss the implications for the variation of mixer performance with the actual operating temperature.

Taur (1980), in his discussion of the excess noise, presented a plot (*cf.* his Figure 5) showing the variation of the noise correlation matrix elements, S_{oo} and S_{vv}, with the noise parameter, Γ. A similar plot from our RSJ simulations is presented in Figure 5.3. For very large values of Γ, where the nonlinearity is not important in comparison with the Johnson noise, the elements vary linearly with Γ, with the expected proportionality (S_v equals 4Γ for pure Johnson noise, see dashed line in Figure 5.3). For values of Γ in the range of 0.1 to 10^{-3}, however, the noise matrix elements are nearly independent of Γ. In this range, the voltage fluctuation spectrum is similar to that shown in Figure 5.1, *i.e.*, the Josephson oscillations are very broad and incoherent. Under these conditions, the noise (both at low frequencies and at the RF sidebands) is dominated by the Josephson fluctuations or excess noise. The total power in these oscillations does not depend on the thermal fluctuations, thus leading to the plateau in the values of S_{oo} and S_{vv}. At much smaller values (*i.e.*, $\Gamma < 10^{-3}$) of the fluctuation parameter, the spectrum becomes similar to that shown in Figure 5.2. In this regime, the noise has a slight variation with the Γ parameter, since the linewidth changes, thereby altering the amount of noise due the wings of the Josephson oscillations. The best fit power-law for this variation is shown as the dash-dotted line, with scaling of approximately $S_{oo} \sim \Gamma^{1/4}$. Taur did not investigate these small fluctuation ranges, and incorrectly postulated that the noise matrix

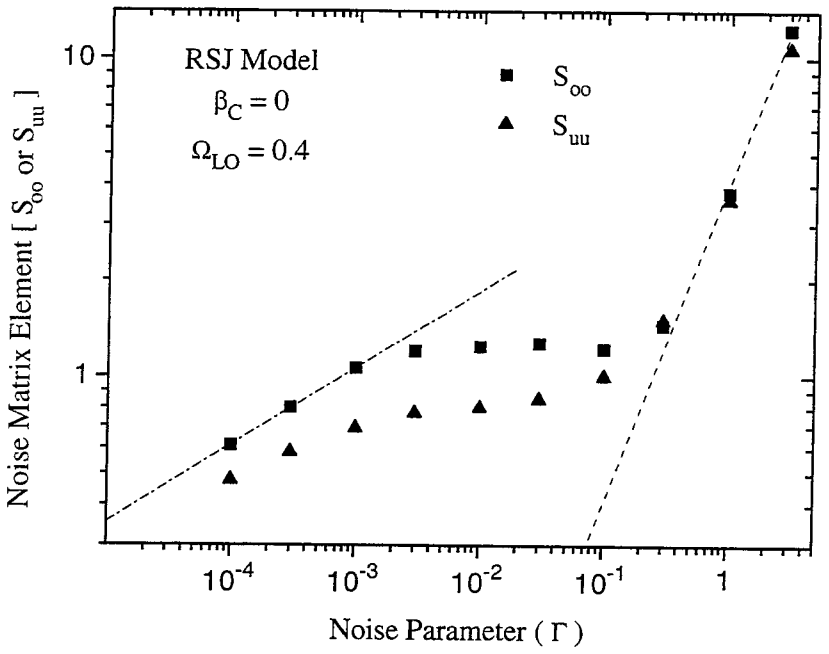

Figure 5.3 This figure shows the variation of the noise correlation matrix elements, S_{oo} (squares) and S_{uu} (triangles), with the RSJ fluctuation parameter, Γ. The simulations are performed for the pumped RSJ model with no capacitance ($\beta_C = 0$) and for a normalized LO frequency of about a half ($\Omega_{LO} = 0.4$). The noise is taken at a voltage near the middle of the riser, where it attains its maximum value, which is also where a mixer would be operated. The dashed line shows the expected high-temperature limit of $S \sim 4\Gamma$. For smaller values of the Γ parameter, the noise is observed to be nearly independent of the input fluctuations, due to the increasingly important effects of the "excess" noise.

elements would be independent of Γ to arbitrarily small values.

The question then arises of why the Josephson linewidth is not dependent on the Γ parameter in the intermediate range of values. We recall that the low frequency voltage noise is multiplied by the square of the dynamic resistance (*i.e.*, the slope of the I-V curve) at the operating point. A lower limit for the linewidth is given by this low frequency noise, $\delta \sim 4\Gamma r_d^2$. As the Γ parameter is reduced, the dynamic resistance increases, due to the reduced amount of noise rounding of the I-V curve. This increase in the dynamic resistance conspires to keep the linewidth large, even as the level of the input Johnson noise fluctuations decrease. The variation of the maximum dynamic resistance on the photon step, for the same parameters as in Figure 5.3, is shown in Figure 5.4. This increase in the maximum dynamic resistance is analogous to the variation seen in Chapter 3 regarding the

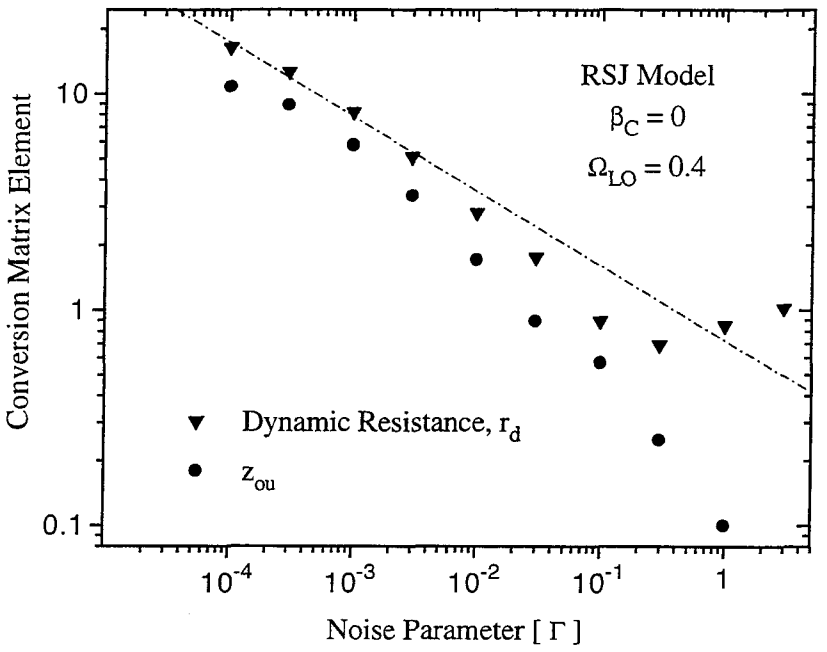

Figure 5.4 This figure shows the variation of the conversion matrix elements, Z_{oo} (or the dynamic resistance, triangles) and Z_{ou} (the down-conversion element, circles), with the RSJ fluctuation parameter, Γ. The simulations are performed for the same RSJ model parameters as in Figure 5.3. The maximum values of the impedances are taken, which also occur near the center of the riser. The dash-dotted line shows the best-fit power law for the variation of the dynamic resistance with fluctuation strength, Γ, at small values, leading to a scaling of $r_d \sim \Gamma^{-1/3}$.

unpumped RSJ model. In fact, for very small fluctuation values, the variation with Γ has the same dependence (*cf.* Figure 3.7) of $r_d \sim \Gamma^{-1/3}$. At very large fluctuations, the nonlinearity in the I-V curve is destroyed, and the dynamic resistance approaches the normal-state resistance (*i.e.*, $r_d \rightarrow 1$, as seen in Figure 5.4). Recalling the qualitative discussion of mixing given in Section 4.2 that the downconversion is proportional to the dynamic resistance at the mixer operating point, it is not surprising that the down-conversion matrix element increases along with the differential resistance as Γ decreases. For large fluctuation values, the down-conversion should go to zero, consistent with that depicted, but the signal-to-noise on its determination also rapidly decreases. The depicted behavior of the impedances as a function of Γ is very similar to that observed by Taur, except that he proposed a $\Gamma^{-1/2}$ scaling for r_d.

5.4. Optimization of Mixers in the Presence of Excess Noise

Now that the origin of the excess and its variation with the noise parameter have been clarified, we can address the variation of mixer performance with the physical temperature. A naive view, based on the fact that RSJ mixer temperatures are normalized to the physical temperature, would argue for reducing the operating temperature in order to obtain a proportional reduction in mixer temperature. Assuming, however, that all other parameters such as critical current and operating frequency are held constant, this reduction of temperature would also cause a reduction in the fluctuation parameter, Γ. We can see (*cf.* Figure 5.3) that for intermediate values of Γ, this reduction of temperature (and Γ) would not lead to any reduction in the output noise, S_{oo}. The sharpening of the nonlinearity due to the reduction in Γ could, however, lead to better conversion and a reduction of mixer noise temperature. However, we saw earlier in Chapter 4 that significant conversion gain was possible even for fairly large values of the fluctuations ($\Gamma = 0.01$). If we assume that the mixer will be operated out of this region of gain, near unity efficiency, then the mixer noise temperature would not be expected to improve as the temperature was lowered. The normalized mixer temperature will in fact rise as the operating temperature is reduced, while the actual mixer noise is nearly constant. This is simply because the noise is dominated by the temperature-independent excess, rather than by the underlying Johnson noise.

If we consider the optimization of the mixer at a fixed physical temperature, we arrive at an even more surprising result. If all other parameters can be held fixed, the normalized temperature will decrease with increasing values of the fluctuation parameter, Γ. Thus if we could reduce the critical current, while holding the $I_C R_N$ product and thus the normalized frequency constant, the actual noise temperature will improve. As the Γ parameter becomes large (~ 0.1), however, the conversion efficiency will eventually degrade, and mixer noise increases again. This is seemingly contradictory in that we are proposing to reduce the nonlinearity by increasing Γ and the rounding of the steps in the I-V curve. Since good conversion is possible, however, this prediction makes sense when we consider what controls the strength of the excess noise. This noise is proportional to the

total power in the Josephson oscillations, and so decreases with decreasing critical current.

Another interesting question is how the excess noise might scale with an increase in the operating frequency. Based on the RSJ model, we would expect that operating frequency can be arbitrarily increased, as long as the $I_C R_N$ product is similarly increased to keep the normalized frequency constant. In this case, the RSJ parameters would all be identical, leading to a prediction of an identical noise temperature, independent of frequency. However, the most likely way to increase the $I_C R_N$ product would be to increase I_C, since R_N must stay approximately constant to allow for matching to antennas and IF systems. In this case, the Γ parameter will be decreasing as the $I_C R_N$ product increases. As mentioned above, the increase in the critical current will increase the output noise and the noise temperature. For example, one could double the critical current and simultaneously double the operating temperature to maintain the same value for the gamma parameter. Then the RSJ model (for which all parameters were unchanged) will predict a twofold increase in mixer noise, since the same normalized temperature would be multiplied by a larger physical temperature. If one operated at the same physical temperature, the increase in noise might be slightly less than linear with frequency (and critical current). Of course, as the operating frequency increases, the quantum noise, which is not included in the RSJ modelling, will increase. However, the noise is usually dominated by the excess, and the quantum noise would constitute only a small addition.

Based on the understanding of the excess noise mechanism, we can perform a simple order-of-magnitude estimate of its severity without the use of the RSJ model. Given the situation seen in Figure 5.1, we may estimate the voltage spectral density by dividing the total Josephson oscillation power by the bandwidth over which they occur. The voltage amplitude of the Josephson oscillations is of order $I_C R_N$. When the oscillations are completely broadened, they extend over a range from DC to about ω_C. Thus we expect a normalized voltage spectral density of about one, in agreement with that seen on the "plateau" in Figure 5.3. The output temperature (not the mixer temperature) should be roughly $T_N/T = \frac{S_v}{4k_B T R_N}$, which becomes $T_N/T \sim 1/\Gamma$. This offers some support for the claim that the Γ parameter should be increased until conversion efficiency degrades in order to

optimize the mixer noise temperature. All of the observations above basically spring from the fact that Josephson mixers are predicted to have good conversion, but relatively high output noise. Thus an optimization is best carried out by reducing the level of the excess noise.

5.5. Excess Noise and the "Self-Pumped" Mixer

There is a mode of operation for Josephson mixers which has not been discussed so far. The internal high-frequency oscillations produced when the junction is biased can in principle be used as the local oscillator for mixing. The junction is simply DC biased at the appropriate voltage so that its oscillation frequency is offset from the signal by the desired intermediate frequency. Such a mixer would have the obvious practical advantage of an integrated, voltage-controlled LO, eliminating the need for expensive and complicated sources. If the Josephson oscillation linewidth could be made sufficiently narrow, then the mixer would still have good spectral resolution. In addition, since the Josephson oscillations would be at the LO frequency, this mixer would not suffer from excess noise. The I-V curve does not display photon-assisted tunnelling steps, and there is no region of large dynamic resistance to broaden the oscillations. By moving the Josephson oscillations to the LO frequency and narrowing them, the excess can be removed.

Although a Josephson mixer which uses this mode has never been constructed, a theoretical analysis of the mixing has been performed by Devyatov *et al.* (1986). They derived mixer noise temperatures and conversion efficiencies based on an analytical treatment of the conversion matrix, which is possible because there is no externally-applied large signal (*i.e.*, no LO). They showed that quantum-limited performance might be possible under optimum conditions and for frequencies less than the critical frequency, ω_C. However, their analysis was for the case of zero capacitance and no reactances whatsoever at the signal frequencies. Our attempts to reproduce this calculation have shown a strong suppression of all conversion when a small reactance (which is unavoidable in practice) is included at the RF ports. However, the results of Koch *et al.* (1980 and 1981, *cf.* Section 3.2) used this mixing mode to measure the zero-point contribution to the Johnson noise of a resistor, and suggest that the conversion efficiency is non-vanishing and that the noise can approach

the quantum limit.

Methods such as those used for Josephson oscillators, including arraying of junctions or low-frequency shunting to provide a good constant-voltage biasing of the junction, could be used to reduce the linewidth of the oscillations. Without a great deal of care, however, the oscillations would be unacceptably broad, given the standard 40 MHz per Ohm of junction resistance per degree from Johnson noise. While the conclusions regarding excess noise suggest that the self-pumped mixer might have a great advantage in sensitivity, the state of the theoretical analysis indicates that further study would be desirable before undertaking experiments on these devices.

5.6. Summary

In this chapter, we have attempted to clarify the mechanism through which the excess noise is generated in Josephson mixers. It is seen not to be caused by chaos or harmonic conversion, but instead by the broadened internal Josephson oscillations. When the mixer is operating, these oscillations are centered at a frequency between the IF and the LO, but they can be very incoherent, contributing large fluctuations at both the IF and RF ports of the mixer. As such, they are an unavoidable consequence of the particular nonlinearity involved in Josephson mixing. The nonlinearity acts to take power from the DC biasing circuit and produce high-frequency fluctuations which decrease the mixer's sensitivity. The result is mixer and output noise temperatures which can be large factors above the underlying physical temperature. This behavior is possible because the device is not being operated under equilibrium conditions (*i.e.*, it is biased). This phenomenon is not too unlike, for example, the shot noise produced by a tunnel junction at non-zero bias. Understanding of the noise mechanism allows some predictions regarding the optimization procedures and the expected scaling of mixer performance. It also suggests that the heretofore untried self-pumped mixing mode may achieve far better noise performance.

Chapter 6

Fabrication of Resistively-Shunted Tunnel Junctions

God is in the details.

– Shaker proverb

God is subtle, but he is not malicious.

– Albert Einstein

The devil is in the details.

– German proverb

In this chapter, we will present the method used to fabricate the resistively-shunted junctions which were used for the noise and mixer measurements. First, we examine the requirements for Josephson mixer devices and the relative merits of the various types of devices. A discussion of the use of tunnel junctions and the advantages and disadvantages of resistively-shunted junctions follows. Finally, an overview of the fabrication process is given and the design and implementation of the shunt resistors is presented. A brief summary of the device characteristics resulting from this process is given, and measurements of the I-V curves and the noise of these devices is discussed at length in Chapter 7.

6.1. Device Requirements for Josephson Mixers

To this point, we have not discussed the specific realization of an actual Josephson junction

and the practical aspects of their use as detectors. The Josephson effect is present in many different varieties of superconducting devices, and all of these can in principle be utilized as mixers. However, a practical device should be stable and should be able to be fabricated reproducibly. We would also like to be able to characterize and control the various parameters of the junction including its critical current, normal-state resistance, and capacitance. A lithographic fabrication method would be preferred in order to allow this control, and to allow fabrication of large numbers of devices for arrays and integration with antennas and other coupling structures. Also, a high-frequency device should have a reasonable overall impedance which will allow good coupling of incoming and outgoing signals. Finally, Josephson devices which have hysteretic current-voltage characteristics present difficulties in obtaining stable bias and allow for chaotic behavior. We would therefore like to be able to avoid hysteresis in mixer applications.

Nearly all previous work on Josephson mixers utilized superconducting point contacts as the nonlinear element. These point contacts are essentially just a small superconducting whisker contact. The conduction in these devices is thought to come from tunneling through a thin oxide on the whisker or perhaps also through small superconducting regions which act as weak links. Due to their manner of construction, however, their electrical properties depend on the native oxide which is formed and also the contact force and orientation of the tip. They were therefore fairly unstable, often changing after exposure to room air or upon thermal cycling, which presents serious drawbacks for most applications. Nonetheless, Nb point contacts did attain (*e.g.*, Claassen and Richards, 1978b; Taur and Kerr, 1978; Blaney, Cross, and Jones, 1982) the desirable electrical qualities of fairly high resistance (20-80 Ohms) and fairly large (1-2 mV) $I_C R_N$ product. There was, however, some non-ideal behavior present in point contacts. Some devices showed gap structure in the current-voltage characteristic, which indicates that conduction due to tunnelling of quasiparticles is important. Other structures in the I-V curve, possibly due to self-heating or other nonequilibrium effects, were observed. These effects reduce reliability and hinder comparison with theoretical predictions, as well as possibly degrading mixer performance.

Other nonhysteretic Josephson devices such as SNS weak links or microbridges have the

drawback of reduced $I_C R_N$ products. A large $I_C R_N$ product leads to a large critical frequency, and improved performance at high frequencies. We will describe the rationale for using resistively-shunted tunnel junctions in the following section. Although we will see that this shunting procedure also reduces $I_C R_N$, the reduced $I_C R_N$ products (relative to an unshunted junction) of microbridges and SNS devices is essentially due to the fact that some less well-defined form of shunting is incorporated into the devices.

6.2. Motivation for Shunted Tunnel Junctions

In order to perform a meaningful evaluation of the potential of Josephson mixers as high frequency mixers, we would like to produce a stable, well-characterized Josephson device with a large $I_C R_N$ product. The best prospects for large $I_C R_N$ products remain with devices based on high-T_C materials; recent work has shown the possibility of $I_C R_N$ products as high as 10 mV (Rosenthal and Grossman, 1994). We saw in Chapter 4 that best mixer performance was obtained at frequencies of about half the critical frequency, $\omega_C = \frac{2e}{\hbar} I_C R_N$. This means that for heterodyne detection at 500 GHz, we would like an $I_C R_N$ product of about two millivolts; high-T_C devices might be operable up to several THz. In addition, we would like a device impedance of about 50 Ω for good RF matching, and a single-valued I-V curve. In Chapter 2, we saw that the amount of hysteresis in a device was dependent on the β_C parameter, with hysteresis occurring for values of β_C greater than one. Fabrication of reliable high-T_C devices continues to be an area of development, and there are many difficulties in obtaining stable, high-impedance devices. Unfortunately, we did not have access to a supply of devices using these materials, which hold the most long-term promise for producing sensitive high-frequency Josephson mixers.

The most reproducible superconducting devices currently available are superconductor-insulator-superconductor (SIS) tunnel junctions. These devices have the maximum theoretical $I_C R_N$ product, which is equal to $\pi/4$ times the gap voltage (Ambegaokar and Baratoff, 1963) for a weakly-coupled BCS superconductor. It is possible to produce small-area SIS junctions using photolithography which have sufficiently high resistances for RF use. A drawback of these devices, however, is

TABLE 6.1
SUPERCONDUCTING PROPERTIES OF NB AND NBN

	Nb	NbN
Bulk T_C [K]	9.50 [a]	~17 [b]
Energy Gap (2Δ) [10^{-3} eV]	3.05 [a]	5.8 [b]
Observed V_{Gap} [mV]	2.9	4.75
$I_C R_N$ Product [mV]	2.0	3.0

[a] This is the maximum value attainable for pure, single crystal material (from Kittel, 1976).

[b] From high-quality films deposited at high temperatures (Shoji *et al.*., 1992).

that they consist of two superconductors separated by a very thin (roughly 10 Å) insulating layer. This results in a large parasitic capacitance between the layers, and causes tunnel junctions to have large values of β_C and highly hysteretic I-V curves. This parasitic capacitance is also detrimental to the performance of SIS mixers, as this large reactance must be compensated in order to efficiently couple the incoming signal to the nonlinear tunnelling resistance which performs the mixing. The effects of the capacitance can be reduced by minimizing the RC product of the device, which is independent of device area. In a tunnel junction, the resistance depends exponentially on the barrier thickness, while the parasitic capacitance varies as the inverse of the thickness. This means that reducing the barrier thickness and increasing the tunneling current density can reduce the RC product of the device.

Two materials in which high-current density tunnel junctions for SIS mixers have been developed are niobium (Nb) and niobium nitride (NbN). These materials are desirable for high frequency work because their relatively high transition temperatures lead to large gap voltages and $I_C R_N$ products. A process for producing high quality Nb tunnel junctions with oxidized aluminum (Al) barriers was first developed by Gurvitch *et al.* (1983). Current densities of up to 10,000 A/cm^2 with good quality I-V curves have been obtained using a version of this process at the Microdevices Laboratory of the Jet Propulsion Laboratory (JPL) by LeDuc *et al.* (1992). A process for high-current density NbN/MgO/NbN junctions has been developed by Stern *et al.* (1992). A summary of the gap voltages and $I_C R_N$ products of these junctions is provided in Table 6.1.

As mentioned above, even these high-current density junctions have relatively large capaci-

TABLE 6.2
PROPERTIES OF NB AND NBN TRILAYERS

	Nb	NbN
Current Density [A/cm^2]	10,000	30,000
R_NA Product [Ohm-μm^2]	20	9
Specific Capacitance (ξ_{SP}) [fF/μm^2]	85 [a]	130 [a]
Unshunted β_C	10	10
$I_C R_N$ Product after Shunting [mV]	0.6	0.93
Required Area for Shunted Junction of 50 Ohms [μm^2]	0.1	0.06

[a] J.A. Stern, private communication, 1994.

tance. The maximum attainable current density in Nb and NbN, the specific capacitance (ξ_{SP}) per unit area, and the resistance-area (R_NA) product for these current densities are shown in Table 6.2. Note that the value of β_C for any junction is independent of device area, since I_C and C are proportional to area, and R_N is inversely proportional to area. The values of β_C are much greater than one, and there will be significant hysteresis. There are several methods which could be used to reduce the β_C value of these tunnel junctions. First, the critical current could be reduced via the application of a magnetic field. However, this procedure will reduce the $I_C R_N$ product of the junction by a factor of $1/\beta_C$, resulting in $I_C R_N$ products much less than a millivolt for β_C values of one or less. Another method would be to attempt to increase the current densities and thus decrease the RC product of these trilayers even further. However, for the current densities listed in Table 6.2, the barriers may already be approaching a single monolayer in thickness. Attempts at increasing the current density of NbN/MgO/NbN edge-geometry junctions were made, but not surprisingly, the I-V curve quality degrades, there is a large amount of sub-gap conduction (presumably through barrier pinholes), and the $I_C R_N$ product eventually decreases. A third method would be to add a parallel resistance to the junction, thereby reducing the normal state resistance while holding the critical current and the capacitance fixed. Since β_C is proportional to the square of the resistance, the $I_C R_N$ product need only be reduced by a factor of $\sqrt{\beta_C}$. This is the procedure used in the fabrication of the Josephson-effect devices discussed in this thesis.

The next-to-last entry in Table 6.2 indicates the expected $I_C R_N$ product of tunnel junctions

which are optimally shunted with resistors to yield β_C values of about one. Obviously, the reduction of the $I_C R_N$ product is extremely undesirable since we are interested in developing high-frequency receivers based on these devices. Using the process described below for fabrication of shunted junctions, it was possible to control the amount of hysteresis. However, noise and receiver measurements with hysteretic devices show that this hysteresis is undesirable (see Chapters 7 and 8). Notice that because of the relatively higher specific capacitance of the NbN/MgO/NbN trilayers, some of the advantage of the higher gap voltage is negated. In addition, there were unavoidable parasitic capacitances from the junction contacts and resistor which tended to increase the initial junction capacitance, thereby requiring stronger shunting and additional reduction of $I_C R_N$ products. Another disadvantage of the shunting is that the impedance of the junction is reduced. In order to have final impedances of about 50 Ohms, the initial junctions must be a factor of several (*i.e.*, $\sqrt{\beta_C}$) higher in resistance. For these high-current densities, this requires submicron-sized junctions and some additional complications in fabrication.

6.3. Junction Fabrication Procedure

The process for fabrication of the shunted junctions is based on the standard trilayer process for SIS junctions, and is very similar for both Nb and NbN junctions. A schematic of the fabrication steps is depicted in Figure 6.1. First, a "trilayer" sandwich of superconductor/insulator/superconductor is deposited in sequential steps within a high-vacuum deposition system. After patterning of gross features, the junction active area is defined and the top layer of superconductor around the junction is etched away. Using a self-aligned lift-off process, an insulating layer of silicon monoxide (SiO) is evaporated to "planarize" the junction by filling in the area where the superconductor was etched. Finally, a superconducting counterelectrode is deposited and patterned to contact the device. For resistively-shunted junctions, a resistor material is deposited and patterned on top of the SiO before counterelectrode deposition. The counterelectrode step then serves to contact both junction and resistor. The shunting leaves the active area of the resistor exposed while the junction is protected by the counterelectrode. Junctions could then be tested and

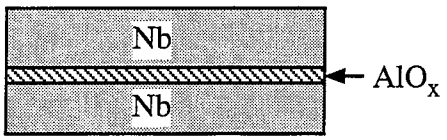

Trilayer Deposition

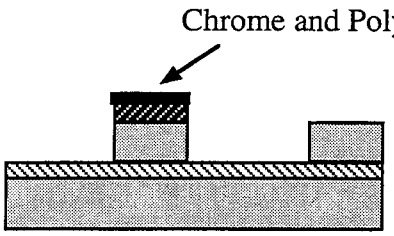

Pattern Junction
and
Etch with RIE

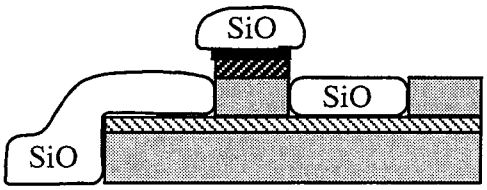

Planarize w/ SiO

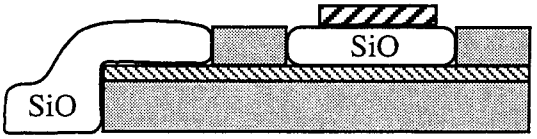

Liftoff SiO
and
Deposit AuGe Resistor

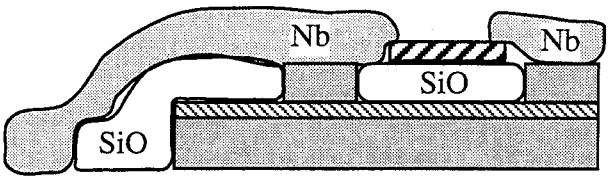

Deposit and Etch Nb Counterelectrode

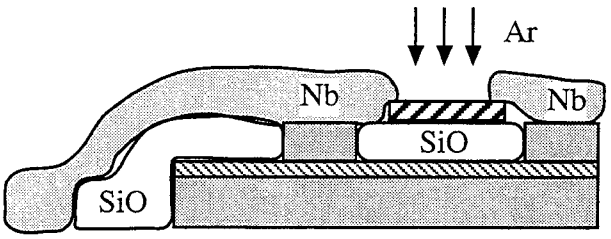

Trim Resistor by Argon Ion Milling

Figure 6.1 Fabrication steps for Nb shunted junction process.

the resistors could be trimmed by ion bombardment to allow fine tuning of the amount of shunting and compensate for variations in junction current density. The shunting process could be applied to either Nb or NbN junctions in the same way. The only differences lie in specifics of deposition and patterning of the respective trilayers. Some relevant specifics of the fabrication steps for Nb trilayer junctions are described below.

Trilayers were formed in a UHV system which had base pressures of about 10^{-8} Torr, and is load-locked to allow rapid introduction and exchange of samples without lengthy pumpdowns. Nb films were formed by DC magnetron sputtering in an argon atmosphere. The chamber pressure affects the stress of the deposited films, and films with slightly compressive stress were found to give tunneling characteristics with lowest leakage. Typical thicknesses for the Nb base layer were about 2,000 Å. An aluminum film 50-80 Å thick was then sputtered. This Al layer was partially oxidized in the same chamber by a high-voltage discharge in an atmosphere of Ar and O_2 for about 30 minutes. Trilayer current density was controlled by the oxygen partial pressure and length of oxidation. A final layer of 1000 Å of Nb was the sputtered and a cap layer of 300 Å of gold was evaporated. This gold layer allowed clean contacting of the completed junction by the counterelectrode, and is sufficiently thin that it becomes superconducting via the proximity effect and does not adversely affect the junction characteristics. The trilayers were patterned with standard contact lithography, usually by lift-off.

Device areas were patterned on the trilayer and then the top layer of Nb was removed within a window around the junction using reactive-ion etching (RIE). Areas larger than about 1 μm were patterned with optical lithography, but the submicron-sized junctions for shunted mixers were defined using direct-write electron-beam lithography. In this process, the wafer is coated with a special resist (PMMA) and exposed only in the junction areas (squares) by writing with an electron beam. This step was performed in the JPL Micro-Devices Laboratory using a JEOL JBX5 e-beam machine by Rich Muller. The e-beam resist is then used to lift-off an evaporated chromium film, which serves as an etch mask for the subsequent junction definition etch. Reactive-ion etching was used to define these very small areas because its directionality minimizes undercutting of features.

Nb etching was performed using a gas mixture of Freon 12 (CCl_2F_2), Freon 14 (CF_4), and oxygen. Silicon monoxide planarization (approximately 1200 Å thick) was carried out by angled evaporation through the same etch mask. The SiO insulator could then be lifted off by dissolving the resist and wet etching the chromium mask.

Optical lithography for the resistors was performed, and AuGe eutectic resistor material was thermally evaporated to form a film 100-300 Å thick. More information on resistor design and the choice of materials is given in the following section. Resistors were sometimes made intentionally thicker than necessary so that a post-fabrication trimming could be performed. After resistor lift-off, the samples had approximately 3500 Å of Nb counterelectrode sputtered over the entire wafer. This layer was then patterned and etched with RIE. Dies of 10 devices were diced and wire-bonded into chip carriers. I-V curves of these devices could then be measured by dunking in a liquid helium storage dewar. If trimming was desired to reduce the amount of shunting and optimize the $I_C R_N$ product, ion-milling with argon could be carried out and the devices retested. An electron micrograph of a completed junction is shown in Figure 6.2. The properties of the resulting shunted junctions are described in Section 6.5.

6.4. Resistor Implementation

Since we wished to shunt the tunnel junctions without introducing unwanted parasitic reactances or spurious high-frequency resonances, it was important that the resistors present a purely real impedance to the junction over a very wide frequency range. The process of fabricating the resistors on top of the planarization layer, as described above, allowed the bottom Nb layer of the etched trilayer to act as a ground plane for the resistors. In Figure 6.2, we see the counterelectrode which contacts the junction and one end of the resistor. Another small section of counterelectrode contacts the other end of the resistor and carries the current off the planarization layer to contact the trilayer. There are two parallel current paths, through the junction down into the trilayer to ground, and through the resistor to the top of the trilayer and through the very large area junction (which is an excellent DC and RF short-circuit) formed by the remaining trilayer to ground. This

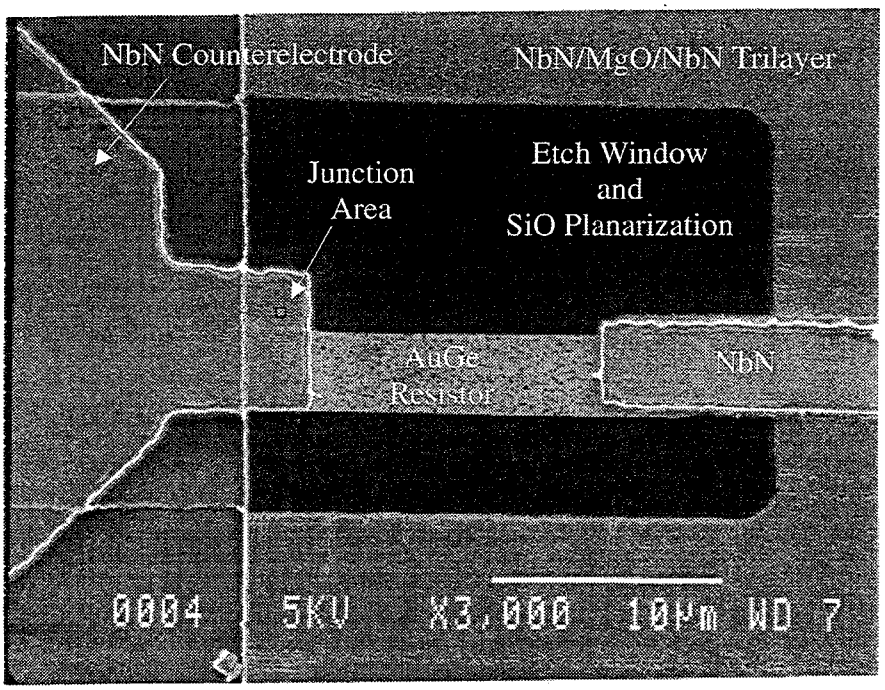

Figure 6.2 Scanning electron micrograph of shunted NbN tunnel junction. The trilayer fills the right $\sim$ 3/4 of the image, and has been etched and planarized with SiO in the dark rectangle. The junction, approximately 0.3 μm on a side, is just barely visible under the counterelectrode which enters from the left. The resistor and its contact to the trilayer (far right) can also be seen. The white bar represents 10 μm.

structure was chosen to minimize the reactance of the resistor and can be analyzed as a section of microstrip line to determine its impedance.

The impedance of a short-circuited section of very lossy microstripline is developed in Appendix A. The impedance in terms of the physical parameters of the microstrip (*cf.* Section A4) is

$$Z = \sqrt{\frac{R_\square h}{2\epsilon_0 \epsilon_r w^2}} \frac{1}{\sqrt{\omega}} (1 - \jmath) \tanh \left[\sqrt{\frac{R_\square \epsilon_0 \epsilon_r}{2h}} \sqrt{\omega} (1 + \jmath)\, d \right], \tag{6.1}$$

where w is the width of the resistor, h is the height of the SiO insulator, ϵ_0 and ϵ_r are the permittivity of free space and the relative dielectric constant of the SiO, $R_\square$ is the sheet resistance of the resistor, and d is the length of the resistor section. Typical values for these parameters are shown in Table 6.3. Note that Equation (6.1) does not depend on the penetration depth of the superconductor. Using these parameters we can display the real and imaginary parts of the impedance of the resistor as a function of the frequency, ω, or the length of the line, d. These are displayed in Figure 6.3. One may

TABLE 6.3
SHUNT RESISTOR FABRICATION PARAMETERS

Width	w	2 μm
Dielectric Thickness	h	1200 Å
Dielectric Constant	ϵ_r	5.8
Nb Penetration Depth	λ	800 Å
AuGe Resistivity	ρ	10 $\mu\Omega$ cm
Resistor Thickness	t	100 Å
Sheet Resistance	$R_\square$	10 $\Omega/\square$
Resistor Length	ℓ	10 μm
Resistance	R	50 Ω
Estimated Capacitance [a]	C_{par}	1.7 fF

[a] This is the effective capacitance of the resistor which appears in parallel with the resistance, see text.

expect some deviation from this behavior above the gap frequency of the superconductor ($\sim$ 750 GHz for Nb) since the groundplane has been assumed to be lossless. This effect will probably be small, however, given the large loss in the top conductor.

The imaginary part of the resistor's impedance is negative, and is essentially the net effect of the resistor's distributed capacitance to ground. One can re-express the general resistor impedance as a parallel combination of two elements, one which is purely real (the desired shunt resistance), and one which is purely imaginary. This parasitic element is well approximated by a capacitance over a wide range of frequencies, and its magnitude is about 2 fF (see Table 6.2). This capacitance, and the capacitance of the counterelectrode contacting the junction, lead to a significant but unavoidable increase in the capacitance. The junctions must therefore be somewhat overshunted, and this leads to about a 30% decrease in the available $I_C R_N$ product.

Several resistor materials were investigated, and the key requirement was for a sufficiently high sheet resistance ($R_\square$) in attainable films. Materials such as titanium (Ti) and copper (Cu) were studied, but the resistivity of these reactive elements varied due to the variation in chamber pressure and contaminants present during deposition. Pure gold gave unacceptably low values for the resistivity. The gold-germanium (AuGe) eutectic material (88% Au and 12% Ge) is readily available since it is used for contacts in semiconductor processing. Because of the large amount of impurity scattering, the resistivity was nearly independent of temperature. This is advantageous since the

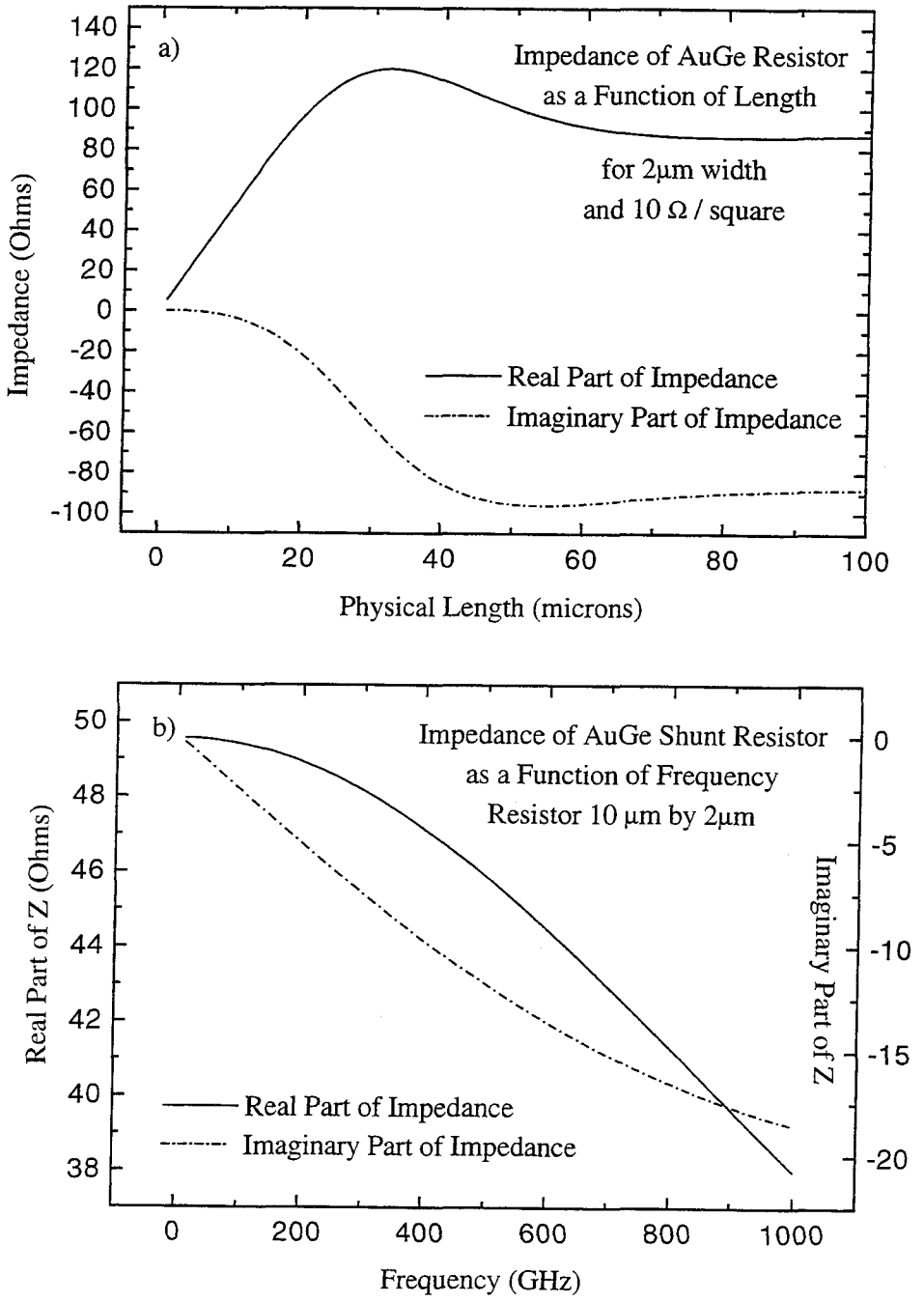

Figure 6.3 Impedance of a shortcircuited section of resistor "microstrip." a) The impedance as a function of the physical extent of the resistor in microns (μm) at 100 GHz, for the nominal resistor parameters given in Table 6.3. The real part of the impedance is the full line, and the imaginary part is the dash-dotted line. b) The impedance as a function of frequency (in GHz) for a resistor 10 μm long. The imaginary part of the impedance increases with frequency, while the real part decreases slightly.

resistance at room temperature can be measured to ensure that the device is intact before mounting for RF testing. Test structures were fabricated and examined to ensure that there was no significant contact resistances formed at the superconductor-resistor interfaces. In addition, the AuGe was found to be compatible with the junction process since it was resistant to the counterelectrode etching step. The resistivity of the films scaled well with thickness, and thermal evaporation of the eutectic gave consistent bulk resistivities. Even the thin films used for the resistors ($\sim$ 100 Å) did not change their properties over time or upon exposure to air.

6.5. Device Results

The junction process described above was applied to produce the junctions used for the measurements in this thesis. As mentioned, these devices had the desirable properties of robustness and stability. Furthermore, the junction parameters such as resistance, critical current, and amount of hysteresis could be controlled. Critical current of the junctions scaled well with junction area (after accounting for the small undercutting of features in junction etching), and variation among devices from the same wafer was small (10-20%). Normal state-resistances in the 30-50 Ohm range were routinely obtained. Devices were typically fabricated on 100 μm (0.004 in) thick fused quartz substrates. RF testable devices were integrated with a microstrip choke structure to allow efficient coupling to the waveguide mount at 100 GHz (*cf.* Chapter 8).

Devices fabricated with the shunted junction process showed single-valued I-V curves which were very similar to those predicted by the RSJ model. Because of the relatively strong shunting, normal state resistances were essentially determined by the resistor values. The I-V curves did show small current increases at the gap voltage of the superconductor used. These were due to the change in conductance of the underlying tunnel junction at the gap rise. These effects in the I-V curve were small, however, due to the strong shunting. Some structure in the I-V curves was seen due to resonances in the RF choke structure or the waveguide. Two slightly different masks with variations in the resistor geometry showed no systematic variation in these structures, which confirms that there were no resonances due to the resistors themselves.

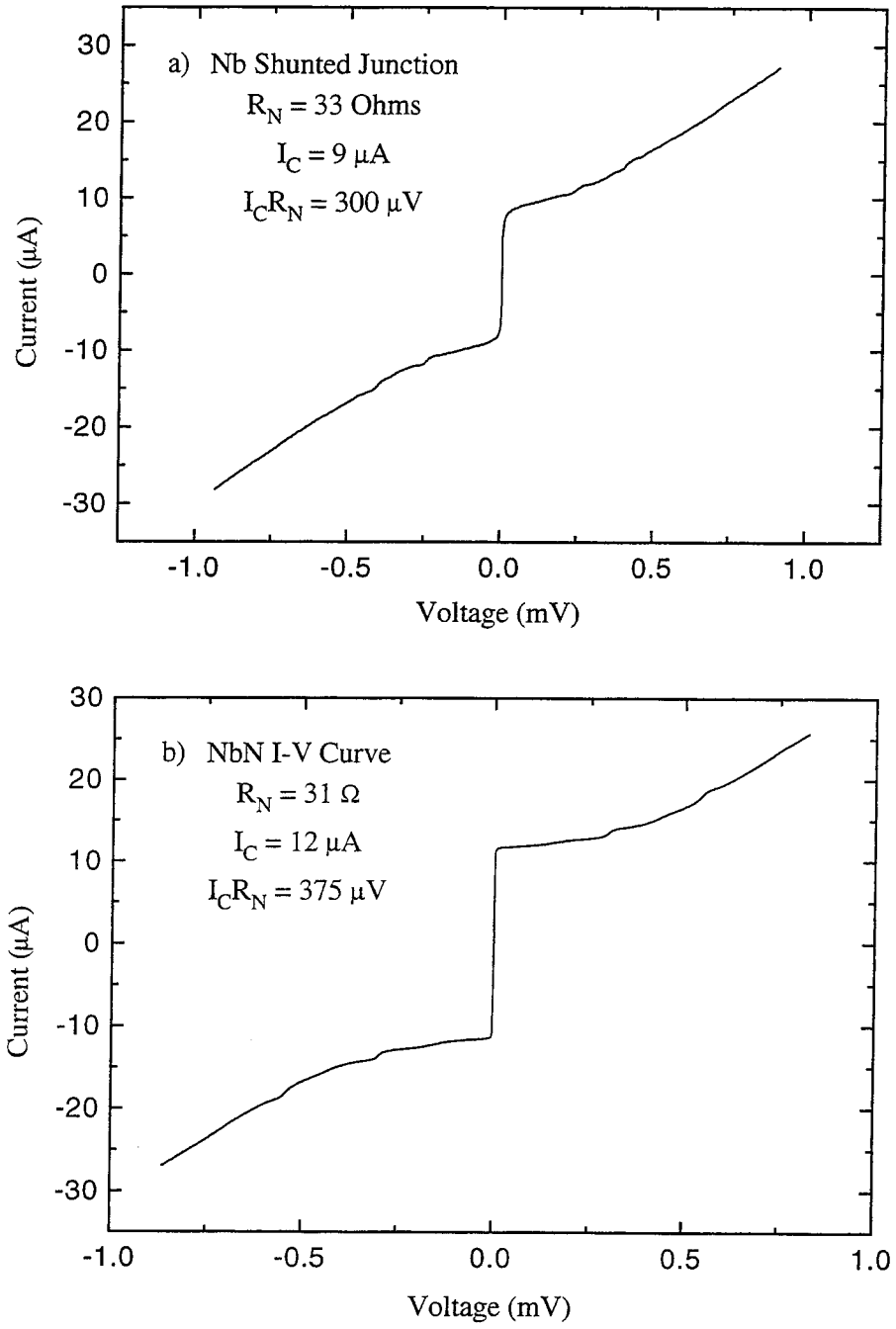

Figure 6.4 Current-voltage characteristics of shunted junctions. Both junctions are shunted so that the I-V curves are completely nonhysteretic (*i.e.*, $\beta_C \sim 1$). a) Nb shunted junction. Normal-state resistance is 33 Ohms, critical current is 9 microamps, and $I_C R_N$ product is 300 microvolts. b) NbN shunted junction. Normal-state resistance is 31 Ohms, critical current is 12 microamps, and $I_C R_N$ product is 370 microvolts.

Because of the additional parasitic capacitances of junction contacts and resistors, the available $I_C R_N$ products for nonhysteretic junctions were somewhat reduced from those predicted in Table 6.2. The best $I_C R_N$ values for the Nb junctions were about 0.5 mV. The parasitics were relatively more important for the very small NbN junctions, giving $I_C R_N$ products of about 0.6 mV. While these are too small for interesting submillimeter-wave mixing, we would expect nearly optimal performance at 100 GHz. A pair of representative I-V curves for the two materials are depicted in Figure 6.4. The detailed shape of the I-V curves, fitting of curves to the RSJ model, and the noise of the devices is discussed further in the following chapter.

Chapter 7

Measurements of Noise in Shunted Junctions

An expert is someone who knows some of the worst mistakes that can be made in his subject and knows how to avoid them.

– Werner Heisenberg, *Physics and Beyond*

In this chapter, we will present measurements of the noise of shunted junctions at a frequency (1.5 GHz, in L-band) which is a typical intermediate frequency for millimeter and sub-millimeter wave mixers. These noise measurements were undertaken after initial results on heterodyne measurements showed good conversion efficiency, but higher output noise than expected from the RSJ simulations. Direct measurements allowed confirmation that the reduced receiver sensitivity was in fact due to large junction noise and not due to a flaw in receiver design or implementation.

The frequency at which the measurements were made is low enough compared to most of the typical frequencies of the junction (*i.e.*, $\omega_C \sim 200$ GHz, while $\omega_J \sim 50$ GHz at $100\mu V$ bias) that we can compare with the Likharev-Semenov model for very-low frequency noise, but high enough that any 1/f noise is negligible. The microwave test system used for the measurements allowed an accurate determination of the available noise power from the junction as a function of bias voltage, taking into account any changes in the coupling due to variation of the junction's dynamic resistance. It was found that the noise was often drastically different from that predicted by the RSJ model,

due to the effects of the frequency-dependent impedance of the RF coupling structure in which the junction is mounted. While the LS model qualitatively reproduced some of the structure in the noise as a function of voltage, there were discrepancies noted which are probably caused by the breakdown of the LS model due to the interaction of the junction with this external circuit. The noise could be measured both with and without a local oscillator applied, and the output noise of the pumped junctions was consistent with that implied by heterodyne mixer noise temperature measurements.

7.1. Noise Measurement Apparatus and Technique

To make absolute measurements of the output noise of the shunted junctions as a function of bias voltage, we needed to calibrate the IF amplification system and determine the power coupling efficiency between the junction and the low-noise amplifier (LNA). We also needed to change the bias and possibly the RF coupling structures seen by the junction, and allow for the introduction of a local oscillator to study the noise under conditions similar to those used for the mixing experiments. The microwave test apparatus used for these measurements is shown schematically in Figure 7.1. All components were bolted to the cold plate of the liquid helium cryostat, with the exception of the variable load and the LNA, which is cooled by a closed-cycle refrigerator to about 12 K. Basically, the system consisted of a low-noise 1.5 GHz amplifier and a calibration load to allow the gain and noise of this amplifier to be accurately determined. The junction was mounted in a fixture which could be the waveguide block used for heterodyne mixing measurements, or a simplified structure in which the junction is only weakly coupled to the exterior. A bias-tee served to introduce the DC bias to the junction and attempted to match the junction output to the 50 Ohm amplifier circuit. Finally, the directional coupler and noise tube allowed the introduction of a test signal, which could be reflected off the junction in order to measure the power coupling coefficient between the junction and amplifier.

The IF amplifier was similar in design to that described by Weinreb *et al.* (1982), with the first stage replaced with a high-electron-mobility transistor (HEMT) to improve the noise performance. The amplifier's bandpass was from 1.25-1.75 GHz, in which the gain was about +27 dB, with a

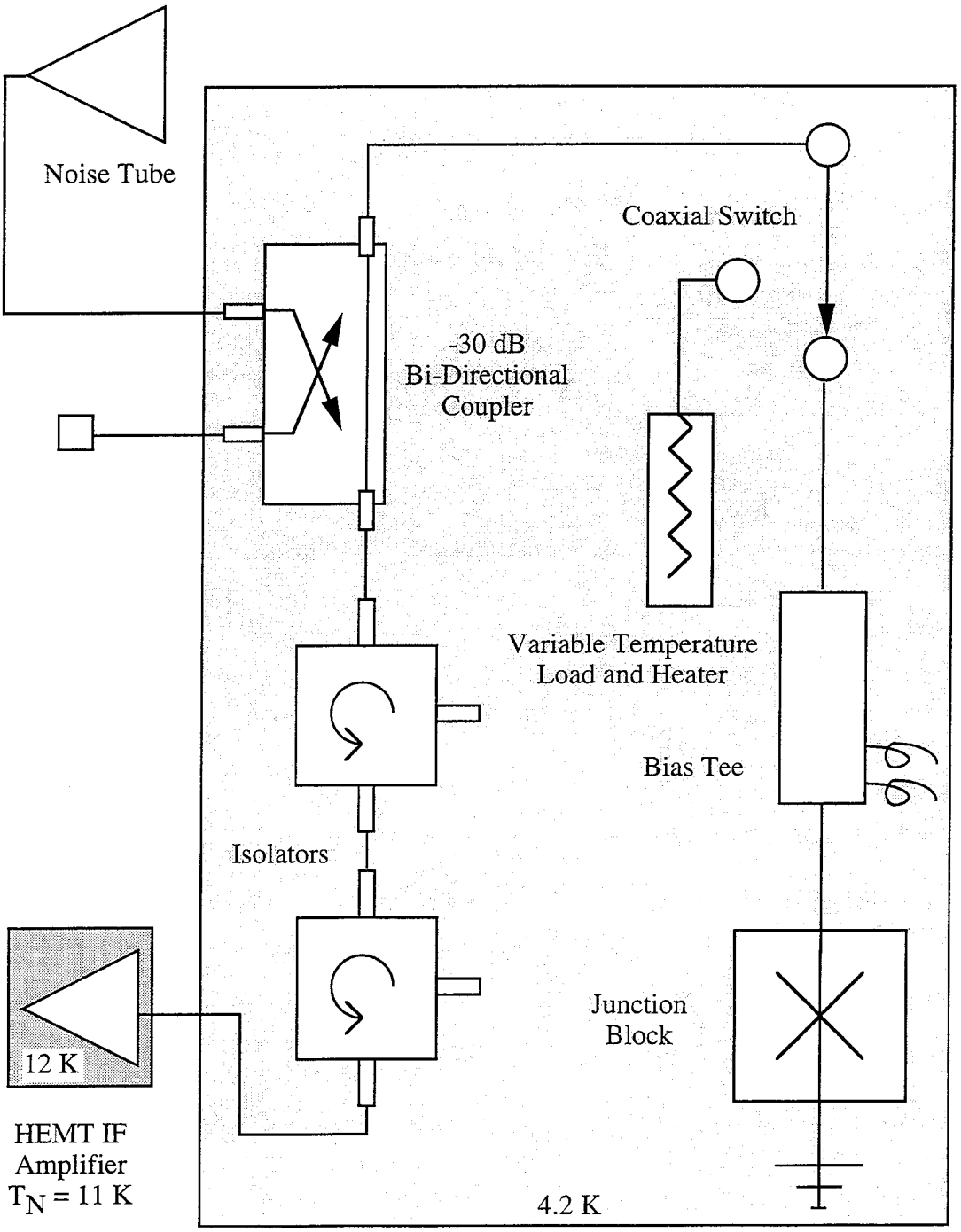

Figure 7.1 Schematic of IF noise measurement apparatus.

noise temperature of typically 10-12 K, depending on bias conditions. Noise temperatures more than a factor of two lower (Padin and Ortiz, 1991) are available at these frequencies, but since the noise of the amplifier could be well calibrated and removed from the data, this noise was not a significant source of error. In order to calibrate the IF amplifier in absolute terms, a coaxial switch (SPDT latching coaxial switch, part #909C70200, Daytron/Transco, Simi Valley, CA) could be used to connect the amplifier input to a variable-temperature termination. The termination was of a design described by McGrath *et al.* (1986), consisting of a section of stainless-steel coaxial cable terminated with a chip resistor. The end of this coaxial cable carried a heater resistor and a temperature sensing diode (DT-500 diode, Lakeshore Cryotronics, Inc., Westerville, OH). When heated, the Johnson noise of the termination in the measurement bandwidth varies with temperature and allows the gain (in watts of output power per Kelvin) and noise (in Kelvin) of the amplifier to be measured. An approximately 5 centimeter (2 inch) long piece of 0.5 millimeter (0.02 inch) diameter copper wire served as the thermal link to the liquid helium bath, and gave a thermal time constant for the load of approximately 10 seconds. The termination was measured to have a return loss of more than -14 dB at cryogenic temperatures. The temperature sensor was calibrated by immersing it in liquid helium. The inaccuracies in the temperature sensor and its linearity probably dominate the uncertainty on the IF system calibration, and we estimate the error to be less than $\pm$ 0.5 K. A personal computer was used to control the heater power and monitor the load temperature, allowing for an automated calibration procedure. A typical calibration run is displayed in Figure 7.2, which shows the excellent linearity and a linear regression used to determine the IF gain and noise.

Since we are interested in the available noise power from the junction, we must correct the measured IF output power for the variation in the IF mismatch between the junction and amplifier system. In principle, the dynamic resistance can be measured, and the coupling predicted as a function of the impedance of the junction. Based upon a model of the IF system, the predicted coupling could then be used to make the correction. This method was used recently to investigate the noise of high-T_c weak links (Grossman and Vale, 1994). However, this method can introduce systematic errors which might depend on the impedance of the junction. Alternatively, one can

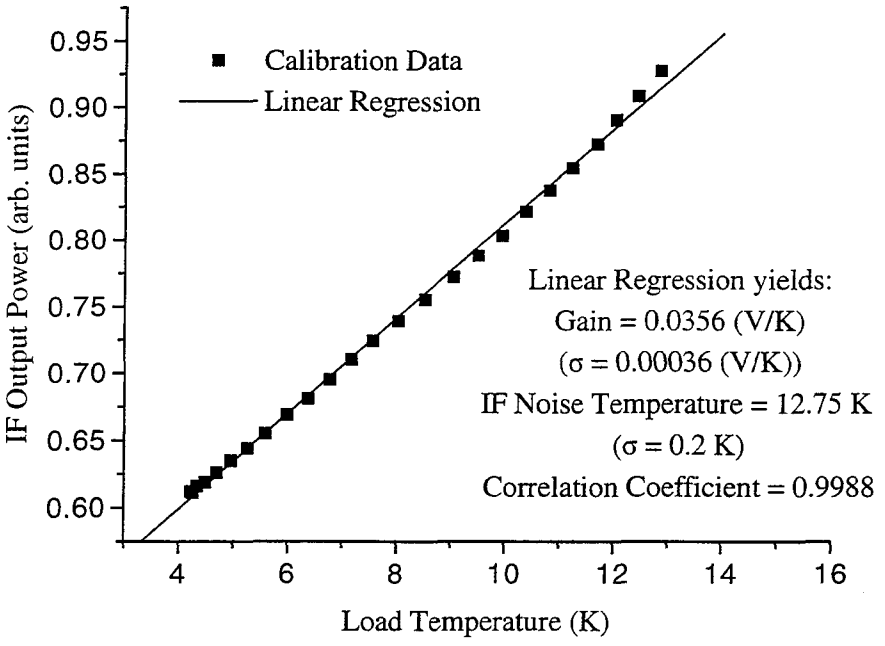

Figure 7.2 Typical IF system calibration for junction noise measurements. The total IF output power, expressed as millivolts detected on a crystal detector, is plotted as a function of the termination temperature. Approximately 1 minute is allowed for thermal equilibration between each different heater setting. Also shown is the best-fit line and regression parameters obtained from the data.

measure the power reflection coefficient of the junction directly. The inclusion of a high-directivity directional coupler (Technical Research and Manufacturing, Inc., model DCS-305, Bedford, NH) allowed a signal from outside the dewar to be introduced into the system, directed either toward the junction or toward the amplifier. A noise tube (HP346B, Hewlett-Packard, Santa Clara, CA), filtered to the 500 MHz band of the amplifier, was used as the test signal. The strength of this signal typically increased the total noise by about 20%. As expected, no difference was observed between the junction I-V curves with the noise tube on or off, verifying that the test signal did not grossly affect the junction properties. The weak coupling of the directional coupler (-30 dB) meant that very little noise is coupled from the room temperature terminations when the noise tube is off. This noise simply causes a small ($\lesssim$ 0.3 K) increase in the measured IF system temperature. The directivity of the coupler was measured to be greater than 23 dB at cryogenic temperatures. This finite directivity of the coupler introduces a systematic error which probably dominates the error

in the coupling, and is worst for large mismatches between junction and amplifier. Two isolators (Pamtech 1.25-1.75 GHz isolator, Pamtech, Inc., Canoga Park, CA), each with a directivity of about 20 dB, followed the coupler to prevent standing waves and any contamination from reflected noise waves from the amplifier.

The difference in the IF system total power with and without the noise source applied gives a measure of the reflection coefficient. When the junction is biased on the critical-current in its zero-voltage state, its dynamic resistance is very small, and it can serve as a reference short-circuit. The power reflection coefficient of the junction, ρ, is therefore given by

$$\rho(V) = \frac{P_{ON}(V) - P_{OFF}(V)}{P_{S-ON}(V) - P_{S-OFF}(V)}, \tag{7.1}$$

where $P_{ON}(V)$ is the power (as a function of the junction bias voltage, V) measured when the noise tube is on, and $P_{OFF}(V)$ is the measured power when the noise tube is off. The denominator, $P_{S-ON}(V) - P_{S-OFF}(V)$, is the difference in these powers when the junction is in the zero-voltage state, and assuming that the junction is a perfect short under this condition, it is proportional to the strength of the coupled test signal from the noise tube. If we reverse the direction in which the signal is coupled, it will travel directly towards the amplifier. This allows us to determine any loss, L, between the coupler and the junction. The loss is given by

$$L = 1 - \sqrt{\frac{P_{S-ON}(V) - P_{S-OFF}(V)}{P_{S-Rev} - P_{S-OFF}(V)}}, \tag{7.2}$$

where $P_{S-ON}(V)$ and $P_{S-OFF}(V)$ are as defined above, and P_{S-Rev} is the power when the noise tube signal is coupled towards the LNA. This loss was determined to be about 0.6 dB ($\sim$ 12%), and includes any loss in the semi-rigid coaxial cable to the junction, reflections within the switch, losses in the bias tee and junction block, and any loss associated with the junction being an imperfect short. This loss is at 4.2 Kelvin, and so it adds a small amount to the IF system temperature. The system temperature is measured in the calibration procedure with the switch connected to a different cable leading to the variable load, so any small difference in this loss could lead to an offset in the determination of the junction noise temperature. The difference in the loss should be smaller

than the total loss measured, so that this leads to an uncertainty of less than 0.4 K (= L times the temperature, 4.2 K), which is comparable to the other uncertainties in the calibration.

Having measured the IF reflection coefficient to the junction as a function of bias voltage, and having determined the IF system temperature through the calibration with the variable temperature load, we can find the available noise power at the junction's output. The output noise temperature, T_J, of the junction, in Kelvins, is given by

$$T_J = \frac{1}{1-\rho(V)} \left(\frac{P_{OFF}(V)}{G} - T_{IF} - \rho(V)\, T_{BATH} \right), \tag{7.3}$$

where $P_{OFF}(V)$ is the IF system output power with only the junction noise at its input, and G and T_{IF} are the measured gain and noise of the IF system. The last term is due to the terminated ports of the isolators, which radiate thermal noise at the bath temperature, T_{BATH}, towards the junction, which is subsequently reflected back into the amplifier. We can see from this expression that the errors in the determination of the junction's output temperature are affected by the strength of the IF coupling. If the coupling were very poor (*i.e.*, $\rho(V) \rightarrow 1$), for example, a small error in the IF system temperature could lead to large errors. Furthermore, the systematics in the reflection coefficient measurement itself, due to the finite directivity of the coupler, are more severe at large reflection coefficients. It is worth noting that the corrections for reflection are nonlinear, so that care must be taken to avoid error if the reflection coefficient is a function of frequency within the band.

The LNA output was typically fed through two temperature-stabilized room temperature amplifiers (Miteq AFD3-010020-15, +38 dB gain and 1.5 dB noise figure, Miteq, Inc., Hauppauge, NY; and Sertek STC8-005, +18 dB gain and 3 dB noise figure, Sertek, Inc., Newbury Park, CA) to give an additional ~60 dB of gain. The total power was then measured with a microwave power meter (ML83A, Anritsu Corp., Tokyo, Japan; or HP 436A) or a crystal detector (HP 8472B). Before power detection, the bandpass was typically filtered to 100 MHz centered at 1.5 GHz. The gain, noise and reflection coefficient did not vary significantly with frequency in this band, as examined with a spectrum analyzer (HP 8562A). As further verification, a few data sets were measured using the spectrum analyzer directly, to select a 1 MHz band for power detection. Analysis of this data

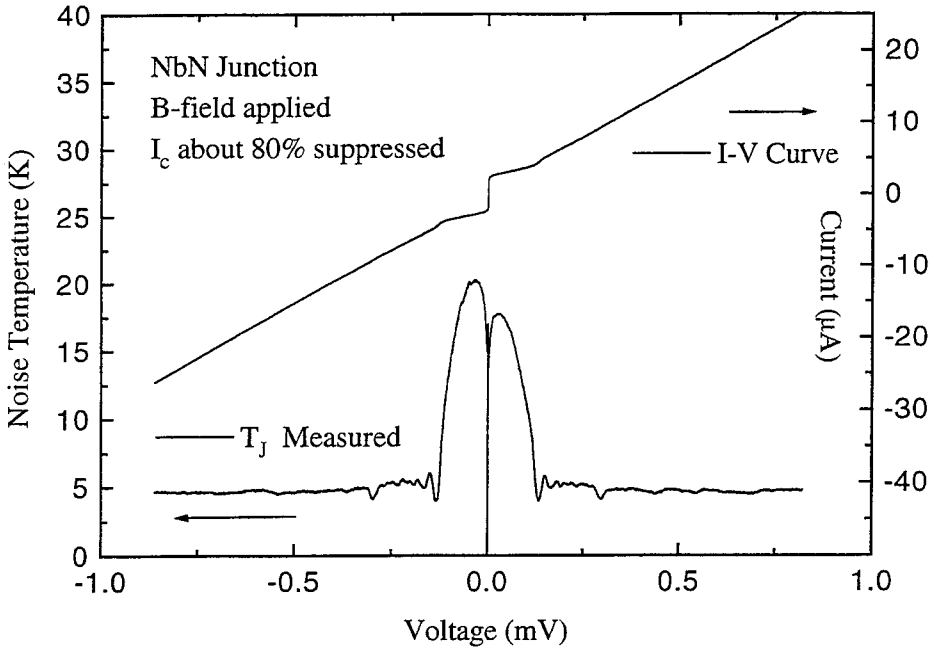

Figure 7.3 A typical plot of junction output noise temperature, T_J, as a function of the applied bias voltage. The I-V curve is also shown for comparison. The high-voltage (greater than $\sim 100\mu$V) noise approaches the expected thermal limit of 4.2 K. The much larger values for the noise attained at voltages comparable to the $I_C R_N$ product ($\sim 80\mu$V) are typical as expected from the RSJ model.

gave identical results to those taken using the 100 MHz bandwidth. The biasing electronics for the junction could be controlled by personal computer, and I-V curves and IF power as a function of bias voltage could be digitized and stored for later analysis.

7.2. General Characteristics of Measured Junction Noise

There are several general features displayed by all of the junctions whose noise was measured, each of which deserve a few comments before we proceed to a detailed comparison of the noise with the RSJ and LS models. Figure 7.3 displays an I-V curve and measured noise as a function of bias voltage for a NbN junction with no local oscillator applied and no RF coupling out of the dewar. In this case, the junction has had a magnetic field externally applied to suppress the critical current to only a few microamps. A superconducting solenoid and high-permeability yoke supplied this field, which could be used to suppress the critical current, providing run-time adjustment of I_C or cancellation of any flux trapped in the junction on cooling.

We see that the noise is independent of bias voltage for voltages greater than the $I_C R_N$ voltage, which is roughly 80 μV in this case. This high-voltage limit is generally slightly higher than the physical temperature of the device (in this case, 4.6 K versus 4.2 K), confirming that the system calibration has been performed adequately well. The statistical uncertainty on the noise measurement is quite small, and several small features which appear at both positive and negative voltage are easily seen. The dominant feature in the noise, however, is the large maxima seen on either side of the critical current at voltages less than the $I_C R_N$ product, where the dynamic resistance is high. This behavior is qualitatively similar to the expected behavior of the unpumped RSJ model, as seen in Chapter 3. An asymmetry of 10-20% in these maxima, which is not expected from the RSJ model, is clearly evident. A similar asymmetry can be discerned in the I-V curve upon close examination. This asymmetry is caused by the chip geometry near the junction, which causes the magnetic fields due to the junction bias current to add to or subtract from the external flux through the junction. The sense of the asymmetry (*i.e.*, which sign of the voltage had the higher noise) could be changed by reversing the direction of the external magnetic field, as would be expected.

There is also a large spike in the measured noise exactly at zero bias voltage. Since the coupling of the junction to the measurement system is exactly zero at this point (by definition), the junction's contribution to the noise is undetermined. In all cases the total IF system output noise at zero voltage is consistent with the noise of the amplifier and the terminations of the isolators alone. In future depictions of junction noise, the divergence in the junction noise (which can be either positive or negative) at zero bias is sometimes removed for clarity. Finally, we can see that there are several small ripples in the junction noise which appear at matching positive and negative voltages. These features correspond well with small changes in the junction dynamic resistance occurring in the I-V curve. Similar features are present in the reflection coefficient as determined using the procedure described in the preceding section. Note that the noise has been corrected for the variation in reflection, so that the observed variation in junction noise represents a true change in output noise temperature with dynamic resistance. More detailed comparisons of the data with

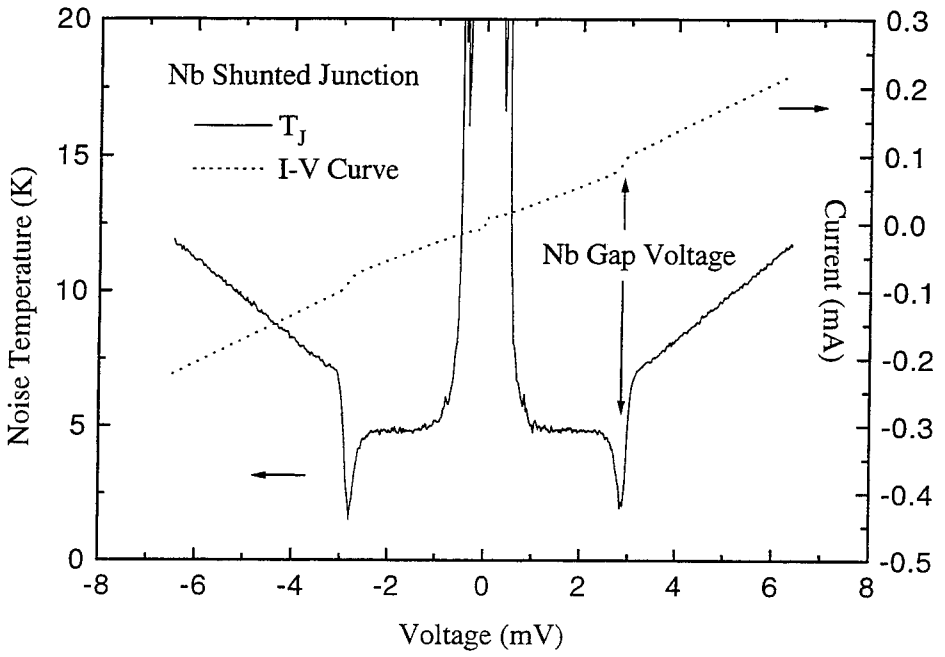

Figure 7.4 I-V curve and junction noise temperature versus bias voltage for a Nb shunted junction, including the region above the gap voltage of the tunnel junction. I-V curve shows a small current rise at the Nb gap of 2.9 mV, due to the increase in conduction of the underlying tunnel junction. The noise also shows structure near the gap, and a linear increase with voltage above the gap, due to the shot noise of the junction.

the RSJ and LS models are presented in the next section.

If we examine the noise at bias voltages higher than the gap voltage of the superconducting tunnel junction on which the device is based, we can see some effects of the quasiparticle tunneling in the junction noise. The noise as a function of voltage on a larger scale for a Nb shunted junction is shown in Figure 7.4. The dotted line shows the I-V curve of the junction. The I-V curve is nonhysteretic, with a critical current of about 8 μA, and a resistance of about 29 Ohms. The device shows a small current rise at the gap voltage of the underlying Nb tunnel junction (2.9 mV), which is as expected, recalling that the device consists of a tunnel junction in parallel with a linear resistor about one fourth of junction's normal state resistance. Similarly, we see structure in the noise at the gap voltage, and an output noise which depends linearly on bias current above the gap. This behavior is just due to the additional shot noise from the tunnel junction when the quasiparticle conduction becomes significant. For a pure tunneling resistance, the effective noise temperature

due to shot noise can be derived by equating the current spectral density, $S_I = 2eI$, to the current spectral density for thermal noise, $S_I = 4k_BT/R$. This gives the "shot noise temperature," $T_{SHOT} = 2eIR/k_B$. For a tunnel junction with no excess current, this can also be expressed as $T_{SHOT} = eV/2k_B$, or 5.8 K per millivolt of junction bias. For our shunted junctions, of course, only a fraction of the total current is due to tunneling of quasiparticles, with the rest passing through the shunt resistor. The variation of the shot noise with bias voltage is then decreased by the same ratio that the junction resistance has been reduced by shunting, typically a factor of three to five. For this junction, the noise increases by 1.5 K for each millivolt of bias. There can also be shot noise due to the small amount of current through the junction in the subgap region. This could explain some of the small elevation of the junction temperature in the "Johnson noise" seen in the subgap region. This elevation was typically somewhat larger for NbN junctions, perhaps due to their relatively larger subgap leakage currents. In any event, the shot noise contribution to the total junction noise is clearly small at the low voltages (less than a mV, comparable to I_CR_N) with which we will mainly be concerned in the remainder of the discussions.

7.3. Comparison of Noise Measurements with RSJ and LS Models

Having described the general behavior of the noise of shunted junctions, we can now examine the noise in the region of strong Josephson nonlinearity (*i.e.*, for voltages less than the I_CR_N product), and see whether this noise is in agreement with predictions of the magnitude of the "excess," based on the RSJ and Likharev-Semenov (LS) models. We will begin with the case of the junction shown in Figure 7.3, which has a fairly small I_CR_N product, and a noise versus voltage curve which is at least in qualitative agreement with that expected, with a single smooth maximum occurring as the voltage is decreased below I_CR_N. We will see later that the noise varied strongly depending on the particular junction parameters and RF embedding circuit presented to the junction.

An I-V curve for a NbN junction with the critical current strongly suppressed (corresponding to Figure 7.3) is shown on an expanded scale in Figure 7.5. Also shown (dotted line) is an RSJ I-V curve with the parameters $\beta_C = 0.3$ and $\Gamma = 0.07$, scaled to fit the measured data. Obviously, there

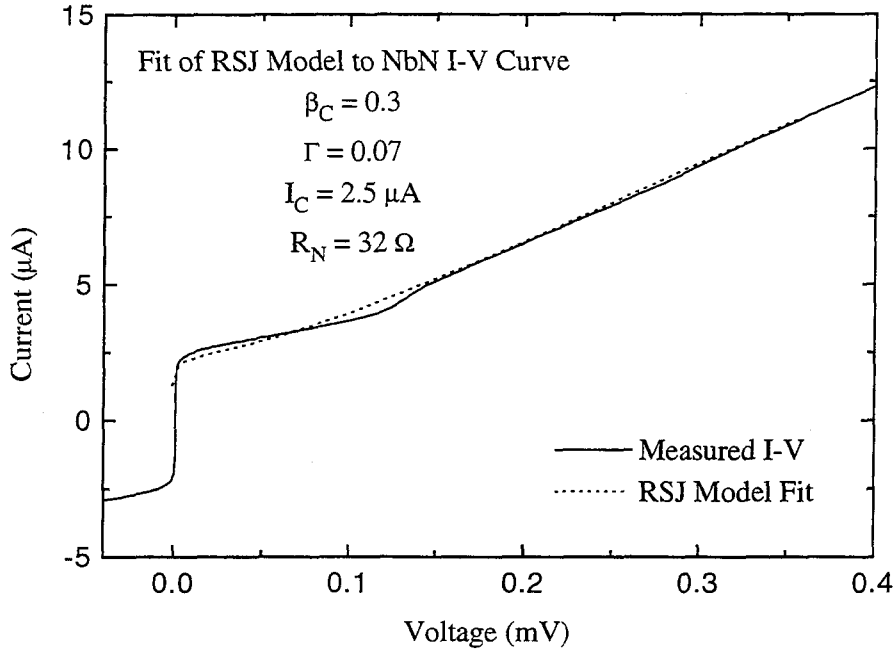

Figure 7.5 I-V curve and RSJ model fit for NbN junction with small $I_C R_N$ product. The RSJ simulation used the parameter values $\beta_C = 0.3$ and $\Gamma = 0.07$. RSJ data were scaled by a critical current of 2.5 μA and a normal-state resistance of 32 Ohms to match the data. Systematic differences between the measured and predicted curves, probably due to the frequency variation of the RF circuit seen by the junction, are clearly visible.

are significant systematic variations between the measured and predicted I-V curves. For example, the kink in the measured I-V curve at about 0.15 mV is not expected from the simple RSJ model with capacitance. Variations in I-V curve shape will be seen to be a general feature of the shunted junctions observed. The curves are qualitatively very similar to the RSJ model I-V curve, but details, such as the presence of resonances and the exact curvature in the region below the $I_C R_N$ voltage, differ from the RSJ predictions because the precise frequency dependence of the junction's external circuit are not included in the modeling.

Having fit the I-V curve, we can then use the RSJ model to predict the low-frequency noise of the junction. The normalized low-frequency voltage noise, $S_v(\Omega = 0)$, was determined at each of the simulation bias points, and then scaled to an available noise temperature at the output in dimensioned units using the relation $T_J = T_{BATH} \times S_v / 4\Gamma r_d$. The low-frequency noise as measured and as predicted in this manner from the RSJ model are displayed in Figure 7.6. We can see that the

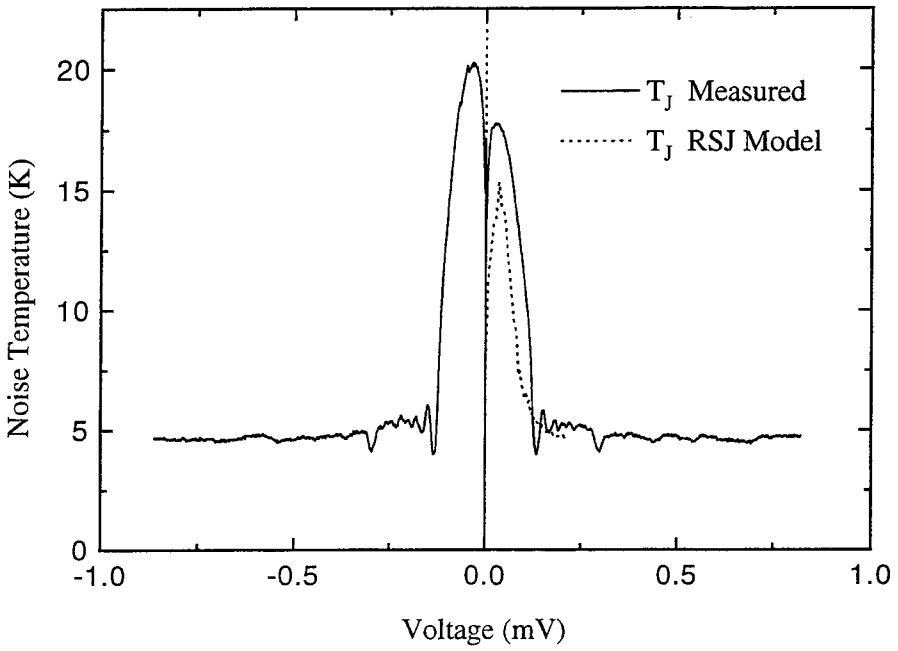

Figure 7.6 Comparison of measured noise (full line) versus noise predicted by RSJ simulation (dotted line) with parameters used in Figure 7.5. General scale and voltage dependence of noise is fairly consistent between model and experiment, despite the discrepancies seen in I-V curve.

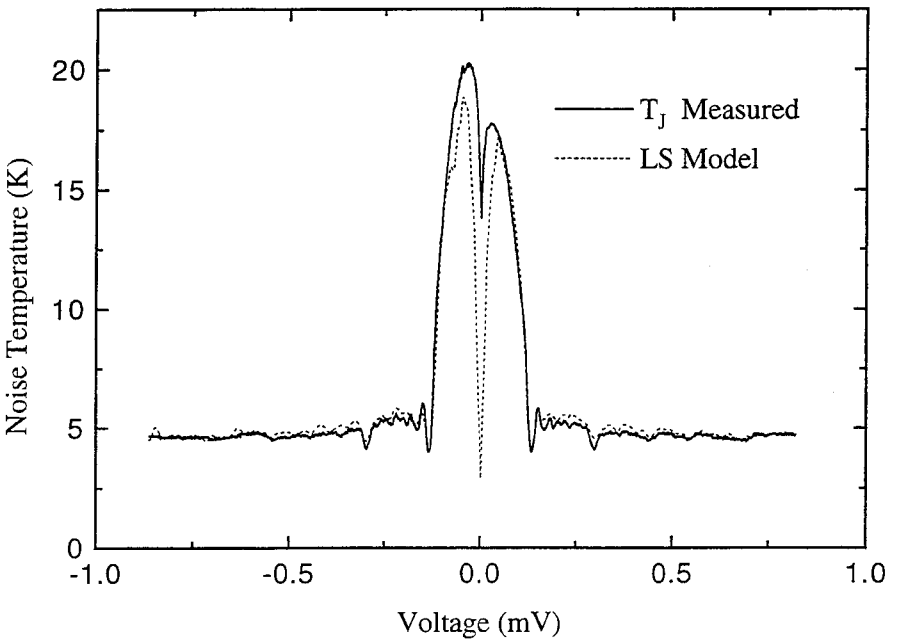

Figure 7.7 Comparison of measured noise with prediction of LS model based on I-V curve. The measured I-V curve and dynamic resistance are used in Equation 7.4 for the LS model, with a physical temperature of 4.6 K, equal to the high-voltage limit.

overall scale and bias dependence of the noise are in fairly good agreement, despite the discrepancies seen in the I-V curves. We can also compare the measured noise with that predicted by the LS model, Equation (3.13). In this case, we can use the measured I-V curve and the dynamic resistance, as determined from this I-V curve, to account for some of the variation due to resonances and other structure in the I-V curve. More specifically, the expression to be used for the junction output noise temperature, in Kelvins, is

$$T_J = T_{BATH} \frac{R_d(V)}{R_N} \left[1 + \frac{1}{2} \left(\frac{I_C}{I(V)} \right)^2 \right], \tag{7.4}$$

where $R_d(V)$ is the measured dynamic resistance and $I(V)$ is the measured current, each as a function of bias voltage. Figure 7.7 shows a comparison of this LS model prediction and the measured noise. Again, the agreement is fairly good, and we can see that the LS model is better able to reproduce the voltage variation of the noise than the RSJ model. In particular, some of structure in the noise also appears in the curves of dynamic resistance (not shown), and is then translated into the LS predictions of the noise (for example, the resonance seen at 0.3 mV). The LS model even displays some of the noise asymmetry due the asymmetry in the I-V curve.

If we examine the behavior when the critical current is no longer suppressed with the magnetic field, we see a dramatic increase in the maximum value attained by the junction output noise. The I-V curve can still be fit reasonably well, except for the deviations due to resonant structure. A comparison of an RSJ model I-V curve and a measured curve for an NbN shunted junction is shown in Figure 7.8a. The accompanying plots show the dynamic resistance (b) and the measured junction noise (c) as a function of bias voltage. In this case, we see that the noise attains a maximum value of nearly 400 K. The RSJ model, in which the effects of any frequency dependence of the external circuit have been ignored, underestimates the actual noise by more than an order of magnitude, predicting an excess noise no greater than about 20 K. Also shown is the prediction of the LS model, based on the observed I-V curve. The LS model reproduces the qualitative shape of the noise curve, with several peaks occurring at the regions of dynamic resistance. However, the LS model also

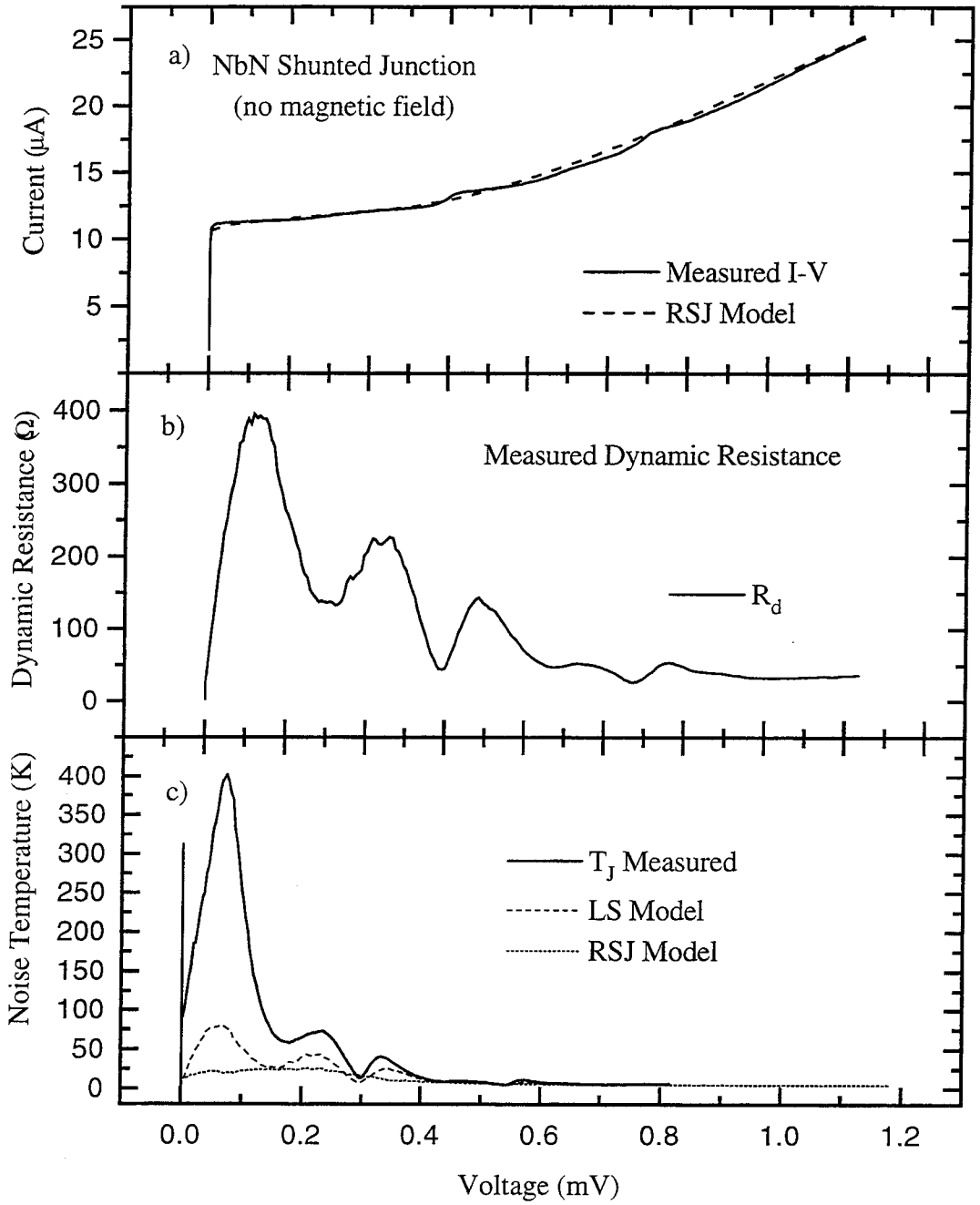

Figure 7.8 Comparison of RSJ and LS model with measured noise for an NbN shunted junction with a large $I_C R_N$ product. **a)** Measured I-V curve (full line) and RSJ model fit (dashed line). **b)** Dynamic resistance as a function of bias voltage, as determined by taking the derivative of the measured I-V curve. **c)** Measured noise temperature (full line) as a function of voltage. Also shown is the noise predicted by the RSJ model (dotted line) and by the LS model (dashed line), using the measured I-V curve and Equation (7.4).

underestimates the severity of the excess noise by about a factor of five. The departures from the RSJ model are not unexpected based on the clear evidence in the I-V curve for the interaction of the junction with the external RF circuit, which cause the variations in the I-V curve. We saw in Chapter 3 that the LS model relies upon the assumption that the high-frequency impedance seen by the junction is not significantly different from the normal-state resistance. When this assumption is violated, the spectrum and amplitude of the excess noise can change. Obviously, the effects of the RF impedance must be included in a proper prediction of the excess noise.

7.4. The Effects of RF Impedance on Noise

Several other experiments which were performed confirm that the cause of the anomalously high noise and the complicated structure of the noise with bias voltage is due to the effects of the RF circuit. First, the structures in the I-V curve occur at voltages in the range from about 0.15 to 0.3 mV. We saw in Chapter 2 that the interaction of a Josephson junction and an external resonance produced a structure in the I-V curve at a voltage where the Josephson oscillation frequency corresponds to the resonant frequency. Thus the range of voltages where structure is observed corresponds to a frequency range from about 75 to 150 GHz. The junctions were fabricated for use in a 115 GHz waveguide mixer mount (described further in Chapter 8), with an integrated choke structure designed to match the 85-140 GHz band of the mount. This choke structure consists of a series of alternating high and low impedance microstrip sections, which are designed to give a low impedance to ground in the waveguide band. When these junctions are suspended across the waveguide, they are effectively connected between the waveguide walls, giving good coupling to the dominant waveguide mode in the desired RF frequency range, but passing the IF to the rest of the system. Several different substrate thicknesses were tested during initial fabrication, and the resonant voltages varied with thickness. Two different resistor geometries and lengths were fabricated, and no systematic variation of the resonances was observed, confirming the analysis (*cf.* Chapter 6 and Appendix A) that these structures should not be strongly frequency dependent. Variations in the resonant structure were seen depending on whether the junction was suspended in

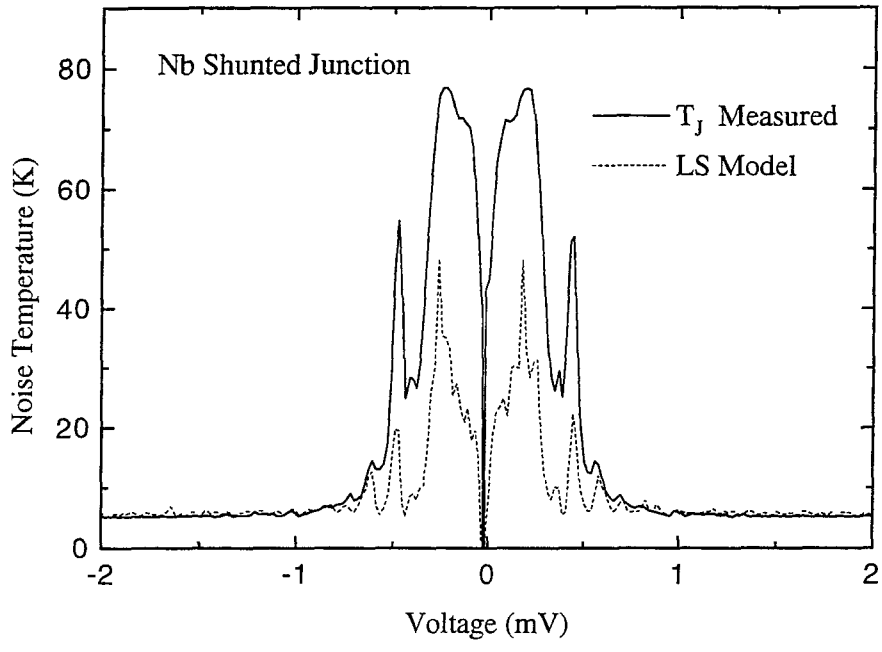

Figure 7.9 Measured junction output noise (full line) and prediction of LS model (dashed line) based on I-V curve. For this large $I_C R_N$ product device, the LS model underestimates the output noise by a factor of several in the region of strong nonlinearity and strong interaction with the external circuit.

the waveguide (so that the first roughly quarter-wavelength section was in free space) or mounted in the noise testing block (over a full ground plane). When junctions were mounted in the waveguide, some very narrow resonances (approximately 0.015 mV) were observed to change position as the settings of the adjustable waveguide tuners were changed. The waveguide resonances are expected to be much narrower band than the choke structure.

The large noise was not associated with an anomalous noise in the NbN junctions. Nb-based shunted junctions had very similar behavior and scale of their excess noise. An I-V curve and noise versus voltage for a Nb junction, when mounted in the waveguide, is shown in Figure 7.9. We see again that the LS model underestimates the noise in the nonlinear region by a factor of several.

For junctions whose $I_C R_N$ product was small, such as the data displayed earlier in Figure 7.3, the junction is well above its $I_C R_N$ voltage when it approaches the resonant frequencies. This means that the nonlinearity and the interaction of the Josephson oscillations (which are now above the critical frequency) with the resonance is less important. Thus we expect the amount of structure

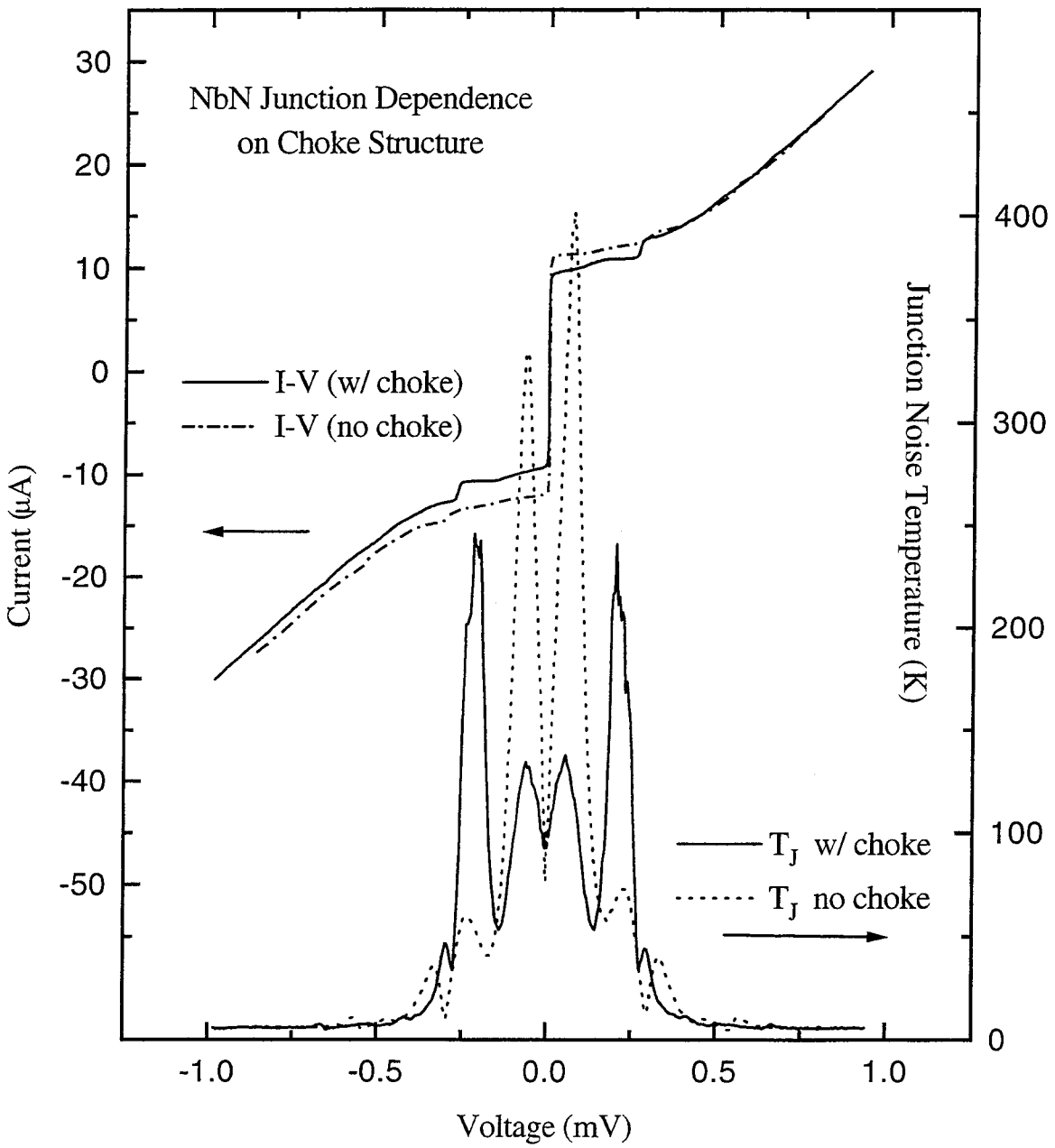

Figure 7.10 Noise and I-V curves of an NbN shunted junction before and after removal of the RF waveguide choke. Full lines show data with choke present, broken lines show behavior on subsequent cooldown after choke was removed. The resonant behavior in the I-V curve (at about 0.2 mV) is less evident after removal, and the structure and amplitude of the noise changes dramatically.

and the deviation from the LS prediction to be smaller for junctions with $I_C R_N$ products less than about 100 μV, as seen for the data in Figure 7.3.

Finally, we were able to measure the noise of a junction both with and without its RF choke. I-V curves and output noise for the same NbN junction on subsequent cooldowns are shown in Figure 7.10. Between cooldowns, the junction had the choke structure cleaved off the chip, leaving only slightly less than the first quarter-wave section to contact the device. We can see that the resonance is less prominent and has moved to higher voltage (and thus higher frequency) as the length of the first section is reduced. Moreover, the structure and size of the noise has been altered simply by the variation in the high-frequency impedance seen by the junction. This is of course an unfortunate circumstance for mixer development, as it is difficult to control the RF impedance over a large range in frequency to prevent any resonances.

7.5. Noise Measurements of Pumped Junctions

We were also able to measure the output noise of a junction with the choke structure removed and with only weak (-30 dB) coupling out of the dewar, through a small hole in the lid of the junction noise measurement fixture. This allowed the application of a local oscillator, fitting of I-V curves under conditions approximating RF current bias, and pumped noise measurements with the junction coupled only to thermal noise at the bath (4.2 K) temperature. The I-V curve for an NbN shunted junction with 86 GHz local oscillator power applied to give about a 50% suppression of the critical current is shown in Figure 7.11. Also shown is an RSJ model I-V curve used to fit this I-V curve, which agrees fairly well. A plot of the measured output noise temperature, T_J, is shown below in Figure 7.12. Here the prediction of the RSJ model for the output noise is unable to account for the observed noise, despite the fact that the junction was only coupled to a 4.2 K bath, with no down-converted noise from outside the dewar. Notice, however, that the measured noise is a much smoother function of the bias voltage, except on the vertical portions of the Shapiro steps, where the IF coupling to the amplifier is small. The noise is significantly less than in the case of no local oscillator applied. In this case, the pumped I-V curve shows only very small traces of the effects

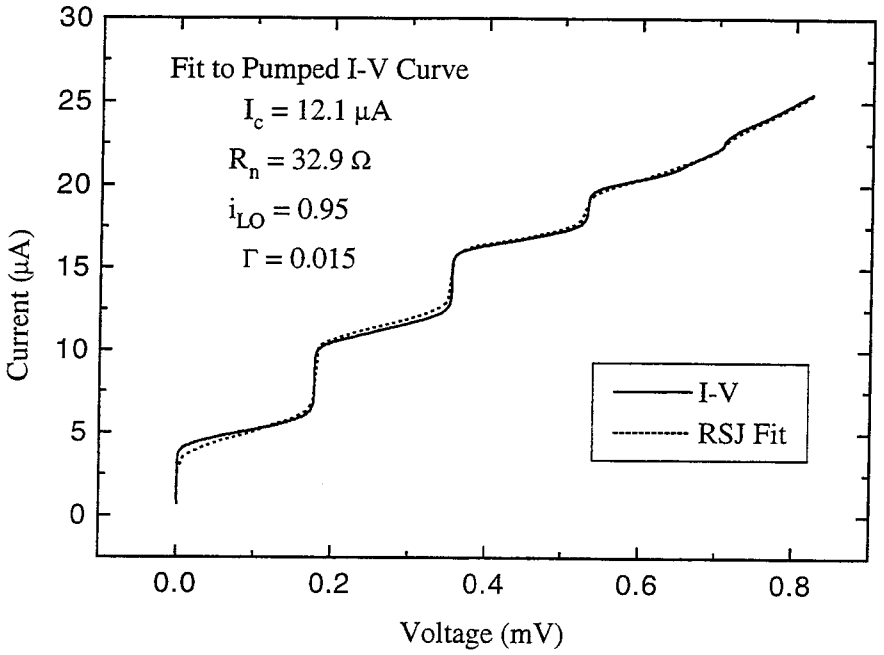

Figure 7.11 Comparison of measured I-V of NbN shunted junction (full line) with 86 GHz local oscillator applied and RSJ model (dashed line). RSJ model parameters were $\beta_C = 1.0$, $\Gamma = 0.015$, $\Omega_{LO} = 0.445$, and $i_{LO} = 0.95$, corresponding to a scaling with a critical current of 12 μA and normal-state resistance of 33 Ohms.

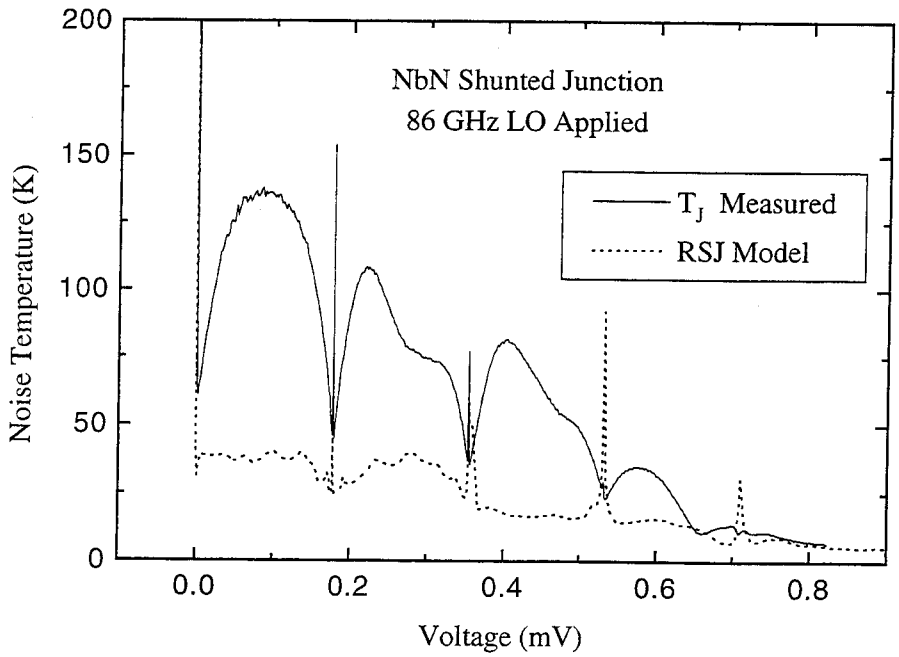

Figure 7.12 Comparison of measured output noise temperature (full line), for the junction shown above, and the RSJ model prediction (dashed line) of noise.

of the RF resonances. Nonetheless, the circuit must still be affecting the junction and causing the discrepancy in the measured and predicted noise.

7.6. Summary

We have presented here calibrated measurements of the low-frequency noise of Josephson devices, both with and without local oscillator applied. The general behavior of this noise is as expected from the RSJ model or the Likharev-Semenov form for the noise of an unpumped junction. In particular, the noise approaches the thermal limit at voltages larger than the critical voltage, $I_C R_N$, where the nonlinearity is not strong. In the region of bias voltage below $I_C R_N$, however, the noise has a much higher than thermal value, due to the excess noise. The measured noise is largest at regions of high dynamic resistance, where the Josephson oscillation linewidth, and therefore the magnitude of the excess noise, should be largest. However, we see significant deviations from the expected dependences on bias voltage, with structures in both the I-V characteristics and the noise as a function of voltage, which are caused by the variation of the RF impedance presented to the junction. As was seen earlier (in Chapter 3), the RF impedance can affect the magnitude of the noise, and both RSJ and LS model would be expected to break down when the impedance deviates strongly from the assumed simple form. As the bias voltage is swept, the junction is sensitive to frequencies from DC to ω_C, which can be hundreds of GHz. This is an unfortunate circumstance, since it is very difficult in practice to prevent resonances in impedance over such a wide range in frequency. This sensitivity to the high-frequency impedance implies that it is difficult to accurately predict the size of the output noise which would be expected. In the next chapter, we will see that the heterodyne sensitivity is degraded due to the elevated output noise of the devices. If one could include the effects of the external circuit into the nonlinear treatment of the junction dynamics, this should improve the prediction of noise levels.

Chapter 8

Heterodyne Receiver Measurements

> *You* may *abuse a tragedy, though you cannot write one. You may scold a carpenter who has made you a bad table, though you cannot make a table. It is not your trade to make tables.*
>
> – Samuel Johnson, *in defense of criticism.*

In this chapter, we will describe heterodyne measurements of Josephson mixers based on resistively-shunted tunnel junctions fabricated with the process described in Chapter 6. These measurements were performed in a waveguide mixer mount with two mechanically adjustable tuners and a scalar feedhorn to couple the local oscillator and signal from outside the helium dewar. All measurements were performed within the approximately 85-120 GHz band of the WR-8 waveguide mount. The mixers tested showed behavior qualitatively in agreement with the RSJ model predictions, although some indications of the influence of the embedding circuit on the junction were observed. The best receiver noise temperature obtained, without corrections for optical losses or IF system contributions, was 190 K (DSB), with about -6 dB of conversion efficiency. This result probably represents one of the best system temperatures achieved with a Josephson receiver, although some earlier works (e.g. Edrich, 1976; Edrich *et al.*, 1977) claimed very low mixer noise temperatures after applying large corrections for estimated mismatches and design imperfections. However, the observed noise temperatures remain a factor of five or more higher than the RSJ predictions, and

the possible causes for the discrepancy will be discussed.

8.1. Previous Experiments with Josephson Mixers

Before describing the experiments performed in this thesis research, however, we will review some of the previous experimental work on heterodyne detection with Josephson devices, which will place this work in context and point out some of the difficulties which need to be avoided. There is a considerable body of previous work on Josephson-effect mixing, although most of this work suffered from a combination of unpredictable devices (*e.g.*, point contacts) and limitations in receiver design. In fact, millimeter-wave mixing (72 GHz) was observed a few years after the discovery of the Shapiro steps (Grimes and Shapiro, 1968). Much of the work performed in this country was done in the laboratories of P.L. Richards at Berkeley. In 1974, this group observed the nonclassical result of large conversion gain ($\eta_C > 1$) in a Nb point contact (Taur, Claassen, and Richards, 1974a). They later inferred a mixer noise temperature of 54 K (SSB) at 36 GHz, which was obtained by measuring the conversion efficiency and output noise separately (Taur, Claassen, and Richards, 1974b). Claassen and Richards (1978b) reported a mixer temperature of of 180 K (SSB), measured with the hot/cold load technique (see, *e.g.*, the description below), although their system temperature was at least a factor of three higher than this. Perhaps the best sensitivity reported at ~100 GHz is that of Taur and Kerr (1978), who obtained a mixer temperature of 120 K (SSB), with 0 dB conversion loss, in a waveguide system based on a Nb point contact. Although they did not report the system temperatures on which this result is based, the receiver did have a 10 dB loss at the RF input due to the stainless-steel waveguide feed. An experiment performed by Edrich (1976) demonstrates some of the difficulties with inferring mixer temperatures based on unoptimized receiver systems. He quoted a mixer noise temperature of 71 K (SSB) for a 47 GHz receiver. However, this mixer was estimated to have ~ 12 dB of conversion loss, and the IF amplifier had a noise temperature of ~ 300 K. This mixer temperature was thus based on an estimation of the mixer's contribution to the reported system temperature of 5600 K (DSB; or 10,000 K SSB!).

A series of experiments were performed at various institutions in the Netherlands over the

period from 1980 to 1987. These experiments used either point contacts or a lithographically-fabricated type of junction consisting of Nb banks with a Si insulating layer, which produced partially hysteretic I-V characteristics without a pronounced gap structure. Daalmans *et al.* (1980) described the device properties and general response to LO radiation, and ter Horst *et al.* (1985) reported receiver temperatures of 1,600 K at 345 GHz with these devices in a waveguide mount. Panhuyzen *et al.* (1987) later obtained improved performance of 1,000 K at the same frequency. Poorter (1982) used Nb point contacts to obtain mixer temperatures of about 200 K (SSB) at 180 GHz based on a waveguide receiver with a system temperature of 1,000 to 2,000 K (SSB). He also examined the frequency response of the system with a Michelson interferometer, and noted that devices with even slight amounts of hysteresis in the I-V curves could display a large nonheterodyne response, *i.e.*, a response to a broadband source which was not close to the LO frequency and did not even require the presence of the LO. Blaney, Cross, and Jones (1982) also observed some nonheterodyne response of their point contact device, which was ameliorated by ensuring a constant-voltage bias for the junction. The nonheterodyne response was always greatest without LO applied to the junction. Nonetheless, they quote a receiver temperature of 2100 K (DSB) at an LO frequency of 450 GHz. One early attempt to use a shunted junction (Gundlach and Kadlec, 1978) to replace the point contact was that of Hartfuß, Gundlach, and Schmidt (1981), who performed experiments at 70 GHz with coherent signals and estimated a mixer noise temperature of 2300 K.

8.2. Heterodyne Receiver Design

The general design of the 3 millimeter (100 GHz) receiver is very similar to that used for astronomical applications with SIS mixers in the millimeter and submillimeter wavebands (*e.g.*, Kooi *et al.*, 1992; Walker, *et al.*, 1992). A schematic of the system is shown in Figure 8.1. The mixer mount is placed in a hybrid cryostat with a closed-cycle refrigerator (CTI-Cryogenics, Model 350, Santa Clara, CA) with one stage at approximately 80 K, and a second stage at approximately 12 K. The mixer is mounted on the coldplate of a liquid helium (4.2 K) pot, within two radiation shields which are cooled by the refrigerator. This arrangement eliminates the need for a second

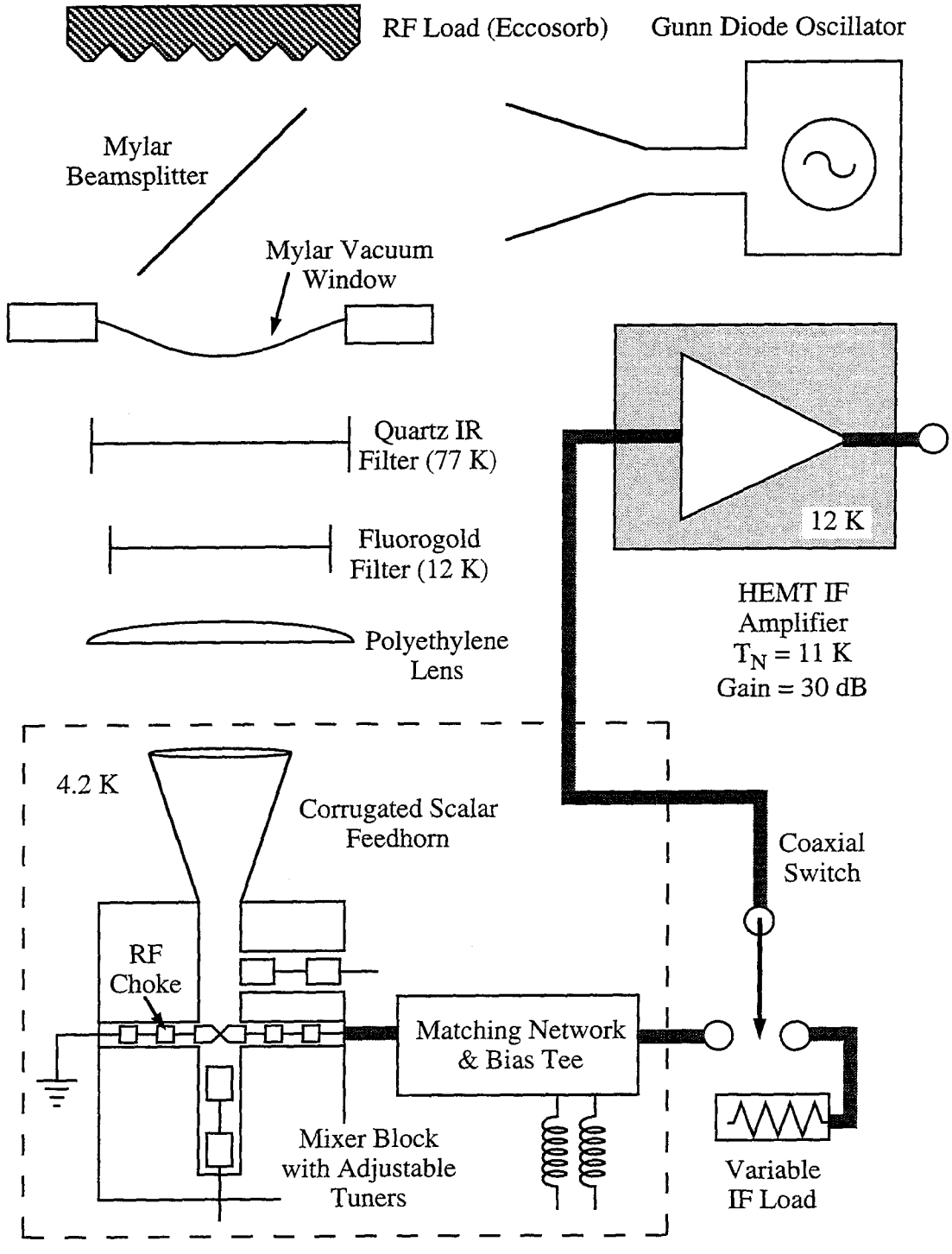

Figure 8.1 Schematic of heterodyne receiver system.

cryogen (usually liquid nitrogen), and allows very long hold times for the helium, since most of the radiative and conductive loads are intercepted by the mechanical refrigerator. This is an advantage for receivers in use at the telescope, but is less important for the laboratory studies described here.

The junction is fabricated on a thin dielectric substrate (100 μm or 0.004 inch thick quartz) with an integrated microstrip choke structure which is mounted across the center of the full-height (0.040 by 0.080 inch; 1 by 2 mm) waveguide in the E-plane direction. The choke structures serves as an RF short to connect the junction to the waveguide walls in band and couple to the TE_{10} mode of the waveguide. There is a rectangular to circular waveguide transition, and a corrugated scalar feedhorn with a directivity of approximately 25 dB. A polyethylene lens is mounted in front of the aperture of the horn to produce a narrower beam. The beam then exits the dewar through cooled IR filters of fluorogold (Fluorogold S-tape, Fluorocarbon, Inc., Anaheim, CA) and black polyethylene on the 12 K radiation shield and quartz and black polyethylene at 77 K. Finally, a 25 μm (0.001 inch) thick mylar sheet serves as the vacuum window. Both IR filters are selected to be one half-wavelength in the dielectric in order to have maximum in-band transmission. The window apertures are approximately one inch in diameter, which corresponds to a better than -30 dB edge taper (*i.e.*, less than 0.1 % spillover of the beam) at each stage. Fresnel (reflection) losses of approximately 5% are expected at the dielectric interfaces of the polyethylene (ϵ_r = 2.4 and index of refraction, n, of 1.55) lens. The overall losses in the optics should be less than 15%. However, since some of these losses (*e.g.*, the vacuum window) are at room temperature, they can add to the observed receiver temperature. Experience with similar systems using SIS mixers (J. Kooi, private communication) has indicated that these losses may contribute roughly 30 K to the DSB mixer temperature.

The local oscillator is injected via a 25 μm (0.001 inch) mylar beamsplitter, whose reflectivity is less than 1% at these wavelengths. For noise measurements, an absorbing load was used which filled the beam. The beam pattern of the complete system was also measured using a chopped hot load which could be moved on an X-Y stage in front of the dewar. The IF output as a function of the load position could then be used to determine the extent of the receiver beam pattern. A surface plot of the receiver response as a function of linear displacement in the plane approximately

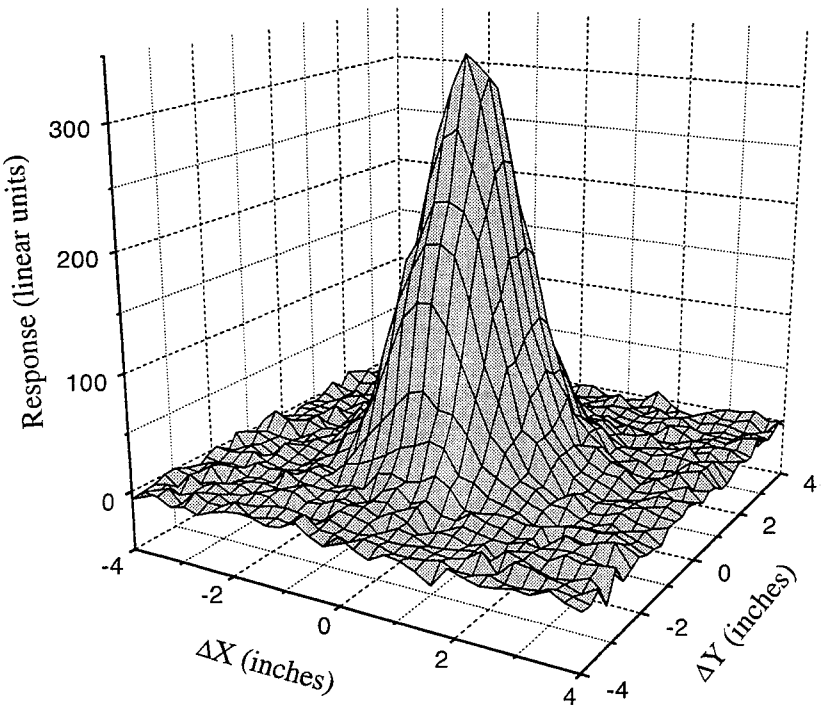

Figure 8.2 Plot of receiver response to a heated load versus linear displacement in a plane approximately one foot in front of the dewar. The beam is approximately gaussian, and corresponds to an f-number of about 5.8.

one foot in front of the dewar is shown in Figure 8.2. This yields a beam divergence half-angle (at the e^{-1} point in power) of about 5 degrees, corresponding to an f-number of 5.8, slightly higher than expected. This confirms that losses due to beam spillover on the windows should be negligible. The beam is highly gaussian, as expected given the many measurements using this type of scalar feedhorn.

As mentioned previously, the mixer mount has two mechanically adjustable tuners which consist of non-contacting backshorts. This particular type of mount has been used extensively for SIS mixers, where the tuners can be used to compensate for the parasitic capacitance of the junction. The mount was previously studied with electromagnetic simulations and scale modeling (Büttgenbach, Groesbeck, and Ellison, 1990), and a wide range of impedances covering nearly the entire Smith chart can be presented to the junction through variation of the tuner positions. An

IF system, described in the preceding chapter, was connected to the mixer output, and allowed an accurate separation of the IF and mixer contributions to the overall receiver performance. An integrated bias-tee and matching circuit was used which provided a better than 90% coupling to the junction at the intermediate frequency for typical mixer conditions. A superconducting solenoid allowed the introduction of a magnetic field, which was capable of suppressing the junction critical current and allowed variation of the $I_C R_N$ product.

8.3. General Response to LO Illumination

The local oscillator was combined with the signal beam through the partially reflecting mylar beamsplitter, and was provided by a Gunn diode oscillator (J.E. Carlstrom Co., Pasadena, CA) which covered the full waveguide band. This oscillator provided typically 20 mW of power, far in excess of that required to pump the mixer. More than 30 dB of attenuation, in addition to the beamsplitter efficiency of less than 1%, was required to produce an LO of the desired strength. Upon illumination with LO, the shunted junction I-V curve displayed strong Shapiro steps, with vertical current steps at the quantized voltages, $V_N = n\frac{h\nu}{2e}$. For strong LO pumping, several (> 5) of these steps could be seen, and the critical current displayed a full modulation, *i.e.*, it could be fully suppressed with the application of the correct amount of local oscillator power.

For one of the Nb shunted junctions from the first fabrication run, the variation of the Shapiro step height as a function of LO power was studied by varying the LO signal strength through a 100 GHz calibrated attenuator. The step heights were determined by the current value displayed at a small, constant voltage above or below the step itself. The amplitudes of the zeroth (*i.e.*, the critical current) and first Shapiro steps are shown in Figure 8.3. The horizontal axis is in units of normalized LO voltage, $\alpha = 2eV_{LO}/h\nu$, obtained by converting the attenuation value to a relative voltage and scaling the result to coincide with the first minimum of the critical current. The lines show the simple Bessel function dependence on LO voltage expected from an RF voltage biased condition (see Section 2.4C). We can see that for this junction, the amplitudes agree well with this functional form. The coupled LO power required to pump the junction is that which gives $\alpha \sim 1$,

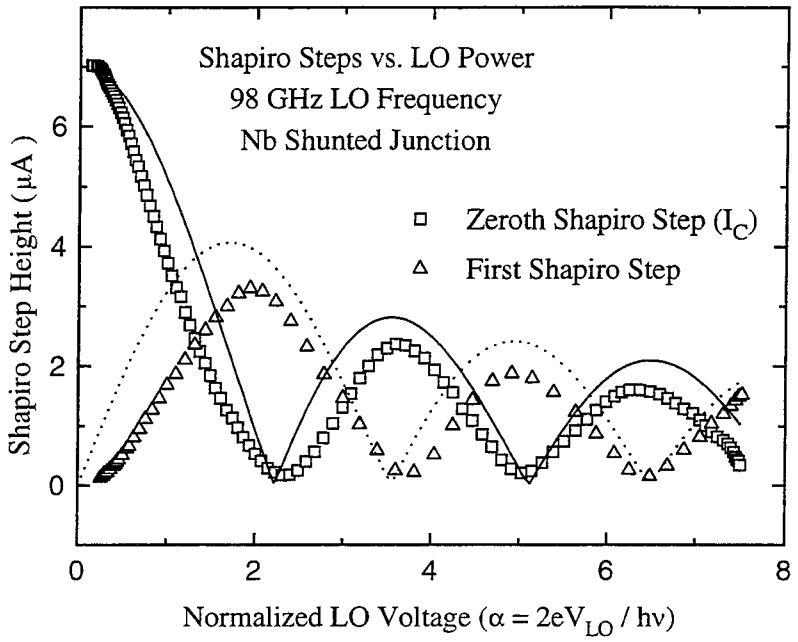

Figure 8.3 Plot of experimentally observed Shapiro step heights as a function of normalized LO voltage, α, in a Nb shunted junction at a 98 GHz LO frequency. Both the zeroth (critical current, squares) and first Shapiro steps (triangles) are shown. The lines show the behavior expected from the simple RF voltage-bias model for the heights, $I_C\,|J_0(\alpha)|$ (solid line) and $I_C\,|J_1(\alpha)|$ (dotted line).

or roughly one nanowatt.

8.4. Receiver Measurement Techniques

Receiver sensitivity was determined using the hot-cold load method commonly used for mixer measurements. In the millimeter frequency range, the power from a thermal load at typical temperatures can be estimated accurately using the Rayleigh-Jeans approximation to the blackbody spectrum, giving a power, directly proportional to the temperature, of k_BT per unit bandwidth. In the hot-cold technique, the receiver is coupled to two loads at known temperatures. The ratio of the receiver output power when viewing these loads is known as the Y-factor, $Y = P_{HOT}/P_{COLD}$. The receiver noise temperature (*cf.* Chapter 1 and the discussion of heterodyne systems) is a measure of the noise added by the heterodyne system, and is defined to be the temperature of a matched load which will exactly double the receiver's output power with no load present. This method is

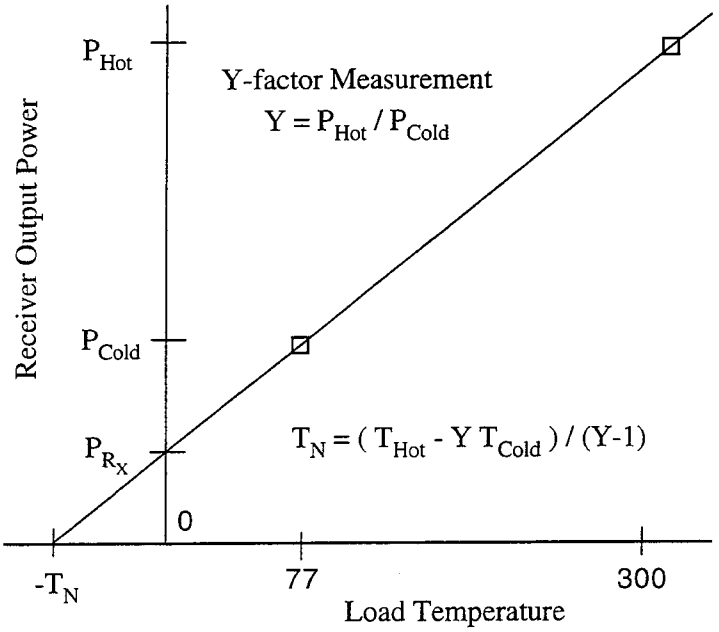

Figure 8.4 Depiction of Y-factor noise measurement technique. Drawing a straight line through the two measurements allows the determination of the output power of the receiver for a hypothetical zero Kelvin load, and the x-axis intercept gives the receiver noise temperature, T_N.

displayed graphically in Figure 8.4. More explicitly, the receiver noise temperature is defined as

$$T_N = \frac{T_{HOT} - YT_{COLD}}{Y - 1}, \tag{8.1}$$

where T_{HOT} and T_{COLD} are the load temperatures used. Since the blackbody loads are broadband, signal will typically be coupled from both upper and lower sidebands, so the noise temperature obtained is the double-sideband (DSB) temperature. Any two temperatures can be used for the loads, but most commonly room-temperature (300 K) and liquid nitrogen (77 K) are used for convenience. In all of the mixer measurements reported here, multi-mode loads consisting of sheets of Eccosorb (Eccosorb AN-72, Emerson and Cummings) were used which filled the entire receiver beam outside of the cryostat. These sheets can be saturated with liquid nitrogen to provide the cold input temperature. The reason for use of blackbody, broadband sources in receiver calibration is the difficulty of obtaining known signal strengths at these frequencies. These broadband sources have several disadvantages, however, since their large total (*i.e.*, integrated over a wide frequency range)

power can cause saturation. Also, if the receiver has non-heterodyne or out-of-band response, this can confuse the measurements, possibly leading to artificially low estimates of the noise temperature. The blackbody technique has proven reliable in the case of SIS mixers, where system temperatures in actual radio-astronomical observations are in good agreement with those estimated via blackbody Y-factor measurements. Josephson mixers with wide-band RF coupling have been seen to have significant problems of direct-detection (Blaney, Cross, and Jones, 1982; Grossman and Vale, 1994), so this is a potential concern. However, several characteristics of the waveguide receivers, which will be described later in this chapter, confirm that the observed response was predominantly heterodyne.

One alternative to the blackbody technique is the use of a gas cell containing a molecule with a transition in the desired frequency range. If a nitrogen-cooled load is placed behind the cell, and if the optical depth of the cell at the center of the transition is large, then this produces an input spectrum of a 77 K background with an emission line equal to room temperature. This technique in principle allows a solely heterodyne measurement of receiver sensitivity, and has been used with high-frequency SIS receivers (*e.g.*, de Lange, 1994; Honingh *et al.*, 1991; Little *et al.*, 1992). However, at 100 GHz it is difficult to obtain large enough optical depth because the low-lying levels of most molecules are not sufficiently populated. A larger path length through the gas could correct this deficiency, but requires additional complications with the optics to handle the broad, diverging receiver beam.

Receiver Y-factors were measured by recording the total power in the IF amplifier's output band (typically 500 MHz). Measurements were occasionally made with a spectrum analyzer, however, and showed little variation with frequency in this band. The Y-factor technique can be used to estimate the mixer's conversion efficiency (*i.e.*, the gain of the first stage of the system), provided that the gain of the IF system is known. In initial measurements, a simplified IF system was used which did not allow direct calibration. In this case, the variation of the junction shot noise, commonly performed with SIS mixers (Woody, Miller, and Wengler, 1985), was used. For the shunted junctions used here, however, a correction for the amount of current flowing thorough the shunt resistor was required (*cf.* discussion in Section 7.2). Later experiments were performed with the

more capable IF system described in Chapter 7, which permitted accurate calibration of IF noise and gain, and the measurement of IF matching at the mixer operation point. In this case, a good separation of the mixer and IF system contributions to the total noise could be made.

8.5. Initial Nb Mixer Results

The first Josephson mixer results were obtained with Nb shunted junctions which were not optimized in several respects. First, the junctions were fairly low-current density and overshunted, which lead to reduced $I_C R_N$ products of about 0.2 mV. This implied that the normalized LO frequencies studied were roughly one, rather than the optimal value of about a half suggested by the RSJ modeling. Secondly, they were fabricated on 200 μm (or 0.008 inch) thick quartz substrates, which were twice the designed (100 μm or 0.004 inch) thickness. The thicker substrates reduced the performance of the RF choke structure and possibly degraded the coupling between waveguide and junction. A preliminary set of unshunted SIS junctions (also on thick substrates) were studied in this mixer mount, and showed a reduced effectiveness for the waveguide tuners, which could not entirely compensate for the junction capacitance. These devices gave receiver noise temperatures of about 80 K (DSB), despite a substantial IF mismatch due to the small area and low current density (3,000 A/cm^2). This verified that the receiver design was not severely flawed.

When the Josephson devices were mounted and illuminated with LO, strong hot/cold response was immediately evident. A plot of the unpumped and pumped I-V curves, and the IF output power as a function of bias voltage, for a 300 K and liquid nitrogen load at the receiver input, is shown in Figure 8.5. The first Shapiro step at $V = h\nu/2e \sim 0.2$ mV is visible in the pumped I-V curve, and the small feature at roughly 0.33 mV in the unpumped curve results from a resonance of the RF choke structure. The best receiver performance was always seen for LO power levels that resulted in a roughly 50% suppression of the critical current. Tuning with the adjustable waveguide backshorts was reproducible, and optimum performance was seen for positions which maximized the total IF output power. These tuner configurations also gave a nearly optimal coupling of LO power to the device. Operation on the riser between the first and second Shapiro steps, as well as operation for

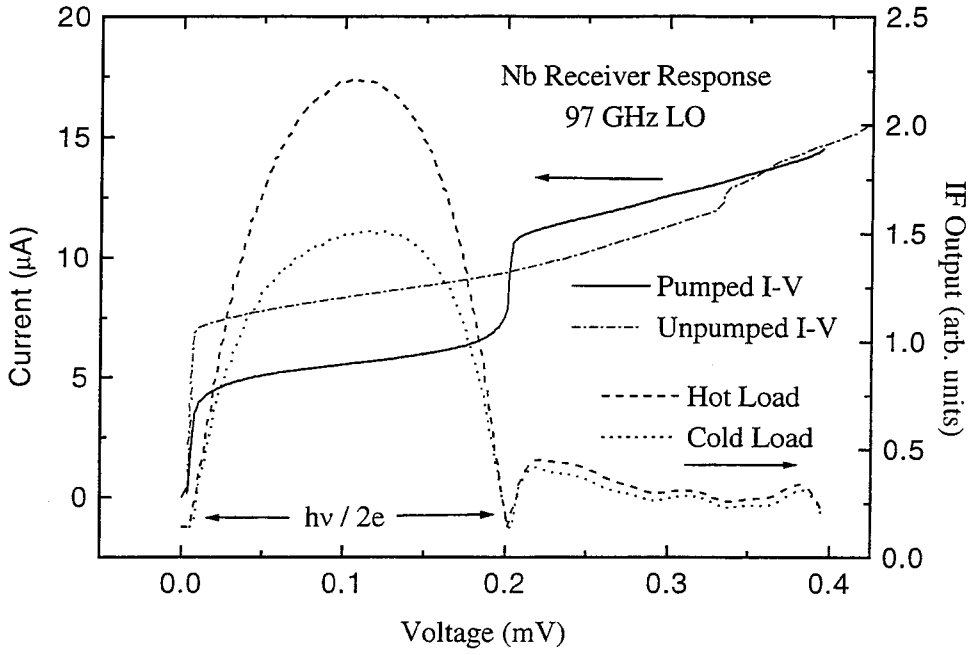

Figure 8.5 Receiver hot/cold response and I-V curves for initial Nb shunted junction mixer. Full line is pumped I-V curve, dash-dotted line shows unpumped I-V. Dashed line is IF output power with a room-temperature load at the receiver input, dotted line is for 77 K load.

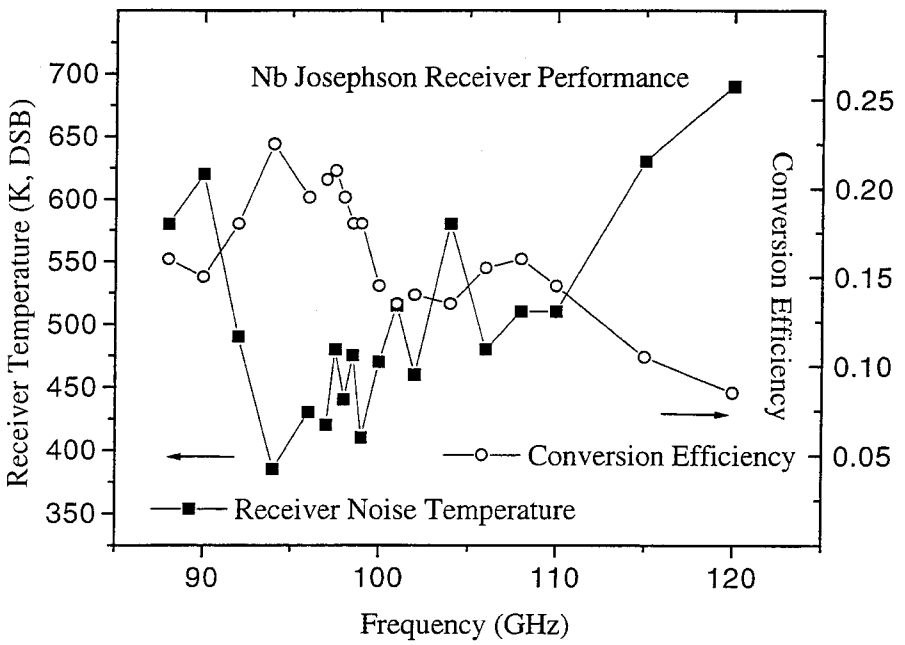

Figure 8.6 Plot of receiver temperature (squares) and conversion efficiency (open circles) for several different LO frequencies across the waveguide band.

LO powers higher than that producing the first minimum of the critical current, was possible, but yielded degraded noise temperatures. No dependence of the I-V curve itself on RF load temperature was seen. Likewise, no variation in output power was seen without LO power applied, ruling out direct detection as a cause of the hot/cold response. Finally, a shift in LO frequency required a change in tuner position to reoptimize receiver response. These tuning shifts were of the direction and magnitude consistent with maintaining the same electrical length for the tuning sections. In other words, the RF impedance at the LO frequency was important in determining the strength of the hot/cold response. This suggests that the observed response was in fact due to power coupled to the device at frequencies very near the LO frequency. Thus it is believed that the observed hot/cold response is in fact completely due to true heterodyne detection.

Based on the difference in the hot/cold output powers seen in Figure 8.5, we obtain a best Y-factor of 1.46, or a receiver noise temperature of 390 K (DSB). Shot-noise calibration of the IF system yields a value for the conversion efficiency of the mixer of about 0.23, or -6.5 dB. This in turn yields an estimate of the mixer noise of about 340 K (DSB). The shape of the pumped I-V curve is quite similar to that predicted by the current-biased RSJ model. The IF output power is a maximum in the center of the first "riser," as is the conversion efficiency, in accordance with expectations from the RSJ model (*cf.* Figure 4.7). The lowest noise temperatures are seen at a bias point just slightly below the center of the riser, also in accordance with the modeling described in Chapter 4 (*cf.* Figure 4.10). The receiver temperature for several different frequencies across the waveguide band, with the LO power and tuning reoptimized for each setting, is shown in Figure 8.6. We can see that the response varies about 50% across the band.

8.6. NbN Josephson Mixer Results

The second set of junctions to be measured in the receiver were shunted NbN devices. These junctions were fabricated on the correct 100 μm (0.004 inch) thick quartz substrates to allow optimum performance of the RF choke structure, and the devices themselves had larger $I_C R_N$ products, approaching 400 μV, which should allow for nearly optimum mixer performance at 100 GHz.

The noise performance of these devices was indeed superior to that of the initial Nb devices. A hot/cold response of the receiver is shown in Figure 8.7. The best receiver response was again found in the center of the riser, and Y-factors as large as 1.6 were observed, corresponding to a noise temperature of about 270 K (DSB). Conversion efficiency remained about -6 dB, suggesting a mixer noise temperature of roughly 220 K (DSB). Notice, however, that the shape of the I-V curve and the IF power curves are quite different from those seen earlier with the first Nb devices.

The effects of the mechanical tuners were more pronounced for these devices, and the dynamic resistance on the riser between photon steps varied dramatically for different tuner configurations. In fact, after the bias circuitry was modified to give a very low impedance load line for the voltage biasing, negative differential resistance could be seen for some conditions. Several pumped I-V curves for different tuner settings, all for the same LO frequency of 98 GHz, are shown in Figure 8.8. These curves are very similar to those calculated by Taur (1980), using an RF voltage balance method to solve the RSJ model (*cf.* the discussion in Section 4.5) with a finite impedance LO source. The dashed curve, with low differential resistance, is similar to that calculated for a capacitive LO impedance, while the dotted curve resembles the case of a real (or infinite impedance, in the RF current-biased case) drive impedance. The solid curve, showing negative differential resistance, corresponds to the case of an inductive driving impedance. Both of the extreme observed cases of differential resistance corresponded to tuner positions very far from LO power match, and the LO power had to be increased significantly to give the same degree of critical current suppression. For the case of negative differential resistance, conversion gain (or efficiencies greater than one) might be possible. However, relatively poor receiver performance was found in this case, probably due to the large RF mismatch.

For these devices, the RF impedance of the mixer mount is clearly exerting a strong influence on the dynamics and behavior of the device. This strong interaction of the nonlinear device and the embedding circuit is probably the origin of "double-humped" shape of the IF power curves shown in Figure 8.7. In fact, RSJ simulations performed with a resonant circuit (a series "R-L-C") in parallel with the junction at the RF frequency were able to reproduce this shape qualitatively. Although

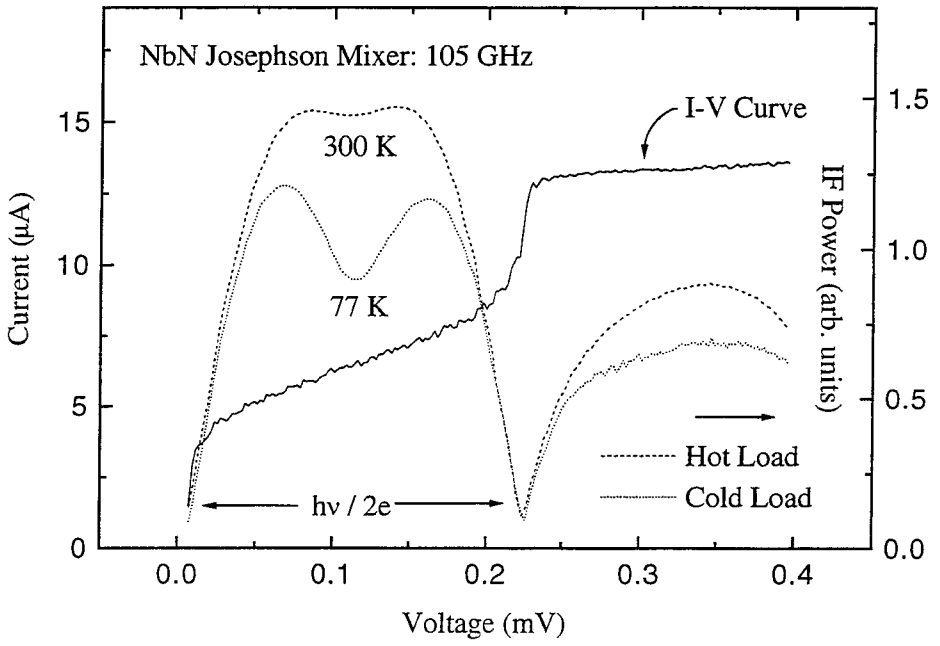

Figure 8.7 NbN receiver response to hot/cold load. Solid line shows pumped I-V curve, dashed line is IF output with a room temperature RF load at the receiver input, and dotted line is for a 77 K load.

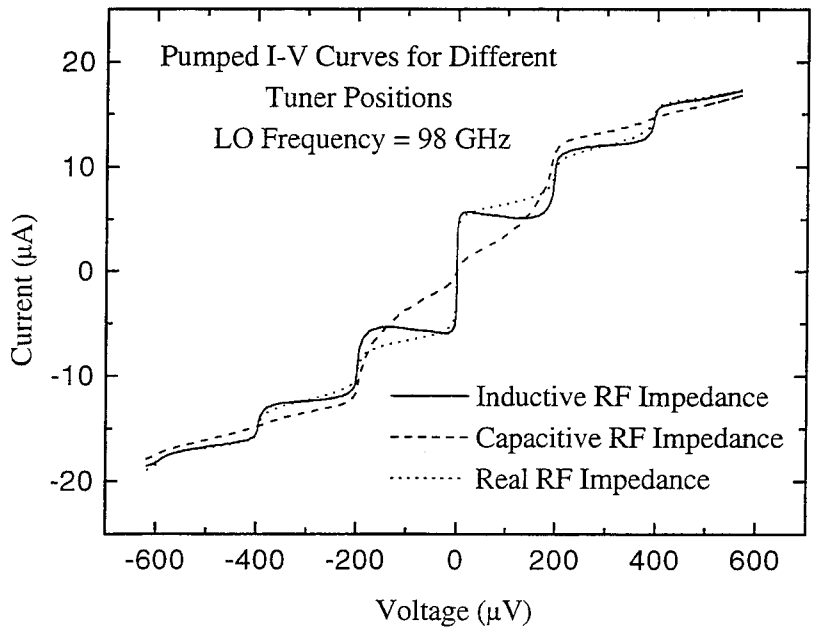

Figure 8.8 Variation of pumped I-V curves and dynamic impedance with different waveguide tuner positions. The three curves were all taken with 98 GHz LO applied, and the power level adjusted to give roughly the same degree of suppression of the critical current.

receiver sensitivities superior to the first Nb devices were obtained, the RF current-biased RSJ model would predict that mixer noise temperatures nearly a factor of five lower should be attainable. Since these devices, based on their DC characteristics (resistance, $I_C R_N$ product) should be nearly optimal, we can compare with the RSJ mixer simulations shown in Figure 4.8. These simulations predict (converting from normalized, single-sideband units to dimensioned, double-sideband temperatures and assuming operation at 4.2 K) that mixer noise temperatures approaching 40 K (DSB) should be possible with these junctions. Thus the noise of these mixers remains a factor of about five higher than predicted. SIS mixer measurements at 200 GHz with NbN junctions (McGrath *et al.*, 1991; Stern, 1991) have shown slightly higher than expected noise, which could perhaps be due to an intrinsic property or RF loss of the superconductor. It is more likely that in our case the degradation of performance is caused by the strong interaction of the junction with the embedding circuit. In the previous chapter, we saw that the output noise could be much larger than that predicted by the RSJ model in the unpumped case due to this effect.

8.7. Further Nb Mixer Results

A further run of Nb shunted junctions was undertaken to ensure that the observed nonideal mixer results were not due to a materials defect. These devices were made with a refined mask design that reduced the parasitic capacitance due to the counterelectrode contact to the junction, and were nearly optimally shunted to give nonhysteretic I-V curves. These devices were also fabricated on thinner (0.004 inch or 100 μm thick) quartz substrates, to allow proper performance of the RF choke structure. When mounted in the waveguide, these devices behaved quite similarly to the NbN junctions described above. The effect of the tuners was much more pronounced than with the initial Nb devices, due to the better performance of the RF choke structure. Negative differential resistance could be observed for particular tuning positions. The heterodyne sensitivity was also significantly improved, with receiver noise temperatures of slightly less than 200 K (DSB) being obtained in the best case. A plot of the Nb mixer's response to a hot and cold load is shown in Figure 8.9. We can see that the shape of the pumped I-V curve is quite similar to that of the NbN mixers (*cf.* Figure 8.7).

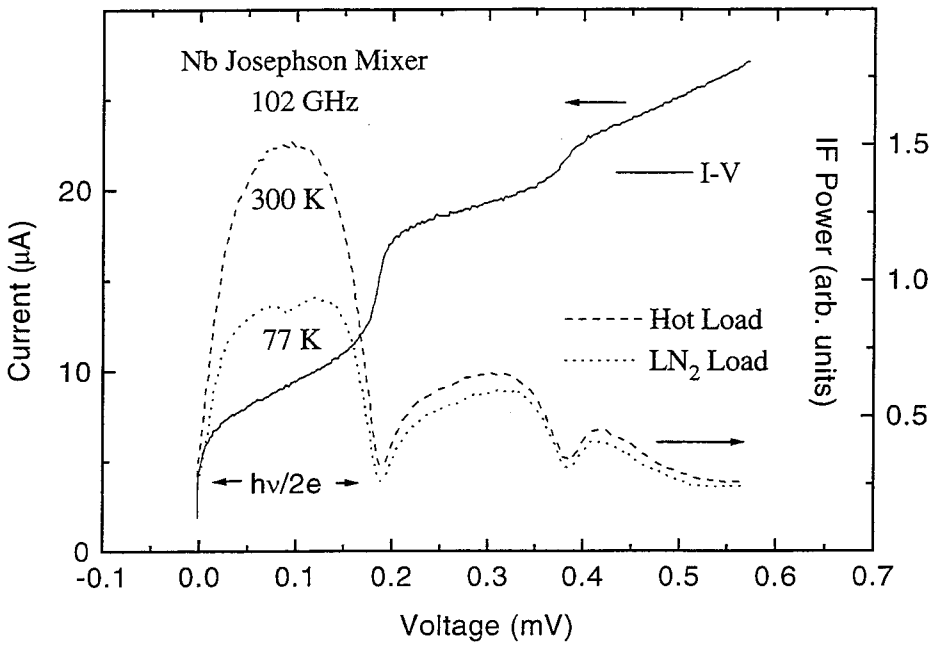

Figure 8.9 Plot of receiver response to a hot/cold load for a Josephson mixer using an optimized Nb shunted junction from the second fabrication run. The pumped I-V curve (full line) and IF output power for room temperature (dashed line) and liquid nitrogen (dotted line) loads at the input are shown. The best receiver response had a Y-factor of 1.82, corresponding to a system temperature of about 190 K (DSB).

The shape of the IF output power curves is also similar, showing the "double-humped" behavior, although it is somewhat less pronounced. The best conversion is attained in the middle of the riser, in the center of the dip, and corresponds to a conversion loss of -6.5 dB. The mixer temperature implied is thus about 150 K (DSB). Since these Nb devices are quite similar to the NbN devices in terms of $I_C R_N$ product and normal-state resistance, we would also expect an optimal performance of about 40 K (DSB), with a conversion efficiency approaching unity, based on the RSJ model.

8.8. Investigation of Nonideal Behavior of Mixers

Some attempts were made to further characterize the Josephson mixers described above, to determine whether saturation or single-sideband operation might be contributing to the degraded performance of the system. As mentioned earlier, the possibility of saturation is a concern when using broadband signals to calibrate a sensitive receiver. As a crude check of the linearity of the

system, loads at several different temperatures can be used. There is, however, some difficulty in obtaining high return loss loads at these frequencies whose temperatures are accurately known. The Eccosorb loads at room temperature and when saturated with liquid nitrogen are well-known, hence their use for calibration. We investigated some of the mixers described above using these two temperatures, as well as a slab of Eccosorb held between blocks of dry ice (solid CO_2; sublimation temperature of 295 K) until briefly removed and placed in front of the dewar. An additional load consisting of a machined ceramic absorber was heated to a temperature of 350 K. Any errors in the temperatures of these loads would most likely be in a warmer than expected dry ice load and a cooler heated load (due to thermal gradients between the backside heaters and frontside absorber). These errors would tend to exaggerate the estimates of saturation. A plot of receiver (IF) output power versus input power (*i.e.*, RF load temperature) is shown in Figure 8.10. The triangles show data taken when the mixer is tuned for best noise performance (*i.e.*, best conversion efficiency), and the circles are taken when the mixer was tuned for negative differential resistance on the riser between Shapiro steps. Also shown are two quadratic fits to these data. The data indicate that in the case of best performance, the receiver may be as much as 30% saturated for a room-temperature load. In the case of negative resistance, the saturation is about 15%, probably due to the lower coupled conversion efficiency.

A fairly simple picture gives some intuition regarding saturation of both SIS and Josephson-effect mixers. In both cases, the mixer gain (conversion efficiency) varies across the photon step, generally peaking in the center. If the down-converted signal strength is large enough, it will cause the bias voltage to swing over some fraction of this step, thereby sampling regions of lower gain near the edges. For SIS mixers, Tucker and Feldman (1985) suggest that this condition can be stated as

$$P_{SAT} = \frac{(f\, h\nu/e)^2}{2\eta_C R_d}, \tag{8.2}$$

where $h\nu/e$ is the width of the photon step, f is the fraction of the step over which the gain varies significantly, η_C is the conversion efficiency, and R_d is the dynamic resistance at the operating point, and thus the IF output impedance. Tucker and Feldman suggest a value for f of about 0.1, leading

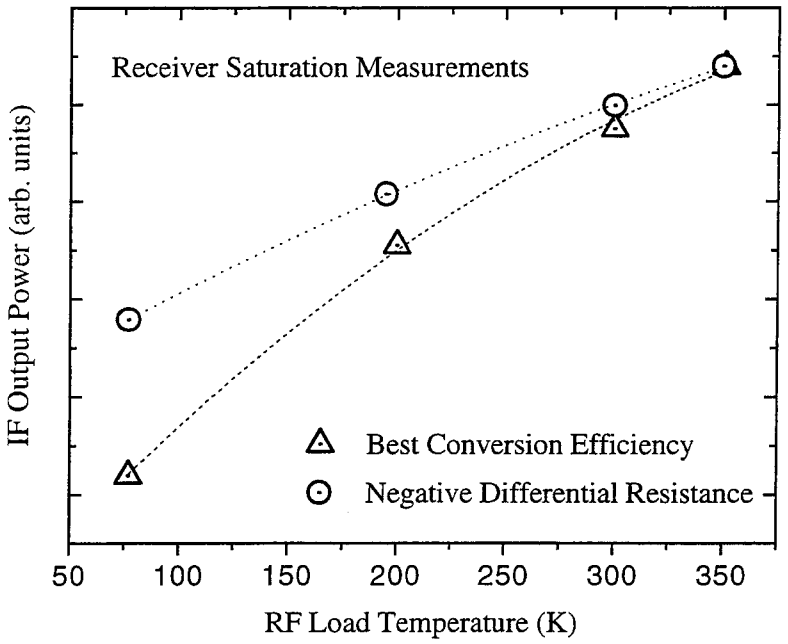

Figure 8.10 Receiver output power versus input RF load temperature (*i.e.*, input power). Both the case when the mixer is tuned for optimum performance (lowest noise, triangles) and the case where the mixer is tuned for negative differential resistance (circles) are shown. The lines are quadratic fits to the data. From these fits, we estimate that the mixer is saturated for a room temperature load by about 30% (triangles) and 15% (circles).

to a saturation power of 8 picowatts for an SIS mixer at 100 GHz, with a conversion efficiency of unity and an output impedance of 100 Ω. This power is equal to that from a room temperature load in a bandwidth of 2 GHz, which could easily be attained. Experience with low-loss SIS mixers at 100 GHz (D. Woody, private communication) shows that 10-20% saturation is in fact seen in these devices.

Based on the argument above, we might expect that saturation in Josephson mixers would be as much as a factor of four higher, due to the photon step size of $h\nu/2e$. For the Josephson receivers discussed above, however, the best conversion efficiency remains about -6 dB, so we might expect a saturation effect comparable to that observed in SIS mixers. Note that for the case of very large (or negative!) differential resistance, the saturation should be more severe. In the case shown above, however, the conversion gain decreases substantially, thus offsetting the increased

output impedance. The presence of saturation means that the receiver noise has been slightly (20%) overestimated, and the conversion efficiency may be about 1 dB higher than inferred from room temperature and nitrogen hot/cold measurements. However, the saturation is not overly large, and has not drastically affected the noise temperatures estimated from the hot/cold method. Note that the saturation power is expected to increase as the square of the LO frequency, and thus this saturation will not be too great a problem at submillimeter frequencies.

Another assumption made in interpreting the hot/cold receiver measurements is that the receiver is double-sideband, or equally sensitive to both the upper and lower sidebands of the LO. This would seem reasonable given that the 3 GHz offset (twice the intermediate frequency of 1.5 GHz) is small compared to the LO frequency of 100 GHz. The waveguide mount and its tuners are highly resonant, however, so that there could be significant impedance variation with frequency. One can measure the instantaneous bandwidth of the receiver in order to determine if this frequency variation is significant. In this measurement, the receiver is first tuned and optimized at a particular frequency. Then the LO frequency is shifted, and the mixer reoptimized without altering the positions of the mechanical tuners (*i.e.*, LO power and bias voltage can be adjusted). Mixer noise can then be measured at several shifted frequencies. When performed for these Josephson-effect mixers, the noise increases roughly linearly with the change in frequency in either direction, and has roughly doubled after a shift of 3-4 GHz in either direction. This suggests that the frequency variation is indeed significant, and that the receiver may be operating in a predominantly single-sideband mode. This would imply that the receiver noise temperatures reported are in fact really single-sideband, and would bring the experiments closer to agreement with the RSJ predictions. Single-sideband operation is not particularly undesirable for astronomical observations, where one typically observes a desired line which is present in only one sideband. However, a less resonant RF circuit might improve the mixer performance.

8.9. Discussion

We can take some of these nonideal effects into account in order to make a comparison with the

RSJ mixer predictions. Furthermore, the effects of the losses in the dewar optics should be subtracted from the mixer noise temperatures. For the best Nb receiver, assuming a 20% overestimate of the noise due to saturation by the hot load, and assuming about 20 K due to optics losses, we obtain a corrected mixer temperature of about 90 K (DSB). Based on the RSJ model calculations shown in Figure 4.8, we would expect a mixer temperature for this nearly optimal device of 20 times the physical temperature (SSB) of 4.2 K. We then need to divide by two to obtain the double-sideband temperature of 45 K (DSB). Thus, after these admittedly uncertain corrections to the measured sensitivity are made, one might claim agreement with RSJ predictions to within a factor of two. If in fact the mixer was largely single-sideband, this would improve the agreement. To truly make a good comparison of the theoretical predictions with experiment, one should carry out the RSJ modeling with the actual RF embedding impedances included in the nonlinear part of the problem. For the waveguide mount, the actual frequency dependence is complicated and, of course, depends on the position and quality of the adjustable tuners. A quasioptical coupling scheme which provides a real impedance to the junction over a broad frequency range (*e.g.*, a log-spiral antenna, see Büttgenbach *et al.*, 1988) would allow a better comparison. However, the increased potential for saturation would be a concern, given the broad-band RF coupling.

We have described the results of several series of heterodyne receiver tests made in a waveguide system at 100 GHz using resistively-shunted tunnel junctions as the Josephson mixing elements. The general behavior of the pumped I-V curves and the mixer optimization with bias voltage and LO power was similar to that expected from the current-biased RSJ model simulations described in Chapter 4. The effects of the finite RF driving impedance could be seen in the change of differential resistance with tuning positions and the shape of the IF power curves. Improvements in the RF coupling and optimization of the junction parameters, particularly the $I_C R_N$ product, were seen to improve receiver sensitivity. Nonetheless, the receivers had lower sensitivity than predicted by the RSJ model. Although some saturation and evidence of unequal sideband ratios was seen, the reduced sensitivity is probably due to higher than expected values for the mixer output noise. As was seen in Chapter 7, the details of the RF embedding circuit can alter the magnitude and character of this

noise. Thus the discrepancy between the experimental results and the RSJ simulations is probably due to the breakdown of the RF current-biased assumption. An inclusion of the RF embedding circuit into the nonlinear RSJ modeling is therefore required to make a more detailed comparison with experiment.

Chapter 9

Summary

I have made this letter longer than usual, because I lack the time to make it short.

– Pascal, *Lettres provinciales*

At this point, a brief review of the material presented in this thesis is desirable. A brief introduction to the Josephson effect and the RSJ model was provided in Chapter 2, and some of the important dynamics were described, including the AC Josephson oscillations, the effects of device capacitance on I-V curves and hysteresis, and the appearance of the Shapiro steps due to photon-assisted tunneling of the Cooper pairs. We also discussed the inclusion of fluctuations into the RSJ formalism, and gave a rough outline of the numerical method used for the solution of the RSJ model. A unfortunate drawback of the RSJ model is its assumption of an ideal current bias at all frequencies. It is possible to include the effects of an antenna or other coupling structure into the nonlinear solution of the RSJ equation, if a simple, lumped-element equivalent circuit can be deduced for this structure. This procedure might yield better agreement between simulations and the observed I-V curves and noise, but such representations are difficult to obtain over the wide frequency range necessary. Another problem with this approach is that it introduces several additional parameters into the nonlinear problem.

The behavior of noise in the current-biased RSJ model without a local oscillator was discussed

extensively in Chapter 3. The output voltage noise of the device is seen to exceed the thermal noise at bias voltages less than the critical voltage, $I_C R_N$. This noise was shown to arise from the presence of the AC Josephson oscillations in the device. At low voltages, where the dynamic resistance is high, these oscillations have a sufficiently large linewidth so that there is excess fluctuation power at very low frequencies due to the tails of their Lorentzian profile. For this simple case, Likharev and Semenov have proposed a simple analytic expression for the noise. RSJ simulations published by Voss had previously shown the presence of this effect, but did not agree well the LS model form. We showed, for the first time, that if the values of the current and dynamic resistance in the LS model were replaced with the values from the simulated I-V characteristic, excellent agreement with the simulations could be obtained. However, the LS model was observed to break down when the RF impedance seen by the junction deviated strongly from a simple resistance. We also showed that this "excess" noise followed the scaling with the RSJ noise parameter, Γ, predicted by Vystavkin *et al.*. Since the magnitude of the excess is determined by the (constant) power of the Josephson oscillations, its relative severity (to the thermal noise) increases as the noise parameter (and thus the thermal noise level) is decreased.

In Chapter 4, we proceeded to the discussion of mixing in the RSJ model. We presented calculations of mixer noise and conversion matrices obtained with a method similar to that of Taur, but extended to the case of non-zero device capacitance. From these matrices, the mixer noise temperature and conversion efficiency were obtained as a function of the embedding impedances presented to the mixer. The conversion efficiency and the noise were shown to degrade rapidly for LO frequencies greater than the device critical frequency, ω_C. For frequencies of about half the critical frequency, however, the possibility of nonclassical conversion gain and interesting levels of sensitivity were predicted. This was despite the presence of the excess noise, which was evidenced in the elevated values for the noise correlation matrix elements.

The excess noise was examined further in Chapter 5. Although this noise had been seen in previous simulations, the mechanism for its generation was ascribed to various causes in the literature. We showed that the AC Josephson oscillations were broadened, because of the high

dynamic resistance in the region between Shapiro steps where a mixer is biased. Under a wide range of conditions, in fact, the oscillations are completely incoherent, and appear as a broadband noise, which can be greatly in excess of the thermal noise. This explanation of the excess noise clears away several longstanding misconceptions. Unfortunately, it does imply that the noise is intrinsic and unavoidable in Josephson mixers. Some predictions for the optimization of mixers, in the presence of this noise, can be made based on the understanding of its generation. Most importantly, this noise is not expected to increase with frequency, provided that the RSJ parameters can be kept fixed. Thus an increase in the available $I_C R_N$ product should allow an proportional increase in operating frequency, with no degradation of performance. At very high frequencies, of course, the quantum noise should add in quadrature to this excess. Nonetheless, this means that the excess noise could become relatively less important as frequency increases.

Armed with the results of the mixer calculations, we were able to determine the device requirements for an optimal Josephson mixer. Chapter 6 described the fabrication procedure developed to obtain stable and well-characterized Josephson-effect devices based on resistively-shunted tunnel junctions. Submicron lithography of high-current density junction was needed to realize nonhysteretic devices with sufficiently high normal-state impedances. These devices also required careful design for the shunting resistors, in order to reduce any parasitic reactances. While these devices overcame the main drawbacks of point contacts, the shunting which was required to reduce the hysteresis also resulted in reduced $I_C R_N$ products. Consequently, while these shunted junctions were nearly optimal for operation at 100 GHz, they were not very suitable for higher-frequency work.

These shunted junctions were tested in a waveguide heterodyne receiver at 100 GHz, as described in Chapter 8, in order to compare them with the expectations of the RSJ modeling. This system attained some of the best overall sensitivities reported to date, but some nonideal behavior, including saturation, was observed. Most importantly, however, the system noise remained a factor of about four higher than that predicted from the RSJ model, even with the excess noise. The devices were observed to interact strongly with the external circuit. The experiments described in

Chapter 7 were then performed in order to verify that elevated output noise was the source of the reduced receiver sensitivity. Well-calibrated measurements of the absolute noise power available from the junction were made at the intermediate frequency of 1.5 GHz. This required construction of a test system in which the coupling of the junction to the measurement system could be accurately made. While the noise agreed well with either the LS or RSJ models for devices with small $I_C R_N$ products, significantly higher noise was seen for higher $I_C R_N$ products. This noise also showed structure as a function of bias voltage, due to the interaction with resonances in the high-frequency coupling structures. The noise of weakly-coupled junctions under LO illumination was also measured. In this case, the output noise was elevated by the same factor of about four which had been inferred from the heterodyne measurements. Techniques for matching the junction to free-space without introducing resonances, such as wide-band planar antennas, might be able to eliminate this sensitivity of the noise to the RF impedance variations. Alternatively, an accurate model of the impedance could be included in the RSJ simulations, and the performance optimized including the interaction with the external circuit.

The goal of this thesis research was to evaluate the potential of Josephson mixers as a possible replacement for SIS mixers for very high-frequency submillimeter detection. It rapidly became evident that a greater understanding of the physics of these devices was required in order to address this question, and that is what we have attempted to present in the preceding chapters. The two main deficiencies of Josephson mixers prior to the beginning of this work were the mysterious excess noise, and their reliance on the undesirable point contact devices. While progress was made on both of these issues, other questions have been raised as a result of our work. Unfortunately, it appears that the strong nonlinearity of the Josephson effect, while it does permit good frequency conversion, leads to many difficulties, including the excess noise and an apparent dependence of the device dynamics upon the external circuitry to which it is connected. The true answer regarding the utility of Josephson-effect mixers for sensitive detection may be largely determined by the future progress in fabrication of devices based on high-T_C materials. If high-quality, large $I_C R_N$ product devices with suitable impedances become available on substrates with acceptable RF properties,

then experiments in the frequency range currently inaccessible to SIS mixers (*i.e.*, above a terahertz) would be justified.

Epilogue

Sarcastic Science, she would like to know,
In her complacent ministry of fear,
How we propose to get away from here
When she has made things so we have to go
Or be wiped out. Will she be asked to show
Us how by rocket we may hope to steer
To some star off there, say, a half light-year
Through temperature of absolute zero?
Why wait for Science to supply the how
When any amateur can tell it now?
The way to go away should be the same
As fifty million years ago we came –
If anyone remembers how that was.
I have a theory, but it hardly does.

– Robert Frost, *Why Wait For Science*

References

Abramowitz, M., and I.A. Stegun, 1964, *Handbook of Mathematical Functions* (New York: Dover).

Ambegaokar, V., and A. Baratoff, 1963, *Phys. Rev. Lett.*, **10**, 486.

Ambegaokar, V., and B.I. Halperin, 1969, *Phys. Rev. Lett.*, **22**, 1364.

Anderson, P.W., and J.M. Rowell, 1963, *Phys. Rev. Lett.*, **10**, 230.

Aslamazov, L.G., A.I. Larkin, and Yu.N. Ovchinnikov, 1968, *Sov. Phys.-JETP*, **55**, 323.

Bardeen, J., L.N. Cooper, and J.R. Schrieffer, 1957, *Phys. Rev.*, **108**, 1175.

Barone, A., and G. Paterno, 1982, *Physics and Applications of the Josephson Effect* (New York: John Wiley and Sons).

Blaney, T.G., N.R. Cross, and R.G. Jones, 1982, *J. Phys. D: Appl. Phys*, **15**, 2103.

Büttgenbach, T.H., R.E. Miller, M.J. Wengler, D.M. Watson, and T.G. Phillips, 1988, *IEEE Trans. on Microwave Theory and Techniques*, **MTT-36**, 1720.

Büttgenbach, T.H., T.D. Groesbeck, and B.N. Ellison, 1990, *Int. J. of IR and MM Waves*, **11**, 1.

Büttgenbach, T.H., H.G. LeDuc, P.D. Maker, and T.G. Phillips, 1992, *IEEE Trans. on Applied Superconductivity*, **2**, 165.

Callen, H.B., and T.A. Welton, 1951, *Phys. Rev.*, **83**, 34.

Caves, C.M., 1982, *Phys. Rev. D*, **26**, 1817.

Cicogna, G., 1987, *Phys. Lett. A*, **121**, 403.

Cicogna, G., 1988, *Phys. Lett. A*, **131**, 98.

Claassen, J.H., and P.L. Richards, 1978a, *J. Appl. Phys.*, **49**, 4117.

Claassen, J.H., and P.L. Richards, 1978b, *J. Appl. Phys.*, **49**, 4130.

Cohen, M.H., L.M. Falicov, and J.C. Phillips, 1962, *Phys. Rev. Lett.*, **8**, 316.

Cooper, L.N., 1956, *Phys. Rev.*, **104**, 1189.

Daalmans, G.M., Th. de Grauw, S. Lidholm, and Fr. v. Vliet, 1980, *SQUID '80*, p. 863.

Dayem, A.H., and R.J. Martin, 1962, *Phys. Rev. Lett.*, **8**, 246.

Devyatov, I.A., L.S. Kuzmin, K.K. Likharev, V.V Migulin, and A.B. Zorin, 1986, *J. Appl. Phys*, **60**, 1808.

Dolan, G.J., R.A. Linke, T.C.L.G. Sollner, D.P. Woody, and T.G. Phillips, 1981, *IEEE Trans. on Microwave Theory and Techniques*, **MTT-29**, 87.

Edrich, J., 1976, *IEEE Trans. on Microwave Theory and Techniques*, **MTT-24**, 706.

Edrich, J., D.B. Sullivan, and D.G. McDonald, 1977, *IEEE Trans. on Microwave Theory and Techniques*, **MTT-25**, 476.

Feynman, R.P., R.B. Leighton, and M. Sands, 1964, *The Feynman Lectures on Physics* (Reading, MA: Addison-Wesley).

Grimes, C.C., and S. Shapiro, 1968, *Phys. Rev.*, **169**, 397.

Groesbeck, T., 1994, *Doctoral Dissertation*, Califonia Institute of Technology.

Gundlach, K.H., and J. Kadlec, 1978, *Solid State Communications*, **25**, 1149.

Gurvitch, M., M.A. Washington, H.A. Huggins, and J.M. Rowell, 1983, *IEEE Trans. on Magnetics*, **MAG-19**, 791.

Grossman, E.N., and L.R. Vale, 1994, in preparation.

Hamilton, C.A., R.L. Kautz, M. Steig, K. Chieh, W.F. Avrin, and M.B. Simmonds, 1991, *IEEE Trans. on Instrumentation and Measurement*, **40**, 301.

Hartfuß, H.J., K.H. Gundlach, and V.V. Schmidt, 1981, *J. Appl. Phys.*, **52**, 5411.

Honingh, C.E., M.M.T.M. Dierichs, H.H.A. Schaeffer, T.M. Klapwijk, and Th. de Graauw, 1991, *2nd Int. Symposium on Space Terahertz Technology*, p. 473.

ter Horst, G., Th. de Grauw, R.A. Panhuyzen, H. Schaeffer, Th.J. Helmerhorst, T. Klapwijk, and J. Kortland, 1985, *SPIE Instrumentation for Submillimeter Spectroscopy*, **598**, 39.

Hunt, B.D., M.C. Foote, W.T. Pike, J.B. Barner, and R.P. Vasquez, 1994, *Physica C*, **230**, 141.

Johnson, J.B., 1928, *Phys. Rev.*, **32**, 106.

Johnson, W.J., 1968, *Doctoral Dissertation*, University of Wisconsin, Madison.

Josephson, B.D., 1962, *Physics Letters*, **1**, 251.

Josephson, B.D., 1963, *Doctoral Dissertation*, Cambridge University.

Kautz, R.L., 1981, *J. Appl. Phys.*, **52**, 3528.

Kerr, A.R., and S.K. Pan, 1990, *Int. J. of IR and MM Waves*, **11**, 1169.

Kautz, R.L., and R. Monaco, 1984, *J. Appl. Phys.*, **57**, 875.

Koch, R.H., D.J. Van Harlingen, and J. Clarke, 1980, *Phys. Rev. Lett.*, **45**, 2132.

Koch, R.H., D.J. Van Harlingen, and J. Clarke, 1981, *Phys. Rev. Lett.*, **47**, 1216.

Koch, R.H., D.J. Van Harlingen, and J. Clarke, 1982, *Phys. Rev. B*, **26**, 74.

Koch, R.H., 1982, *Doctoral Dissertation*, University of California, Berkeley.

Kooi, J.W., M. Chan, T.G. Phillips, B. Bumble, and H.G. LeDuc, 1992, *IEEE Trans. on Microwave Theory and Techniques*, **MTT-40**, 812.

Kooi, J.W., M. Chan, B. Bumble, H.G. LeDuc, and T.G. Phillips, 1994, *Int. J. of IR and MM Waves*, **15**, 783.

Kittel, C., 1976, *Solid State Physics* (New York: J. Wiley and Sons).

Kraus, J.D., 1966, *Radio Astronomy* (New York: McGraw-Hill).

de Lange, G., 1994, *Doctoral Dissertation*, University of Groningen, Gronigen, the Netherlands.

LeDuc, H.G., B. Bumble, S.R. Cypher, A.J. Judas, and J.A. Stern, 1992, *3rd Int. Symposium on Space Terahertz Technology*, p. 408.

Likharev, K.K., and L.S. Kuzmin, 1977, *Radiotekh. Elektron. (Radio Eng. Electron. Phys. (USSR))*, **22**, 1689.

Likharev, K.K., and V.K. Semenov, 1972, *JETP Lett.*, **15**, 625.

Likharev, K.K., 1986, *Dynamics of Josephson Junctions and Circuits* (New York: Gordon and Breach).

Little, L.T., S.R. Davies, and C.T. Cunningham, 1992, *Int. J. of IR and MM Waves*, **12**, 659.

Lukens, J., 1990, in *Superconducting Devices*, S.T. Ruggiero and D.A. Rudman (Boston: Academic Press), p. 135.

McCumber, D.E., 1968, *J. Appl. Phys*, **39**, 2503.

McGrath, W.R., P.L. Richards, A.D. Smith, H. van Kempen, R.A. Batchelor, D.E. Prober, and P. Santhanam, 1981, *Appl. Phys. Lett.*, **39**, 655.

McGrath, W.R., A.V. Räisänen, and P.L. Richards, 1986, *Int. J. of IR and MM Waves*, **7**, 543.

McGrath, W.R., J.A. Stern, H.H.S. Javadi, S.R. Cypher, B.D. Hunt, and H.G. LeDuc, 1991, *IEEE Trans. on Magnetics*, **MAG-27**, 2650.

Mears, C.A., Q. Hu, P.L. Richards, A.H. Worsham, D.E. Prober, and A.V. Räisänen, 1991, *Appl. Phys. Lett.*, **57**, 2487.

Nyquist, H., 1928, *Phys. Rev.*, **32**, 110.

Octavio, M., 1984, *Phys. Rev. B*, **29**, 1231.

Padin, S., and G.G. Ortiz, 1991, *IEEE Trans. on Microwave Theory and Techniques*, **39**, 1239.

Panhuyzen, R.A., G. ter Horst, Th. de Grauw, H. Schaeffer, T.M. Klapwijk, J. Kortland, and J.E. Mooij, 1987, *IEEE Trans. on Magnetics*, **MAG-23**, 125.

Pedersen, N.F., 1980, in *SQUID '80*, H.D. Hahlbohm and H. Lübbig (Berlin: W. de Gruyter), p. 739.

Pedersen, N.F., and A. Davidson, 1981, *Appl. Phys. Lett.*, **39**, 830.

Phillips, T.G., and J. Keene, 1992, *Proceedings of the IEEE*, **80**, 1662.

Poorter, T., 1982, *J. Appl. Phys.*, **53**, 51.

Rogovin, D., and D.J. Scalapino, 1974, *Annals of Physics*, **86**, 1.

Rosenthal, P.A., E.N. Grossman, R.H. Ono, and L.R. Vale, 1993, *Appl. Phys. Lett.*, **63**, 1984.

Rosenthal, P.A., and E.N. Grossman, 1994, *IEEE Trans. on Microwave Theory and Techniques*, **42**, 707.

Shapiro, S., 1963, *Phys. Rev. Lett.*, **11**, 80.

Shoji, A., S. Kiryu, and S. Kohijiro, 1992, *Appl. Phys. Lett.*, **60**, 1624.

Stern, J.A., 1991, *Doctoral Dissertation*, California Institute of Technology.

Stern, J.A., H.G. LeDuc, and A.J. Judas, *3rd Int. Symposium on Space Terahertz Technology*, p. 420.

Stewart, W.C., 1968, *Appl. Phys. Lett.*, **12**, 277.

Stratonovich, R.L., 1963, *Topics in the Theory of Random Noise* (New York: Gordon and Breach).

Taur, Y., J.H. Claassen, and P.L. Richards, 1974a, *Appl. Phys. Lett.*, **24**, 101.

Taur, Y., J.H. Claassen, and P.L. Richards, 1974b, *IEEE Trans. on Microwave Theory and Techniques*, **MTT-22**, 1005.

Taur, Y., and A.R. Kerr, 1978, *Appl. Phys. Lett.*, **32**, 775.

Taur, Y., 1980, *IEEE Trans. on Electron Devices*, **ED-27**, 1921.

Tinkham, M., 1975, *Introduction to Superconductivity* (New York: McGraw-Hill).

Torrey, H.C, and C.A. Whitmer, 1948, *Crystal Rectifiers* (New York: McGraw-Hill).

Tucker, J.R., 1979, *IEEE J. of Quantum Elec.*, **QE-15**, 1234.

Tucker, J.R., and M.J. Feldman, 1985, *Rev. of Modern Phys.*, **57**, 1055.

Van Duzer, T., and C.W. Turner, 1981, *Principles of Superconductive Devices and Circuits* (New York: Elsevier).

Voss, R.F., 1981, *J. Low Temp. Phys.*, **42**, 151.

Vystavkin, A.N., V.N. Gubankov, L.S. Kuzmin, K.K. Likharev, V.V. Migulin, and V.K. Semenov, 1974, *Rev. Appl. Phys*, **9**, 79.

Walker, C.K., J.W. Kooi, M. Chan, H.G. LeDuc, P.L. Schaffer, J.E. Carlstrom, and T.G. Phillips, 1992, *Int. J. of IR and MM Waves*, **13**, 785.

Weinreb, S., D.L. Fenstermacher, R.W. Harris, 1982, *IEEE Trans. on Microwave Theory and Techniques*, **MTT-30**, 849.

Wengler, M.J., 1987, *Doctoral Dissertation*, California Institute of Technology.

Werthamer, N.R., 1966, *Phys. Rev.*, **147**, 255.

Woody, D.P., R.E. Miller, and M.J. Wengler, 1985, *IEEE Trans. on Microwave Theory and Techniques*, **MTT-33**, 90.

Zavaleyev, V.P., and K.K. Likharev, 1981, *Radiotekh. Elektron. (Radio Eng. Electron. Phys. (USSR))*, **26**, 1554.

Zavaleyev, V.P., and K.K. Likharev, 1981, *IEEE Trans. on Magnetics*, **MAG-17**, 830.

Zmuidzinas, J., H.G. LeDuc, J.A. Stern, and S.R. Cypher, 1994, *IEEE Trans. on Microwave Theory and Techniques*, **42**, 698.

Appendix A

Lossy Transmission Lines

In this appendix, we will discuss the propagation of waves on lossy transmission lines. The well-known case of small loss is derived first, and then the case of large losses per wavelength is developed. This last case is crucial in the proper analysis of the microstrip resistors used for the fabrication of resistively-shunted junctions and discussed in Chapter 6. We will also discuss the modifications to ordinary microstrip transmission lines when ground plane or top conductor is superconducting.

A1. Transmission Lines: Small Losses

The simple description of transmission lines can be found in many books on electrical engineering. The equivalent circuit for a general transmission line is shown below in Figure A1.1. It consists of a ladder of series impedances R and L, with shunt admittances G and C, where all quantities are per unit length. We can write down the two following equations,

$$\begin{aligned} -\frac{\partial V}{\partial x} &= L\frac{\partial I}{\partial t} + RI \\ -\frac{\partial I}{\partial x} &= GV + C\frac{\partial V}{\partial t}, \end{aligned} \tag{A1.1}$$

where V and I are functions of both x and t. We can then eliminate the current to obtain the

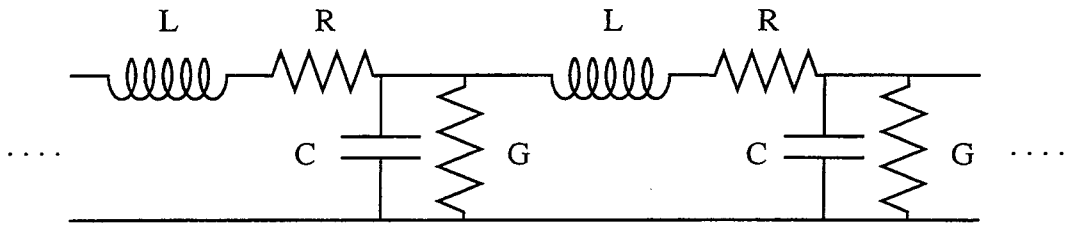

Figure A1.1 Equivalent circuit diagram for ideal transmission line. All quantities are per unit length.

governing equation for the voltage,

$$\frac{\partial^2 V}{\partial x^2} = RGV + (RC + LG)\frac{\partial V}{\partial t} - LC\frac{\partial^2 V}{\partial t^2}. \qquad (A1.2)$$

In the case of vanishing losses, we set both R and G to zero, and (A1.2) reduces to the simple wave equation,

$$\frac{\partial^2 V}{\partial x^2} = -LC\frac{\partial^2 V}{\partial t^2}.$$

We expect travelling wave solutions for the voltage (and the current),

$$V(x,t) = \Re e\left[V_0\, e^{-\jmath(kx-\omega t)}\right], \qquad (A1.3)$$

where V_0 is a constant and k is the wave vector. We see that the dispersion relation is $k^2 = \omega^2 LC$, and the phase velocity, v_p, is given by

$$v_p = \frac{\omega}{k} = \frac{1}{\sqrt{LC}}. \qquad (A1.4)$$

We define the characteristic impedance of the transmission line to be the ratio of voltage to current at any point,

$$Z_C = \frac{V(x,t)}{I(x,t)} = \frac{\jmath\omega L}{\jmath k} = \sqrt{\frac{L}{C}}. \qquad (A1.5)$$

If we now consider the case in which the shunt conductance, G, is zero, but there is a nonvanishing resistance for the line, R, then the dispersion relation becomes

$$k^2 = -\jmath\omega C(R + \jmath\omega L). \qquad (A1.6)$$

This can be linearized for small losses when the inductance dominates over the resistance, *i.e.*, when $Q = \omega L/R \gg 1$, giving

$$k = \beta - \jmath\alpha = \frac{\omega}{v_p} + \frac{\jmath R}{2\sqrt{L/C}}. \qquad (A1.7)$$

The equations for the voltage or current can then be rewritten in the form

$$V(x,t) \;=\; \Re e\left[V_0\, e^{-\alpha x} e^{-\jmath\,\omega(t-x/v_p)}\right]. \qquad (A1.8)$$

This form makes it clear that there is a travelling wave solution, which propagates with the unperturbed (*i.e.*, zero loss) velocity, v_p, but which is now attenuated over a length scale $1/\alpha$, with α given above in Equation (A1.7). The voltage attenuation per wavelength is α, and since both voltage and current decay in the same way, the power attenuation coefficient is 2α. We can also rewrite the characteristic impedance of the line after linearizing,

$$Z_C = \sqrt{\frac{L}{C}}\left(1 - \jmath\frac{1}{2}\frac{R}{\omega L}\right). \qquad (A1.9)$$

We see that the characteristic impedance now has a reactive (imaginary) part which is small and negative, but the real part of the impedance is unchanged. The input impedance is equal to the characteristic impedance if the line is infinitely long, or if there are no reflections at the termination of the line. For a general line terminated in an arbitrary impedance, one needs to consider the effect of reflections at the termination. This will be discussed for the particular case of the resistors below.

A2. Transmission Lines: Large Losses

We can now examine the opposite limiting case to that discussed above, *i.e.*, when the loss is large and $Q = \omega L/R \ll 1$. We will show below that this case is the relevant one for the AuGe resistors used in the junction fabrication. We again ignore the shunt conductance, G, which will be extremely small for the microstripline resistors (the SiO is a good insulator). The dispersion relation, Equation (A1.6), is unchanged, but we will now linearize with respect to the small Q-factor. We

define the propagation constant, γ, to be equal to $-\jmath k$, which gives

$$\gamma = \alpha + \jmath\beta = \sqrt{(R+\jmath\omega L)(\jmath\omega C)}. \qquad (A2.1)$$

Expanding in the small quantity $Q = \omega L/R$, we obtain

$$\gamma = \omega\sqrt{LC}\sqrt{\frac{R}{2\omega L}}\,(1+\jmath). \qquad (A2.2)$$

Notice that the real and imaginary parts of the propagation constant (and of the wavevector) are now equal. The phase velocity is still given by $v_p = \omega / \Re e(k)$, so we have

$$v_p = \frac{1}{\sqrt{LC}}\sqrt{\frac{2\omega L}{R}} = v_{p0}\sqrt{2Q}, \qquad (A2.3)$$

where v_{p0} is the loss-free velocity. So we see that the velocity is reduced from the small-loss velocity. This slowing will of course also reduce the wavelength, and thus require shorter sections of resistor to prevent reactances. We can also calculate the characteristic impedance in the large-loss case, obtaining

$$Z_c = \sqrt{\frac{L}{C}}\sqrt{\frac{R}{2\omega L}}\,(1-\jmath) = Z_0\frac{1}{\sqrt{2Q}}\,(1-\jmath), \qquad (A2.4)$$

where Z_0 is the loss-free characteristic impedance. We see that the characteristic impedance of the line also has equal real and imaginary parts, and the magnitude of the real part of the impedance has also been reduced by a factor of $\sqrt{2Q}$. Having discussed the propagation and characteristic impedances of transmission lines, we now move on to the effective impedance of terminated sections of line with finite length.

A3. Short-circuited Lines of Finite Length

If the impedance of a lossy line of infinite length is measured, one finds the impedance to be equal to the characteristic impedance of the line. For finite lengths of line, however, a mismatch at the termination of the line can lead to reflections and standing waves. This modifies the impedance seen from the opposite end of the line. The well-known formula for the transformation of a load

impedance by a lossless transmission line is

$$Z_{IN} = Z_0 \left[\frac{1 + \Gamma_L e^{-\jmath\, \beta 2d}}{1 - \Gamma_L e^{-\jmath\, \beta 2d}} \right], \tag{A3.1}$$

where d is the length of the line, β and Z_0 are the imaginary part of the propagation constant and the characteristic impedance of the line, and Γ_L is the voltage reflection coefficient at the load impedance, Z_L, which terminates the line. The reflection coefficient is defined as

$$\Gamma_L = \frac{Z_L - Z_0}{Z_L + Z_0}. \tag{A3.2}$$

Obviously, if the line is terminated in a matched load, $Z_L = Z_0$, then there are no reflections, and the input impedance is equal to the characteristic impedance. If the line is terminated in a perfect short-circuit, $Z_L = 0$, then the input impedance becomes

$$Z_{IN} = \jmath\, Z_0 \tan(\beta d) = \jmath\, Z_0 \tan\left(\frac{2\pi d}{\lambda_g}\right), \tag{A3.3}$$

where λ_g is the wavelength on the line (guide wavelength). The dependence of the input impedance on the electrical length of a low-loss line is shown in Figure A3.1. The circuit is highly resonant, with a periodic dependence on the length. For a quarter-wave section of line, the short-circuit termination is transformed into an open circuit. This principle is widely used in microwave design.

If we instead consider a short-circuited section of the lossy line discussed in the previous section, we need to replace the arguments of the exponentials in Equation (A3.1) with $2\gamma d$, where γ is the complex propagation constant, Equation (A2.2). Then we have

$$Z_{IN} = Z_c \tanh(\gamma d) = Z_0 \frac{1}{\sqrt{2Q}} (1 - \jmath) \tanh\left[\frac{1 + \jmath}{\sqrt{2Q}} \frac{2\pi d}{\lambda_{g0}}\right]. \tag{A3.4}$$

Here λ_{g0} is the loss-free guide wavelength. For sufficiently short lines, if $d \ll \lambda_g$, then $\tanh(x) \sim x$, and the impedance becomes

$$Z_{IN} \sim Z_0 \frac{1}{Q} \frac{2\pi d}{\lambda_{g0}} = Rd, \tag{A3.5}$$

i.e., the input impedance is simply the resistance of the strip (recall that R is the resistance per unit length), and purely real. The real and imaginary parts of the impedance for a short-circuited line

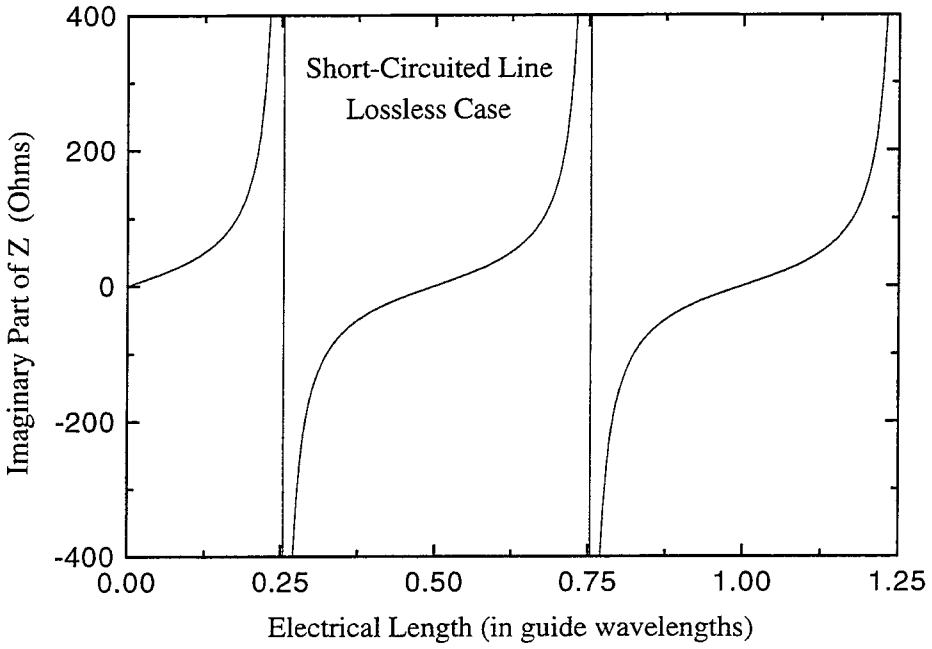

Figure A3.1 A plot of the impedance of a short-circuited lossless transmission line as a function of the electrical length, d/λ_g. The impedance has an infinite number of resonances separated by a half-wavelength. The characteristic impedance of the line was assumed to be 50 Ohms.

with 50 Ohm loss-free characteristic impedance and a Q of 0.1, is plotted in Figure A3.2 versus the length of the line in units of length normalized to the lossy guide wavelength, $\lambda_{LOSSY} = \frac{2\pi}{\omega\sqrt{LC}}\sqrt{2Q}$. We see that the real part of the impedance increases linearly with length, and then undergoes a single resonance when the line is approximately a half-wavelength long. The imaginary part is capacitive (negative), and nearly zero for lines less than about 0.1 waves, and then rapidly increases. For long lines (greater than about 3/4 of a wavelength) the impedance approaches the characteristic impedance of the line. For these very lossy lines, the attenuation per wavelength is high, so that no reflected waves return to the input for lengths comparable to a wavelength.

A4. Shunt Resistors as Lossy Transmission Lines

Having developed the formalism for the analysis large-loss transmission lines, we can now proceed to a specific analysis of the microstrip line which represents the AuGe resistors used in the resistively-shunted tunnel junction fabrication described in Chapter 6. First we will briefly discuss

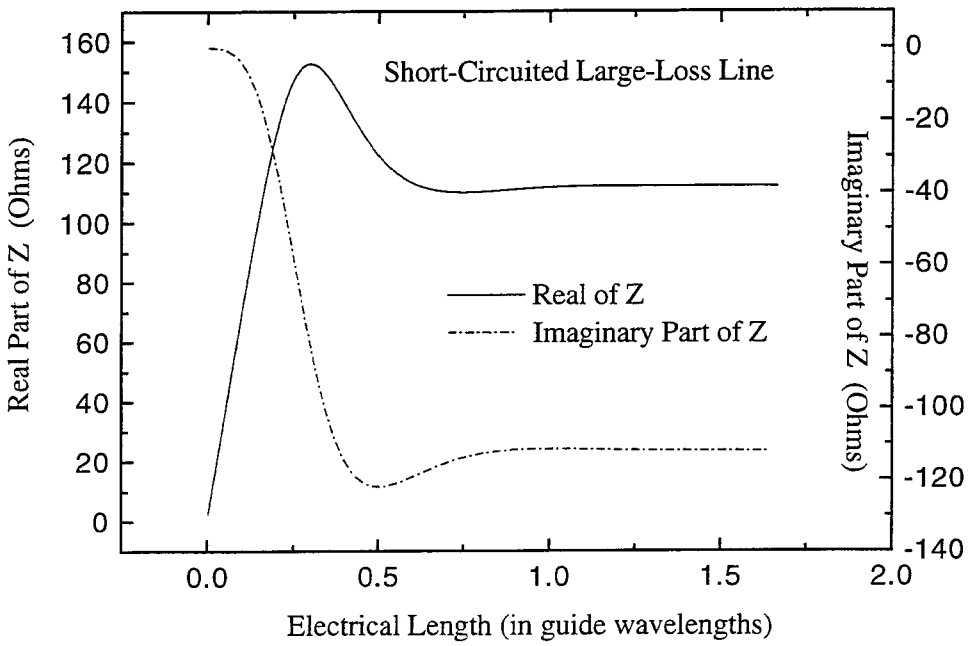

Figure A3.2 The real (full line) and imaginary (dash-dot line) parts of the impedance of a short-circuited section of very lossy transmission line as a function of the electrical length. The line was assumed to have a lossless characteristic impedance, Z_0, of 50 Ohms and a Q of 0.1. The guide wavelength is that of the lossy line, *i.e.*, the lossless guide wavelength divided by $\sqrt{2Q}$.

microstripline and the dependence of the electrical parameters on the line geometry, and then we will show the modifications which must be made when one or both of the metallization layers is superconducting.

A schematic of a general microstrip transmission line is shown in Figure A4.1. It consists of a metallic ground plane, an insulating layer of height h, and a metallic strip of width w and thickness t on top of the insulator. This structure has a TEM mode, which can easily be analyzed in the limit $w \gg h$, where the fringing of the fields at the edges of the stripline is small. The inductance and capacitance per unit length for this line are

$$L = \mu_0 \kappa \frac{h}{w} \qquad \text{and} \qquad C = \epsilon_0 \epsilon_r f \frac{w}{h}, \tag{A4.1}$$

where κ and f are numerical factors of order one to account for fringing, μ_0 and ϵ_0 are the vacuum permeability and permittivity, respectively, and ϵ_r is the relative dielectric constant of

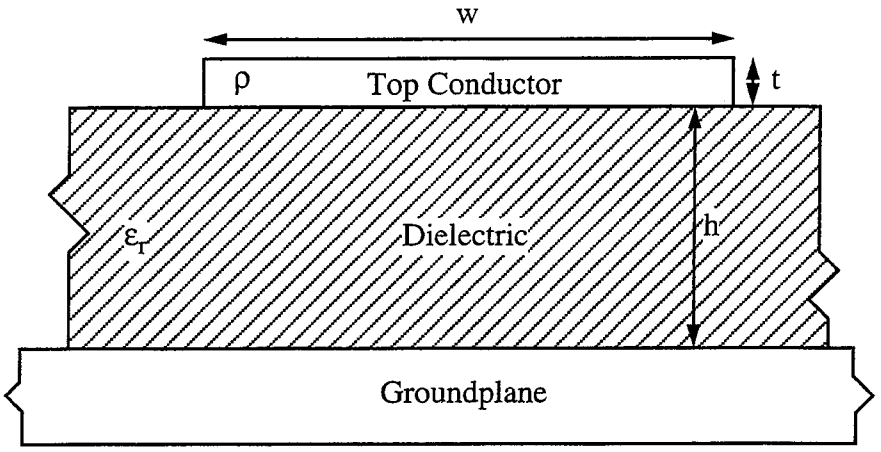

Figure A4.1 Schematic of a general microstrip transmission line.

the insulating dielectric. Ignoring the fringing fields, the characteristic impedance of the line is $Z_C = \sqrt{\frac{L}{C}} = \frac{h}{w}\sqrt{\frac{\mu_0}{\epsilon_0\epsilon_r}}$, which can also be expressed as $\frac{h}{w} \times 377\ \Omega/\sqrt{\epsilon_r}$. The phase velocity on the line is independent of the geometry, and depends only on the dielectric constant of the insulator, $v_p = 1/\sqrt{LC} = 1/\sqrt{\epsilon_0\mu_0\epsilon_r} = c/\sqrt{\epsilon_r}$. In the case in which both metals are superconducting, there is a modification to the inductance per unit length due to the penetration of the magnetic field into the superconductor. The general expression for the inductance per unit length then becomes (Van Duzer and Turner, 1981)

$$L_{SUP} = \frac{\mu_0}{w}\left[h + \lambda_1 \coth\frac{\lambda_1}{t_1} + \lambda_2 \coth\frac{\lambda_2}{t_2}\right], \qquad (A4.2)$$

where λ_1, λ_2 and t_1, t_2 are the penetration depths and thicknesses of the two superconducting films. In the case of thick (*i.e.*, $t \gg \lambda$) films, the effect is simply to replace the height of the dielectric, h, with $h + \lambda_1 + \lambda_2$ in the expressions for L. There are also corrections for the surface impedance and loss of the superconductor, which are small and will be ignored here.

We can now examine the case in which the top electrode is lossy, and the ground plane is a thick superconductor. The loss of the superconductor will be negligible compared to that of the resistor material, and is ignored. For a top conductor with resistivity ρ, the resistance per unit

TABLE A.1
SHUNT RESISTOR FABRICATION PARAMETERS

Width	w	2 μm
Dielectric Thickness	h	1200 Å
Dielectric Constant	ϵ_r	5.8
Nb Penetration Depth	λ	800 Å
AuGe Resistivity	ρ	$10\,\mu\Omega - cm$
Resistor Thickness	t	100 Å
Sheet Resistance	$R_\square$	10 Ω/□
Resistor Length	ℓ	10 μm
Resistance	R	50 Ω

length of the line becomes $R = \rho/tw = R_\square/w$, where $R_\square$ is the sheet resistance of the film. The expression for the impedance of a shorted section of low-Q line, Equation (A3.4), written out to explicitly contain L, R, and C, is

$$Z_{IN} = \sqrt{\frac{L}{C}}\sqrt{\frac{R}{2\omega L}}(1-\jmath)\ \tanh\left[\omega\sqrt{LC}\sqrt{\frac{R}{2\omega L}}(1+\jmath)d\right]$$
$$Z_{IN} = \sqrt{\frac{\omega R}{2C}}(1-\jmath)\ \tanh\left[\sqrt{\frac{\omega RC}{2}}(1+\jmath)d\right]. \qquad (A4.3)$$

Note that provided that the Q of the line is small enough, there is no explicit dependence on the inductance per unit length. In terms of the resistor geometry, this becomes

$$Z = \sqrt{\frac{R_\square h}{2\epsilon_0\epsilon_r w^2}}\frac{1}{\sqrt{\omega}}(1-\jmath)\ \tanh\left[\sqrt{\frac{R_\square\epsilon_0\epsilon_r}{2h}}\sqrt{\omega}(1+\jmath)\,d\right]. \qquad (A4.4)$$

The typical values for the shunt resistor geometry are given in Table A4.1. Equation (A4.4) is applied to the specific case of the shunt resistors and the impedance as a function of length and as a function of frequency are displayed in Section 6.4.

Reference for Appendix A

T. Van Duzer and C.W. Turner, 1981, *Principles of Superconductive Devices and Circuits* (New York: Elsevier).